國立臺灣大學理學院物理學研究所

碩士論文

Department of Physics
College of Science
National Taiwan University

Master's Thesis

矽奈米粒子於深紫外區間所展現的非線性極化子散射和超解析顯微術的應用

Deep Ultraviolet Nonlinear Polaritonic Scattering of Silicon Nanostructure and Application to Super-resolution Optical Microscopy

林子婷

Zi-Ting Lin

指導教授：朱士維 博士

Advisor: Shi-Wei Chu, PhD

中華民國 114 年 5 月

May, 2025

doi:10.6342/NTU202501130

國立臺灣大學碩士學位論文
口試委員會審定書

MASTER'S THESIS ACCEPTANCE CERTIFICATE
NATIONAL TAIWAN UNIVERSITY

矽奈米粒子於深紫外區間所展現的非線性極化子散射和超解析顯微術的應用

Deep Ultraviolet Nonlinear Polaritonic Scattering of Silicon Nanostructure and Application to Super-resolution Optical Microscopy

本論文係林子婷 同學(R11222033)在國立臺灣大學 理學院物理學研究所碩士班 完成之碩士學位論文，於民國 114 年 05 月 14 日承下列考試委員審查通過及口試及格，特此證明。

The undersigned, appointed by the Department / Institute of Department of Physics, National Taiwan University on 14/05/2025 have examined a Master's thesis entitled above presented by Zi-Ting Lin (R11222033) candidate and hereby certify that it is worthy of acceptance.

口試委員 Oral examination committee:

朱士維　　曾銘綸　　[illegible]

（指導教授 Advisor）

doi:10.6342/NTU202501130

致謝

我於 2022 年 7 月加入了朱士維教授的實驗室、2022 年 11 月加入了高原淳一教授的實驗室、2023 年 4 月加入了曾銘綸助理教授實驗室，使我對於各式研究有了諸多的體悟，原先對於光學以及半導體研究一竅不通的我，逐漸累積於理論模擬到實驗的經驗，感謝一路上受到的呵護以及各式的幫助，充實我碩士 3 年的研究生涯。

首先，我要感謝我的指導教授朱士維教授，願意提供我許多的資源，協助我建構對於光學以及固態相關理論的理解，於 2022 年的 11 月，使我有幸拜訪大阪大學高原淳一教授實驗室，我很感謝此次的拜訪致使我碩士題目的誕生，期間我和台大實驗室、高原教授以及博後西田健太郎有了諸多學術上的討論，感謝各種關照使我的研究能力有諸多的進步；再來我也要感謝交大電子所，曾銘綸教授於理論模擬以及製程技術上的共同指導，拜訪交大期間我也參加了幾場難得的演講，拓展了我對於半導體光學相關研究不同面向的理解，我喜歡開會時和教授們詢問大面積 DUV 矽光子的製程以及理論細節。此外，朱教授會提醒我要時時記得感謝所有的幫助，使我漸漸改善人格的瑕疵，我銘記在心，也感謝朱教授生活上的協助使我能夠更穩定的學習；而曾教授講求的誠實信任原則，我也謹記在心。

除了教授的各種指導，我也很感謝從實驗室獲得的各種專業協助，首先是博後還有德心學長在我剛進實驗室的時候，輔導我快速步入研究的軌道，以及時常和博後討論，致使我改善了邏輯、報告架構、理論上的瑕疵，我很崇拜年滿 31 歲的兄貴；感謝和德心學長以及 Morpal 學長理論上的討論:傳授和朱教授的溝通秘訣、口述實驗室流傳的歷史迷因、教我陪我幫我量光譜，聽我用英文抱怨在做實驗之餘只能和紐西蘭來的基督徒研究耶穌；也感謝兩位學長傳授如何精緻的描述 photo-thermo-optical effect；感謝俞安學姊和我分享研究上不變的堅持還有 COMSOL 細緻的建模技巧；感謝育傑學長精緻的物理詮釋以及老練的模擬技術，嘆為觀止；還有冷靜的 Jeremy 學長，會和我解釋量子力學艱澀的數學理論；認真嚴格的荐軒學

doi:10.6342/NTU202501130

長會跟大家一起討伐噁男，朱老師還會打電話問子婷有沒有安全，博後還會陪我走到有燈的地方，送我安全回家。雖然我一有機會就用小零食賄賂朱老師、肯塔羅、還有厲害的學長們，但是謝謝你們還是對我很寬容又嚴格。也感謝朱老師和曾老師願意幫我推薦給交大電子所，讓我在 2024 年 11 月正取交大電子所甲組碩班。也謝謝毓隆學長的康愾解囊大神模擬檔案，用程式碼操控 COMSOL 超厲害的，子婷甘拜下風，在朱老師實驗室裡我變成了漂亮有自信的肥宅，我覺得很感謝。此外，也謝謝于碩學長經過地下室找博後聊天的時候神來一筆提起精緻的固態物理；呂宥蓉教授實驗室的景崴學長極簡的描述電漿子物理也令我眼睛為之一亮。

再來，我在交大研究期間習得了固態物理以及極化子相關理論、Lumerical 的細節操作、製程整合、架光路的基本知識，感謝曾老師無微不至的愛護讓我在交大的實驗室有動力從早勞動到晚，也感謝曾老師很常自掏腰包請客，讓我有更多體力做實驗；再來感謝交大的夥伴，感謝宇嘉、宥潔、昱傑、貿豐跟我一起完成製程參數測試，特感謝宇嘉手把手的帶我模擬優化、製程整合；再來是感謝柏叡學長細心的講解調整模擬參數的細節，以及深紫外區間矽材料的理論知識，謝謝學長；還有最強韌的佳樺學妹，包管了實驗室研究相關的大小事辛苦了，研究加油；還有沛縈、冠衡、俊亦、澤凱陪伴我量測，總是可以學到厲害的快捷法；還有貿豐的神祕小徑，俊亦、明峻、育泓和宥潔會借我奈中 24 小時的卡讓我可以晚上處理樣品問題、冠衡也會協助我快速解決光路問題。感謝我在交大吃好睡好，穩定做實驗。

最後，感謝我的家人雖然飽受風霜仍一路上支持我的學習，感謝阿嬤提供溫暖的避風港，感謝爸爸媽媽姊姊穩定的生活。「愛就是在別人身上看見自己的責任」，子婷的哥哥姐姐老師們是那樣教育我的，我也要和東瀚、尹慈、致嘉、庭禎、承軒、品壬、和家、品淳、奕蓁、尚霖、唯峻學弟、北村學妹、鎔仰學長、定薇學姊、笹井學長、森田學長、宮野、宮田、新開學弟、沛縈、宇嘉、宥潔、昱傑、佳樺學妹、貿豐、冠衡、明峻、星貽道謝，感謝你們帶給我真實，需要幫助的話要跟我說白話文具體的求救，我會有耐心的回覆你們，祝研究順利。

doi:10.6342/NTU202501130

摘要

矽是被廣泛研究的材料，並由於其容易取得的特性以及和互補金屬氧化物半導體（CMOS）的相容性而被廣泛應用於半導體產業。半導體產業正致力於縮小芯片尺寸以形成具有更多功能的積體電路。隨著製造技術的提升以及生產的加速，我們需要新的顯微技術來更快地檢查半導體結構。一般業界所使用的掃描式電子顯微鏡（SEM）具有低吞吐量、僅能掃描樣品表面，所使用的高能電子束能量也容易傷害樣品表面，和傳統光學顯微鏡（OM）所具有的高吞吐量、三維樣品的觀測範圍，並和使用低能量的光照檢測相比，OM 不但能避免對樣品造成更多損害同時也提供相較 SEM 大的觀測吞吐量。因此，隨著半導體尺寸日漸縮小至光學的繞射極限無法分辨時，電子顯微鏡反倒得以達成遠小於繞射極限的奈米解析度，因此我們需要超解析光學顯微技術，用以觀測奈米尺度的半導體晶片。

在 2020 年，我們通過結合飽和激發顯微鏡（SAX）和矽奈米結構的光學非線性，達成了 132 奈米的空間解析度。米氏共振有效加熱了矽奈米方塊，使之展現了比矽塊材大了五個數量級的等效光熱非線性指數 n_2，並在可見光區域達成了兩倍的解析度提升。在這篇研究裡面我們預期使用更短的波長來進一步突破繞射極限，以提高 SAX 的光學解析度。最近的研究揭示，在深紫外（DUV）波段光照射下，矽展現了表面極化子共振。在這項研究中，我們模擬了 266 奈米的紫外光激發下，矽奈米粒子基於表面極化子共振，所展現的光熱非線性效應。我們也最佳化矽奈米圓盤結構的半徑，達成 6%的散射強度差異。我們預期這種非線性散射可以應用於 SAX 顯微鏡並提升至 70 奈米的解析度。

此外，我們製作了隨機排列的矽奈米圓盤樣品，並架設了一個配備了光偵測器的光學截斷器系統，以初步檢測非線性現象是否存在。經深紫外光譜儀檢測的矽樣品顯示在約 270 奈米處有共振峰。在實驗中，我們優化了系統的穩定性，以確保良好的可逆性。然而，重複性仍然存在爭議，因此未能於實驗上應證非線性的存在。而均一化的實驗數據顯示其趨勢更接近線性。因此，下一步仍需改善實驗系統，以驗證模擬的結果。

關鍵字：矽奈米光子學、深紫外光學、非線性光學、光熱效應。

doi:10.6342/NTU202501130

Abstract

Silicon material has been widely studied due to its natural abundance and compatibility with complementary metal-oxide semiconductors (CMOS). The semiconductor industry strives to miniaturize chips and develop circuits with enhanced functionality. With the advancement of fabricating techniques and accelerating production, scanning electron microscopy (SEM)'s low throughput, surface-only scanning, and potential sample damage make it insufficient for high-demand semiconductor inspection, necessitating a faster alternative. In contrast, optical microscopes (OM) provide high throughput, a three-dimensional (3D) inspection range, and low-energy illumination, which avoids sample damage. However, OM is limited by the diffraction limit, thus, the resolution is typically 200 nm or worse. Therefore, the development of super-resolution optical microscopy that breaks through resolution limits is highly desired.

In 2020, by combining saturated excitation (SAX) microscopy and optical nonlinearity of a silicon nanostructure, our group achieved 132 nm lateral resolution. Silicon nanoblock with Mie resonance enhanced heating offers an equivalent photothermal nonlinear index n_2 that is five orders larger than bulk silicon, and the nonlinearity provides more than two-fold resolution enhancement. To further enhance optical resolution by SAX, a shorter wavelength is explored in this work. Although silicon has a large imaginary refractive index below 300 nm that reduces the quality factor of

doi:10.6342/NTU202501130

resonance, recent studies have shown that silicon exhibits polaritonic resonance under deep ultraviolet (DUV) excitation. Here, we simulated the enhancement of photo-thermo-optical nonlinearity of a single silicon nanostructure excited at 266 nm wavelength based on polaritonic resonance. An optimized radius of a silicon nanodisk shows a backward scattering intensity difference as large as 17%. We expect this nonlinear scattering can be used in SAX microscopy and yield a 70 nm spatial resolution in the future.

Additionally, we fabricated silicon nanodisks with diameters ranging from 65 nm to 75 nm and built a 266 nm laser light path equipped with a chopper to control exposure time and a photodetector to detect whether nonlinearity exists. The silicon sample inspected by a DUV spectroscope demonstrated a resonant peak at around 270 nm. Even though the system's stability was optimized to ensure good reversibility, reproducibility remains controversial. As a result, the experimental data failed to confirm whether nonlinearity was present. The normalized experimental data indicate a trend that is closer to linearity. The experiment needs further refinement to examine the simulation results.

Keywords: silicon nanophotonics, DUV optics, nonlinear optics, photothermal effect

doi:10.6342/NTU202501130

Contents

口試委員會審定書 i
致謝 ii
摘要 iv
Abstract v
Contents vii
Figure List ix
Table List xi
Chapter 1. Introduction 1
1.1 Semiconductor observation: an introduction to imaging techniques 1
1.2 Super-resolution imaging based on silicon nonlinear scattering 2
1.3 SAX imaging in the DUV region based on silicon polaritonic resonance enhanced photo-thermo-optical nonlinearity 5
Chapter 2. Theory 8
2.1 Mie resonance: introduction to Mie theory 8
2.2 Types of surface polaritons (SPs) at the semiconductor-insulator surface 18
2.3 Photothermal nanophotonic nonlinear scattering 29
2.4 Differential-excitation saturated excitation (dSAX) microscopy 41
2.5 Finite-difference time-domain and finite element method 44
Chapter 3. Materials and Methods 52
3.1 Simulation strategy 52
3.1.1 Particle Swarm Optimization (PSO) method for size determination 53
3.1.2 Simulation Setup in Lumerical and COMSOL 57
3.1.3 Matching simulation results and analytical solutions 62
3.2 Experimental preparation 67
3.2.1 Layout of shuffled silicon nanoarrays 68
3.2.2 Fabrication process of shuffled silicon nanoarrays 70
3.2.3 Setup for spectrum measurement 73
3.2.4 The 266 nm setup for measuring photothermal nonlinear scattering 75
Chapter 4 Simulation results 78
4.1 Polaritonic resonance of a single silicon nanodisk on a quartz substrate in the DUV region 78
4.2 Optimization of the radius of a single silicon nanodisk in Lumerical 81
4.3 Photo-thermo-optical nonlinearity of a silicon nanodisk on quartz excited at 266nm 84
4.4. dSAX microscopy for resolution enhancement[69] 88
Chapter 5. Experimental results 91
5.1 Spectrum measurement in the DUV region 91

doi:10.6342/NTU202501130

5.2 Photothermal nonlinearity experimental measurement 98
Chapter 6. Conclusion and future work 104
6.1 Conclusion 104
6.2 Future work 105
Reference 107

doi:10.6342/NTU202501130

Figure List

Figure 1.1: Super-resolution imaging of p-SAX microscopy. 4
Figure 1.2: Concepts of external heating and self-induced optical heating. 5
Figure 1.3: The refractive index and permittivity of bulk silicon material measured at a temperature of 300K.. 7
Figure 2.1: Schematic diagram of Mie resonance in a dielectric sphere 8
Figure 2.2: A comparison of c-Si and a-Si with their real (n) and imaginary parts (extinction coefficient, k) of the refractive index. 28
Figure 2.3: Photo-thermo-optical nonlinearity analyzed analytically and numerically.. 32
Figure 2.4: Refractive index and permittivity at 266 nm and 561 nm wavelengths as a function of temperatures ranging from 300K to 1400K 36
Figure 2.5: Electric field profiles along the xz-plane are shown in the DUV region 40
Figure 2.6: The excitation intensities (I_{ex}) required to heat a nanoparticle to an average temperature (T) of 700 K. 40
Figure 2.7: The concept of SAX microscopy 42
Figure 2.8: Concept of differential-excitation SAX (dSAX) 44
Figure 2.9: Flowchart of FDTD calculation in space and time. 48
Figure 2.10: The electromagnetic field distribution in a Yee grid mesh. 49
Figure 2.11: FDTD with field equivalence principle to separate incident field and scattered field. 51
Figure 3.1: Particle swarm optimization (PSO) strategy. 54
Figure 3.2: Settings in a particle swarm optimization (PSO). 55
Figure 3.3: Trends of PSO. 56
Figure 3.4: Generation of PSO in the form of color maps. 57
Figure 3.5: The Lumerical environment for calculating modulation depth based on PSO is shown. 59
Figure 3.6: Simulation environment for a single silicon nanodisk. 60
Figure 3.7: COMSOL simulation environment for heating a single silicon nanoparticle. 61
Figure 3.8: Mie analytical solution. 62
Figure 3.9: Scattering cross-section and absorption cross-section fit well between the Mie analytical solution and FDTD simulation in the visible at 561 nm and the DUV region at 266 nm wavelength. 63
Figure 3.10: Simulation of photothermal nonlinear scattering for single silicon nanodisks with widths of 100, 170, and 190 nm. 65
Figure 3.11: Simulation of a silicon nanodisk lying on sapphire. 66
Figure 3.12: Electric fields of a silicon nanodisk lying on the sapphire substrate. 67

doi:10.6342/NTU202501130

Figure 3.13: The layout of shuffled nanodisk arrays of a radius of 36 nm according to the PSO result. 69
Figure 3.14: The 4×5 numbers of arrays are arranged to be patterned by EBL. 69
Figure 3.15: Fabrication of shuffled silicon nanodisk arrays. 71
Figure 3.16: The white light path for measuring spectra. 74
Figure 3.17: The 266 nm laser light path for measuring the nonlinear scattering. 76
Figure 4.1: Simulation of a single silicon nanodisk lying on a quartz substrate. 80
Figure 4.2: Electric field distributions of a silicon nanodisk on a quartz substrate. 80
Figure 4.3: The modulation depth was calculated separately from a single nanodisk at 300K and 700K. 84
Figure 4.4: Temperature-dependent refractive index of 150 nm thickness silicon nanofilm on quartz at 266 nm wavelength. 85
Figure 4.5: Simulation results of photo-thermo-optical nonlinearity from a single silicon nanodisk of radius 35 nm. 86
Figure 4.6: Spectra of the radius of 35 nm silicon nanodisk at 300K/ 500K/ 700K. 88
Figure 4.7: Relations between the scattering intensity (I_{Sca}), linear intensity (I_L), and nonlinear intensity (I_{NL}). 89
Figure 4.8: SAX microscopy with differential excitation. 90
Figure 4.9: Subtraction signal from linear minus nonlinear signal. 90
Figure 5.1: Sample arrays with different dose times. 93
Figure 5.2: Spectra of shuffled nanodisk arrays measured with silicon mirror as reference background. 94
Figure 5.3: Separated spectra with different doses with silicon mirror. 95
Figure 5.4: Spectra of shuffled nanodisk arrays measured with an aluminum mirror. 96
Figure 5.5: Separated spectra with different doses with aluminum mirror. 97
Figure 5.6: The Spectrum of Array 4 shows a resonance peak at 270 nm. 98
Figure 5.7: Preliminary results of photothermal nonlinearity of shuffled silicon arrays. 99
Figure 5.8: Transmission signal of air (left) and its normalization signal (right) 100
Figure 5.9: Reversibility and repeatability of photothermal nonlinearity of the transmitted signal of the quartz substrate. 101
Figure 5.10: Reversibility and repeatability of silicon's nonlinearity. 102
Figure 5.11: Reversible measurement of silicon signal with a spot size of 2~5 μm. 103
Figure 6.1: Comparing the experimentally measured *n* and *k* at 266 nm 105

doi:10.6342/NTU202501130

Table List

Table 1: A chart for comparing parameters used in the DUV and the visible region 39

doi:10.6342/NTU202501130

Chapter 1. Introduction

1.1 Semiconductor observation: an introduction to imaging techniques

The prospering development of the semiconductor industry endeavors to miniaturize integrated circuits (IC) chips to form a more functional device. One important task in the contemporary semiconductor industry lies in developing methods to inspect structures quickly. Several kinds of electron microscopies are used for inspection, such as scanning electron microscopy (SEM), transmission electron microscopy (TEM), and atomic force microscopy (AFM)[1,2,3]. Even though electron microscopy offers angstrom scale resolution, it has several drawbacks. For example, error sources in electron microscopy, cause drifting, vibrating, beam damaging, charging, and contaminating, which will affect the performance of modern best SEM[4]. Moreover, low throughput due to a small field of view and a high-vacuum condition needs to be improved as well. On the other hand, OM has a much higher throughput due to a larger FOV[5,6,7]. For example, a conventional optical microscope equipped with a standard objective of 20x magnification (MPLN ×20, 0.4 NA, Olympus) microscope is featured by the field of view (FOV) with 1.1-mm-diameter and the space–bandwidth product (SBP) around 7 megapixels[8].

Even though imaging semiconductors with OM is promising, OM is limited by the diffraction limit. The optical diffraction limit[9], *i.e.* the smallest distinguishable distance between two points, was proved by Ernst Abbe in 1873 with the formulation,

$$d = \frac{\lambda}{2n\,sin\theta} = \frac{\lambda}{2NA}. \qquad \text{(eq. 1.2.1)}$$

, where n is the refractive index, λ is the incident wavelength, NA is the numerical aperture, and θ is the angle between the incident light and the normal line.

It is proportional to the wavelength and puts a curb on the spatial resolution around several

doi:10.6342/NTU202501130

hundreds of nanometers when using visible wavelengths. Nowadays, the critical dimension of semiconductors is far smaller than the diffraction limit. For example, finFET keeps decreasing and reached an unprecedented nanometer scale[10,11].

Therefore, it is impractical to use a conventional OM to inspect the state-of-the-art electronic chips and a breakthrough of resolution limit is desired. The technique that breaks through diffraction limits is called super-resolution optical microscopy[12,13].

1.2 Super-resolution imaging based on silicon nonlinear scattering

There are several super-resolution optical microscopies to reach spatial resolving power beyond the diffraction limit. Contemporary techniques include stimulated emission depletion microscopy (STED)[14], stochastic optical reconstruction microscopy (STORM)[15], photo-activated localization microscopy (PALM)[16], and saturated excitation (SAX)[17] microscopy. Most of them involve fluorescence as a contrast probe. Samples under observation are usually fluorescently labeled bio-samples. However, when we wanted to observe silicon with these mature techniques, we found difficulty in the fluorescence labeling of IC chips. In 2022, a paper proposed a super-resolution imaging technique that combined a fault localization method, called laser probing, with an algorithmic method to achieve beam positioning accuracy of better than 10 nm[18]. In detail, laser probing wavefronts in the neighborhood are extracted and correlated, yet parallel transistors might show no difference, causing a flaw in this method. Additionally, with a shorter wavelength of the laser probing technique, optical resolution is enhanced more than twofold and reduces crosstalk, even though the resolving thickness of the Si substrate is restricted by large absorption.

Different from the algorithmic method of laser probing for increasing lateral

doi:10.6342/NTU202501130

resolution, the results published in our group took good use of the inherent properties of a single silicon nanoparticle to demonstrate super-resolution imaging in simulation at DUV wavelength. Our team strives to develop a real-time method for imaging silicon nanostructure in the DUV region to break beyond the optical resolution limit with a large throughput.

One possible method of our proposed label-free super-resolution imaging technique is using saturated excitation (SAX) microscopy. In 2014, the first super-resolution imaging based on plasmonic scattering: plasmonic saturated excitation (p-SAX) microscopy was invented[19] for imaging a single gold nanoparticle. With visible p-SAX microscopy, spatial resolution was enhanced by three-fold, as shown in Figure 1.1[20]. Near-infrared p-SAX microscopy provides both contrast and resolution enhancement over 400 μm depth in a tissue phantom from gold nanoshells[21], as shown in Figure 1.1 I. Inspired by super-resolution imaging using a single gold nanoparticle, we explored applying SAX microscopy for real-time imaging of Si-based chips at DUV wavelengths, where c-Si behaves as a polaritonic material.

doi:10.6342/NTU202501130

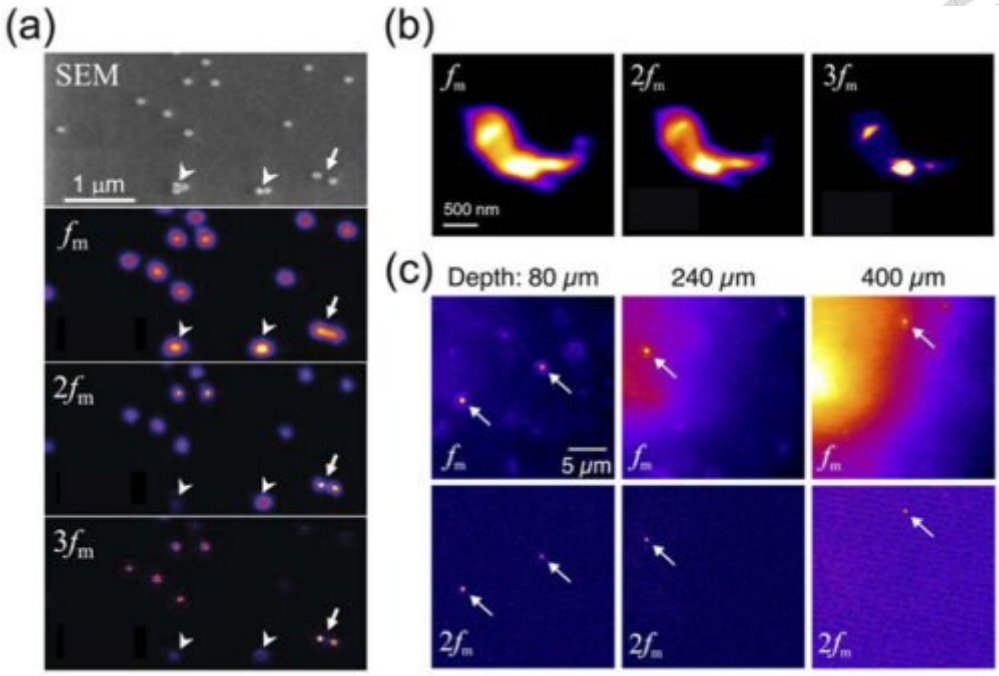

Figure 1.1: Super-resolution imaging of p-SAX microscopy. (a) SEM image and p-SAX images of gold nanoparticles of diameter 100 nm. (b) P-SAX captures imaging of aggregated gold nanostructures. (c) Gold nanoshells distributed in a tissue phantom with different thicknesses of 80 μm, 240 μm, and 400 μm are imaged by p-SAX. Figures in a set were reconstructed by the signal demodulated at f_m, $2f_m$, and $3f_m$. (a)-(c) were reproduced with permission from [20].

Intriguingly, our group found that a silicon nanoparticle excited under visible wavelength exhibits a giant optical nonlinearity[7]. The giant optical nonlinear mechanism is due to the combination of the photothermal and thermo-optic effects, namely photo-thermo-optical nonlinear scattering[22], and the mechanism is shown in Figure 1.2. A single silicon nanoparticle absorbed incident photons to be heated up, temperature changes refractive index, and index variation modifies absorption cross-sections and scattering resonance of a silicon nanostructure. Based on Mie resonance-enhanced efficient heating, a silicon nanoparticle achieves an effective nonlinear refractive index n_2 equivalent to

doi:10.6342/NTU202501130

10^{-1} μm^2/mW. In comparison, bulk silicon has a thermo-optical nonlinear index of n_2 equivalent to 10^{-6} μm^2/mW. By applying enhanced saturated scattering to SAX microscopy for imaging a silicon nanoparticle, the increased nonlinear component enables the extraction of higher-order harmonics, resulting in a smaller point spread function for resolution enhancement and achieving a 132 nm resolution with more than a two-fold improvement[7].

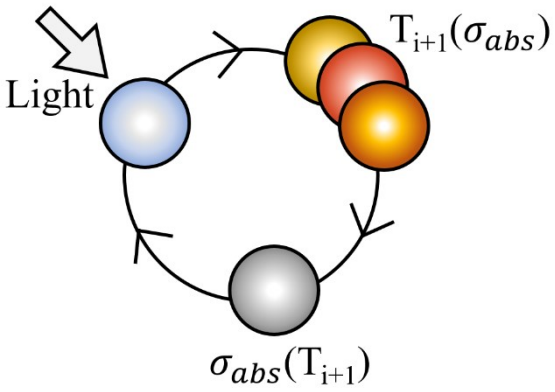

Figure 1.2: Concepts of external heating and self-induced optical heating. It is a recursive method that starts from light heating a nanoparticle with an absorption cross-section spectrum at every new temperature. After heating, the new temperature reaches equilibrium and refreshes the absorption under continuous-wave illumination. The figure was reproduced from [22].

1.3 SAX imaging in the DUV region based on silicon polaritonic resonance enhanced photo-thermo-optical nonlinearity

A key approach to enhancing resolution in SAX microscopy is reducing the wavelength to the DUV region. Our team achieved a 132 nm resolution using SAX in the visible

doi:10.6342/NTU202501130

range, and we now aim to further improve lateral resolution two-fold by shifting to DUV wavelengths. Silicon in the visible region above 550 nm has a large real refractive index (*n*) and a moderate imaginary refractive index (*k*), so it's not hard to find silicon nanostructures that show Mie resonance. A large photothermal nonlinearity was reported to originate from the spectra shifting of a silicon Mie-resonator. When we decrease wavelengths from the visible to the DUV region, the quality factor (Q-factor) of Mie resonance decreases[23]. The reason lies on the change of the optical properties from its wavelength-dependent optical constants demonstrated in Figure 1.3. The reason is based on the skyrocketing k surpassing decreasing n, which results in negative permittivity. Even though the resonance in DUV shows a smaller Q-factor, the negative permittivity in the DUV enables the polaritonic resonance in Si nanostructures. We expect to use the silicon polaritonic resonance to induce thermo-optical nonlinearity to enhance the resolution of SAX in the DUV wavelength.

Related physics for discussing polaritonic resonance starting from plasmonic theory will be given in Ch. 2.2. Different from metals showing negative permittivity based on oscillating free electron gas in conduction bands, silicon shows its polaritonic trait with a resonance peak shown in the DUV region related to interband transitions[24,25,26], as shown in the relative permittivity in Figure 1.3 (b), and a detailed description will be shown in Ch. 2.3.

doi:10.6342/NTU202501130

In the following chapters, I'll discuss the theoretical basics in the sequence of Mie resonance, plasmon resonance, ultraviolet excitation of silicon polaritonic resonance, imaging with SAX microscopy, and the finite-difference time-domain (FDTD) method.

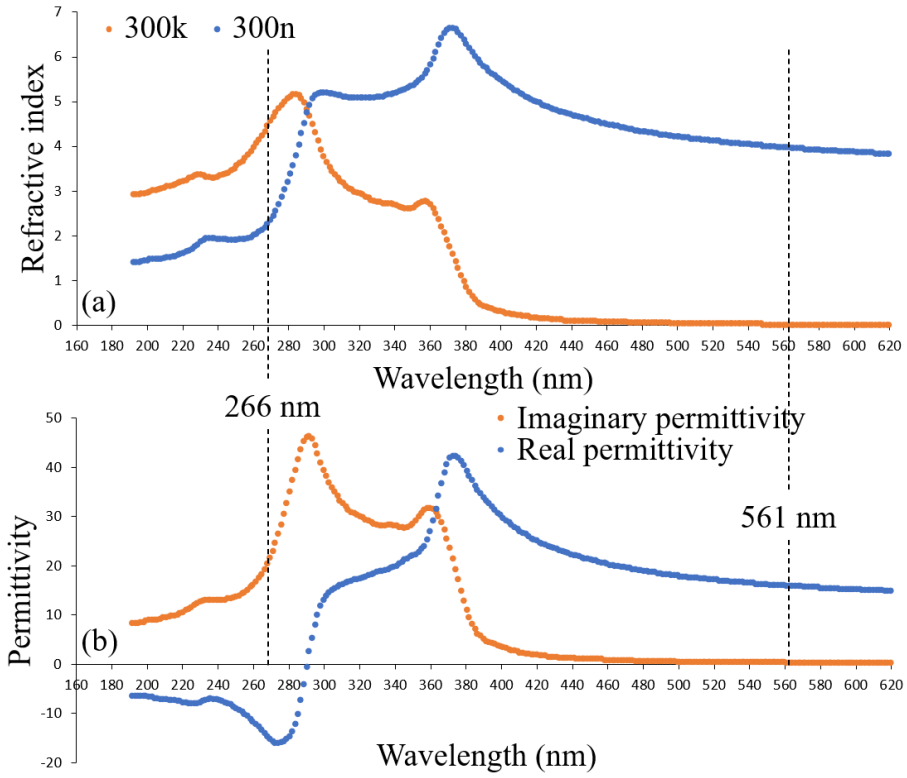

Figure 1.3: The refractive index and permittivity of bulk silicon material measured at a temperature of 300K. (a) The real part of the refractive index (n) is plotted in blue, while the imaginary part (k) is plotted in orange. (b) The real permittivity is plotted in blue, and the imaginary permittivity is plotted in orange. While the permittivity becomes negative, it shows a polaritonic trait alike metal. The refractive index values were reproduced from [7].

doi:10.6342/NTU202501130

Chapter 2. Theory

2.1 Mie resonance: introduction to Mie theory

Scattering originates from heterogeneity, enabling us to distinguish different materials via optical excitation. In the case of dielectrics, incident light oscillates and polarizes the bound electrons inside the material, leading to re-radiation from the atoms, which is called scattering. Scattering intensity is mainly dominated by several factors, such as the particle size ratio and the incident wavelength. In the following discussion, we focused on Mie scattering, as the concept shown in Figure 2.1, in which the size of the particle is roughly in the same order as the wavelength.

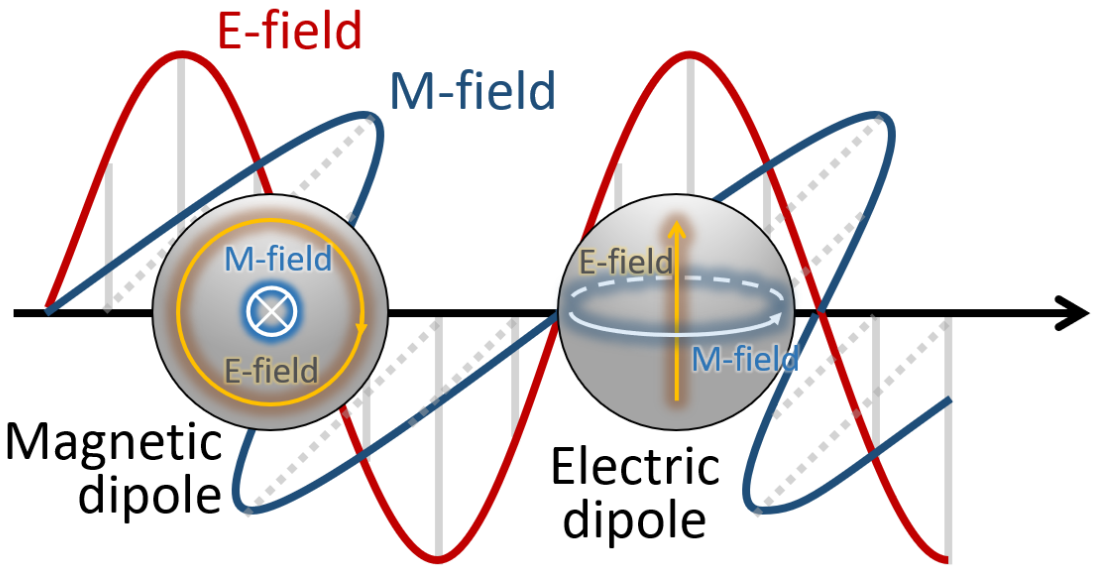

Figure 2.1: Schematic diagram of Mie resonance in a dielectric sphere. Electric dipole and magnetic dipole are characterized by the interaction with incident electromagnetic waves.

In 1871, Lord Rayleigh solved the small particle scattering solution based on Maxwell's equations[27], where the particle size is far smaller than the incident wavelength.

doi:10.6342/NTU202501130

Afterward, Rayleigh's scattering is used to explain why the sky is blue based on the scattering intensity beings 4th-power inversely proportional to the incident wavelength. In the case of the particle of almost the same scale as the incident wavelength, a theory for solving this problem is famously named after Gustav Mie, who published a simulation paper discussing colorful scattering from gold nanoparticles and the corresponding Maxwell's equations in 1908[28]. Unlike Rayleigh scattering, Mie scattering is anisotropic, and its scattering intensity is a complex function of particle size.[29] Kerker documented the history of solving the scattering problem of a sphere[30, 31, 32], in which Mie was not the first to solve the problem [29]. The related scattering theories are named after Mie because his work discussing the color of gold nanoparticles inspired the next generation with the possibility of using resonance nano-scatterer structures to design optical devices, such as an optical antenna, nanoscale sensor, and all-optical modulator. One thing to notice here is that the size-dependent colorful gold spheres were later interpreted in terms of localized surface plasmon resonance (LSPR), which will be discussed in the last part of this section[32].

Mie theory is built on Maxwell's equations with the derivation of the wave equations in spherical coordinates. The commonly used Mie theory is also referred to as Lorenz-Mie theory[33,34] or even Lorenz-Mie-Debye theory[35] for describing plane waves scattered by a homogeneous isotropic sphere[36].

A time-harmonic electromagnetic field in a linear, isotropic, homogeneous medium satisfies the wave equation under consideration,

$$\nabla^2 \boldsymbol{E} + k^2 \boldsymbol{E} = 0. \qquad \text{(eq. 2.1.1)}$$

doi:10.6342/NTU202501130

$$\nabla^2 \boldsymbol{H} + k^2 \boldsymbol{H} = 0. \qquad \text{(eq. 2.1.2)}$$

where $k^2 = \omega^2 \varepsilon \mu$, ($\boldsymbol{k}$ is the wavenumber, ω is the angular frequency, ε is relative permittivity, and μ is permeability.)

and it is divergence-free

$$\nabla \cdot \boldsymbol{E} = 0, \nabla \cdot \boldsymbol{H} = 0. \qquad \text{(eq. 2.1.3)}$$

$\boldsymbol{E}$ and $\boldsymbol{H}$ are related by Maxwell's equations,

$$\nabla \times \boldsymbol{E} = i\omega\mu \boldsymbol{H}, \nabla \times \boldsymbol{H} = -i\omega\varepsilon \boldsymbol{E}. \qquad \text{(eq. 2.1.4)}$$

We can further develop eq. 2.1.4 in spherical coordinates (r, θ, ϕ) with scalar wave equation as,

$$\frac{1}{r^2}\frac{\partial}{\partial r}\left(r^2 \frac{\partial \psi}{\partial r}\right) + \frac{1}{r^2 sin\theta}\frac{\partial}{\partial \theta}\left(sin\theta \frac{\partial \psi}{\partial \theta}\right) + \frac{1}{r^2 sin\theta}\frac{\partial^2 \psi}{\partial \phi^2} + k^2 \psi = 0. \qquad \text{(eq. 2.1.5)}$$

$\psi(r, \theta, \phi) = R(r)\Theta(\theta)\Phi(\phi)$ for separating variables and yielding three equations.

$$\frac{d^2 \Phi}{d\phi^2} + m^2 \Phi = 0, \qquad \text{(eq. 2.1.6)}$$

$$\frac{1}{sin\theta}\frac{d}{d\theta}\left(sin\theta \frac{d\Theta}{d\theta}\right) + \left[n(n+1) - \frac{m^2}{sin^2\theta}\right]\Theta = 0, \qquad \text{(eq. 2.1.7)}$$

$$\frac{d}{dr}\left(r^2 \frac{dR}{dr}\right) + [k^2 r^2 - n(n+1)]R = 0, \qquad \text{(eq. 2.1.8)}$$

Solving these equations, we derived,

$$\psi_{emn} = cos(m\phi)\, P_n^m(cos\theta) z_n(kr), \qquad \text{(eq. 2.1.9)}$$

$$\psi_{omn} = sin(m\phi)\, P_n^m(cos\theta) z_n(kr), \qquad \text{(eq. 2.1.10)}$$

where m is an integer or zero. P_n^m is the associated Legendre functions of degree n and order m, where $n = m, m+1, \ldots$. z_n is any of the four spherical Bessel functions

doi:10.6342/NTU202501130

$j_n, y_n, h_n^{(1)}, h_n^{(2)}$.

$$j_n(\rho) = \sqrt{\frac{\pi}{2\rho}}\, J_{n+1/2}(\rho), \quad \text{(eq. 2.1.11)}$$

$$y_n(\rho) = \sqrt{\frac{\pi}{2\rho}}\, Y_{n+1/2}(\rho), \quad \text{(eq. 2.1.12)}$$

$$h_n^{(1)}(\rho) = j_n(\rho) + iy_n(\rho), \quad \text{(eq. 2.1.13)}$$

$$h_n^{(2)}(\rho) = j_n(\rho) - iy_n(\rho), \text{ where } \rho = kr, \quad \text{(eq. 2.1.14)}$$

The wave equations can be expanded as infinite series based on the completeness of the functions $cos\, m\phi$, $sin\, m\phi$, $P_n^m(cos\theta)$ and $z_n(kr)$. With these, we can expand the vector spherical harmonics, $M_{emn}, M_{omn}, N_{emn}, N_{omn}$.

Therefore, we can start to expand an incident plane x-polarized wave in spherical polar coordinates,

$$E_i = E_0 e^{ikrcos\theta}\widehat{e_x}, \quad \text{(eq. 2.1.15)}$$

where $\widehat{e_x} = sin\theta cos\phi \widehat{e_r} - sin\phi \widehat{e_\phi}$.

The electromagnetic fields at all points of space are expanded based on vector spherical harmonics. Expanding (eq. 2.1.15) in spherical harmonics, we have

$$E_i = \sum_{m=0}^{\infty}\sum_{n=m}^{\infty}(B_{emn}M_{emn} + B_{omn}M_{omn} + A_{emn}N_{emn} + A_{omn}N_{omn}), \quad \text{(eq. 2.1.16)}$$

with the orthogonality relations of all vector spherical harmonics and the orthogonality of sine and cosine, we proceed with the form

doi:10.6342/NTU202501130

$$B_{emn} = \frac{\int_0^{2\pi}\int_0^{\pi} E_i \cdot M_{emn} sin\theta \; d\theta d\phi}{\int_0^{2\pi}\int_0^{\pi} |M_{emn}|^2 sin\theta \; d\theta d\phi}, \quad \text{(eq. 2.1.17)}$$

and similar expressions for $B_{omn}, A_{emn},$ and A_{omn}.

$B_{emn} = A_{omn} = 0$ for all m and n, based on the orthogonality of M_{emn}, N_{omn} and $\widehat{e_x}$.

The same reason also renders the remaining coefficient vanishes unless $m = 1$.

With the condition that the incident field is finite at the origin, $j_n(\rho)$ the suitable spherical Bessel function with subscripts (1) to choose among the generating functions ψ_{o1n} , ψ_{e1n}. y_n would be eliminated in this case.

Therefore, we have the expansion in the form of

$$E_i = \sum_{n=1}^{\infty}(B_{o1n} M_{o1n}^{(1)} + A_{e1n} N_{e1n}^{(1)}). \quad \text{(eq. 2.1.18)}$$

Solving the numerical part containing the Legendre polynomials,

$$\int_0^{\pi} \frac{d}{d\theta}(sin\theta P_n^1) e^{i\rho \, cos\theta} d\theta, \text{ with } P_n^1 = -\frac{dP_n}{d\theta}, \quad \text{(eq. 2.1.19)}$$

we obtain the form,

$$B_{o1n} = i^n E_0 \frac{2n+1}{n(n+1)}, \text{ and } A_{e1n} = -iE_0 i^n \frac{2n+1}{n(n+1)}. \quad \text{(eq. 2.1.20)}$$

Hence, we obtained the expansion of a plane wave in spherical harmonics. For convenience, we change the symbol to

$E_0 M_{o1n}^{(1)} \equiv M_n^{(1)}(r)$, and $E_0 N_{e1n}^{(1)} \equiv N_n^{(1)}(r)$, yielding

$$E_i = E_0 \sum_{n=1}^{\infty} i^n \frac{2n+1}{n(n+1)} (M_{o1n}^{(1)} - iN_{e1n}^{(1)}) = \sum_{n=1}^{\infty} i^n \frac{2n+1}{n(n+1)} (M_n^{(1)}(r) - iN_n^{(1)}(r)), \quad \text{(eq. 2.1.21)}$$

doi:10.6342/NTU202501130

with its curl, we have the magnetic field,

$$H_i = -\frac{k}{\omega\mu} E_0 \sum_{n=1}^{\infty} i^n \frac{2n+1}{n(n+1)} (M_{e1n}^{(1)} + iN_{o1n}^{(1)}) = -\frac{k}{\omega\mu} \sum_{n=1}^{\infty} i^n \frac{2n+1}{n(n+1)} (M_n^{(1)}(r) + iN_n^{(1)}(r)). \quad \text{(eq. 2.1.22)}$$

With the boundary conditions indicating a continuous field, we can derive the scattering field and field inside the particle. Two other fields are of interest, scattering fields $E_s(r)$ and $H_s(r)$ outside the particle and resonant field $E_p(r)$ and $H_p(r)$ inside the particle. An incident field is represented as $E_i(r)$ and $H_i(r)$. We want to expand them to a linear combination of $M_n^{(1)}(r)$ and $N_n^{(1)}(r)$.

$$(E_i(r) + E_s(r) - E_p(r)) \times e_r = 0, \quad \text{(eq. 2.1.23)}$$

$$(H_i(r) + H_s(r) - H_p(r)) \times e_r = 0. \quad \text{(eq. 2.1.24)}$$

$$r = a.$$

We expressed them in the linear combination of $M_n^{(1)}(r)$ and $N_n^{(1)}(r)$. Only the Bessel function of the first kind takes use of $z(\rho)$ that can suitably represent the field inside the particle, $E_p(r)$ and $H_p(r)$, like the incident plane wave.

$$E_p(r) = \sum_n^{\infty} i^n \frac{2n+1}{n(n+1)} (c_n M_n^{(1)}(r) - id_n N_n^{(1)}(r)), \quad \text{(eq. 2.1.25)}$$

$$H_p(r) = -\frac{k}{\omega\mu} \sum_n^{\infty} i^n \frac{2n+1}{n(n+1)} (d_n M_n^{(1)}(r) + ic_n N_n^{(1)}(r)), \quad \text{(eq. 2.1.26)}$$

where c_n and d_n are the constants for $M_n^{(1)}(r)$ and $N_n^{(1)}(r)$, respectively.

doi:10.6342/NTU202501130

The expressions for the scattered field should be represented by sphere Hankel functions $h_n^{(3)}$ $h_n^{(4)}$ because they don't exist at the origin. They are approximated in the vicinity of infinity as follows,

$h_n^{(3)}(kr) \sim \frac{(-i)^{n+1}}{kr} e^{ikr}$, indicating the wave propagates outward the particle.

$h_n^{(4)}(kr) \sim \frac{i^{n+1}}{kr} e^{ikr}$, indicating the wave propagates inward the particle.

Because the scattered field propagates outward the particle, $M_n^{(3)}(r)$ and $N_n^{(3)}(r)$ are under consideration based on $h_n^{(3)}$.

$$E_s(r) = -\sum_n^{\infty} i^n \frac{2n+1}{n(n+1)} (a_n M_n^{(3)}(r) - i b_n N_n^{(3)}(r)), \quad \text{(eq. 2.1.27)}$$

$$H_s(r) = \frac{k}{\omega\mu} \sum_n^{\infty} i^{n+1} \frac{2n+1}{n(n+1)} (b_n M_n^{(3)}(r) + i a_n N_n^{(3)}(r)), \quad \text{(eq. 2.1.28)}$$

where a_n and b_n are the constants for $M_n^{(3)}(r)$ and $N_n^{(3)}(r)$.

In the final step, we want to solve a_n and b_n to evaluate the scattering efficiency. By solving the equations with boundary conditions on the particle surface and eliminating c_n and d_n by Riccati-Bessel functions, and $\rho = k_m r = \frac{2\pi n_p r}{\lambda_m}$, $m = \frac{k_p}{k_m} = \frac{n_p}{n_m}$

The boundary conditions are[37]:

$$\psi_n(m\rho) c_n + \xi_n(\rho) b_n = \psi_n(\rho), \quad \text{(eq. 2.1.29)}$$

$$\psi'_n(m\rho) c_n + \xi'_n(\rho) b_n = \psi_n(\rho), \quad \text{(eq. 2.1.30)}$$

doi:10.6342/NTU202501130

$$\psi_n(m\rho)d_n + \xi_n(\rho)a_n = \psi_n(\rho), \quad \text{(eq. 2.1.31)}$$

$$\psi'_n(m\rho)d_n + m\xi'_n(\rho)a_n = m\psi'_n(\rho), \quad \text{(eq. 2.1.32)}$$

where $m = \frac{n_p}{n_m}$ is the refractive index ratio between the particle and the outside medium.

The Riccati-Bessel functions are[37]:

$$\psi_n(\rho) = \rho j_n(\rho), \quad \text{(eq. 2.1.33)}$$

$$\xi_n(\rho) = \rho h_n^{(3)}(\rho), \quad \text{(eq. 2.1.34)}$$

$$\psi'_n(\rho) = \frac{\partial}{\partial\rho}(\rho j_n(\rho)), \quad \text{(eq. 2.1.35)}$$

$$\xi'_n(\rho) = \frac{\partial}{\partial\rho}(h_n^{(3)}(\rho)), \quad \text{(eq. 2.1.36)}$$

We can therefore represent a_n and b_n as,

$$a_n = \frac{\psi_n(m\rho)\psi'_n(\rho) - m\psi_n(\rho)\psi'_n(m\rho)}{\psi_n(m\rho)\xi'_n(\rho) - \xi_n(\rho)\psi'_n(m\rho)}, \quad \text{(eq. 2.1.37)}$$

$$b_n = \frac{m\psi_n(m\rho)\psi'_n(\rho) - \psi_n(\rho)\psi'_n(m\rho)}{m\psi_n(m\rho)\xi'_n(\rho) - \xi_n(\rho)\psi'_n(m\rho)}. \quad \text{(eq. 2.1.38)}$$

Supposing the surrounding medium is non-absorbing, the electromagnetic energy flowing through the particle surface is independent of the radius of the imaginary sphere, which also enables the far-field approximation. Therefore, we have the representation for the scattering cross-section, C_{sca}, and absorption coefficient, C_{abs} with Mie coefficients, a_n and b_n.

doi:10.6342/NTU202501130

$$C_{sca} = \frac{2\pi}{k^2}\sum_{n}^{\infty}(2n+1)(|a_n|^2 + |b_n|^2), \quad \text{(eq. 2.1.39)}$$

$$C_{ext} = \frac{2\pi}{k^2}\sum_{n}^{\infty}(2n+1)Re(a_n + b_n), \quad \text{(eq. 2.1.40)}$$

$$C_{abs} = C_{ext} - C_{sca}. \quad \text{(eq. 2.1.41)}$$

The lowest order resonance mode is the electric dipole (ED) with $n = 1$. With proper simplification on the Riccati-Bessel function by assuming that a nanoparticle is very small[38] (dimensions below 100 nm) compared to the wavelength, and the wavenumber of a medium is $k_m = \frac{2\pi}{\lambda_m} \ll 1$, deriving the ED mode for connecting Mie resonance to plasmon resonance is demonstrated from eq. 2.1.42 to eq. 2.1.49.

Noting that $m = \frac{n_p}{n_m}$, where n_p is the refractive index of a nanoparticle and n_m comes from the outside environment. Remaining terms of order 3 in Riccati-Bessel function leads to ρ^3, a_n and b_n with the simplified term of a_1 and b_1 without the existence of the higher order terms[38],

$$a_1 \approx -\frac{i2\rho^3}{3}\frac{m^2-1}{m^2+2}, \quad \text{(eq. 2.1.42)}$$

$$b_1 \approx 0. \quad \text{(eq. 2.1.43)}$$

The disappearance of b_1 means a lack of magnetic dipole.

Substituting $m = \frac{n_R + in_I}{n_m}$, leads to

doi:10.6342/NTU202501130

$$a_1 = -i\,\frac{2\rho^3}{3}\,\frac{{n_R}^2 - {n_I}^2 + i2n_R n_I - {n_m}^2}{{n_R}^2 - {n_I}^2 + i2n_R n_I + 2{n_m}^2},$$ (eq. 2.1.44)

, and $$a_1 = \frac{2\rho^3}{3}\frac{-i{\varepsilon_1}^2 - i\varepsilon_1\varepsilon_m + 3\varepsilon_2\varepsilon_m - i{\varepsilon_2}^2 + i2{\varepsilon_m}^2}{(\varepsilon_1+2\varepsilon_m)^2+(\varepsilon_2)^2},$$ (eq. 2.1.45)

through the complex dielectric function of metal with $\tilde{\varepsilon} = \varepsilon_1 + i\varepsilon_2$ and $\varepsilon_m = {n_m}^2$.

$$\varepsilon_1 = {n_R}^2 - {n_I}^2,\ \varepsilon_2 = 2n_R n_I\ ,$$ (eq. 2.1.46) and (eq. 2.1.47)

We obtain the expressions of C_{ext} and C_{sca} for the most commonly observed localized surface plasmon resonance (LSPR), where massive electrons lie in the conduction band.

$$C_{ext} = \frac{18\pi{\varepsilon_m}^{3/2}V}{\lambda^2}\frac{\varepsilon_2(\lambda)}{[\varepsilon_1(\lambda)+2\varepsilon_m]^2+\varepsilon_2(\lambda)^2},$$ (eq. 2.1.48)

$$C_{sca} = \frac{32\pi^4{\varepsilon_m}^2V^2}{\lambda^2}\frac{(\varepsilon_1-\varepsilon_m)^2+(\varepsilon_2)^2}{(\varepsilon_1+2\varepsilon_m)^2+(\varepsilon_2)^2}.$$ (eq. 2.1.49)

The extinction cross-section is maximized when $\varepsilon_1 = -2\varepsilon_m$, explaining the dependence of the LSPR extinction peak on the surrounding dielectric environment.

Simply put, Mie theory provides a mathematical framework for describing the absorption and scattering of small spheres with arbitrary radii and refractive indices. Scattering can be calculated through the superposition of Mie modes in a scatterer with different indices for a_n and b_n[37,38,39].

Moreover, the assumption of small size-wavelength ratio for a Mie resonator helps to purify multiple Mie modes to the electric dipole resonance with a simplification on the Ricatti-Bessel functions for deriving eq. 2.1.42 and eq. 2.1.43. In the following section 2.2, this assumption is also beneficial for representing an ideal dipole for describing the scattering cross-sections in eq. 2.2.3 and eq. 2.2.4, where we neglected the explanation of the ideal dipole moment used in Φ_{out}, as demonstrated in Maier[37].

doi:10.6342/NTU202501130

2.2 Types of surface polaritons (SPs) at the semiconductor-insulator surface

A polariton[40] is formed by a hybrid quasiparticle with photons coupling between the electromagnetic wave and electric dipoles in a material, such as an optical phonon activated in infrared, excitons in semiconductors, or plasmons in doped materials[41]. To excite the surface polaritons, it suffices to satisfy the condition of

$$Re[\varepsilon(\omega)] \cdot \varepsilon_m < 0 \qquad \text{(eq. 2.2.1)}$$

with a negative $Re[\varepsilon(\omega)]$, such as silicon in DUV region.

Our discussion here is focused on the excitation of interband-transition-driven surface polaritons in Si (containing a-Si and c-Si) nanostructures at DUV region- by considering a sphere of a diameter d, much smaller than the wavelength, λ. This assumption is used in a classical plasmon theory for ignoring the phase and fields distribution in a particle of dimensions below 100 nm. In general, localized surface polariton resonance is considered a branch of Mie resonance. This assumption helps isolate the electric dipole mode from overlapping modes in classical Mie theory[38]. The second usage of this condition is to represent an ideal dipole for the convenience of mathematical analysis.

From solving the boundary condition of electrostatic problems involving dielectrics, where inside and outside the sphere have no free charges[42]. Inside the sphere, there are constant electric field parallel to the applied field and an electric dipole located

doi:10.6342/NTU202501130

at the center, which is represented as $\boldsymbol{p} = 4\pi\varepsilon_0\varepsilon_m a^3 \frac{\varepsilon-\varepsilon_m}{\varepsilon+2\varepsilon_m}\boldsymbol{E_0}$, where ε_0 is the dielectric constant of the free space, and ε_m is that of the surrounding medium. E_0 is the amplitude of the incident electric field, and α is the polarizability of the nanosphere, defined by

$$\alpha = 4\pi r^3 \frac{\varepsilon(\omega)-\varepsilon_m}{\varepsilon(\omega)+2\varepsilon_m} \qquad \text{(eq. 2.2.2)}$$

, where $\varepsilon(\omega)$ is the dielectric function of the nanosphere dependent on the angular frequency, ω, of the incident light, and r is the radius of the dielectric sphere.

The corresponding cross sections for scattering (C_{sca}) and absorption (C_{abs}) is calculated via the Poynting-vector determined from the electromagnetic fields associated with an oscillating electric dipole with corresponding total fields, represented as

$$C_{sca} = \frac{k^4}{6\pi}|\alpha|^2 = \frac{8\pi}{3}k^4a^6\left|\frac{\varepsilon-\varepsilon_m}{\varepsilon+2\varepsilon_m}\right|^2 \qquad \text{(eq. 2.2.3)}$$

$$C_{abs} = k\mathrm{Im}[\alpha] = 4\pi k a^3 \mathrm{Im}[\frac{\varepsilon-\varepsilon_m}{\varepsilon+2\varepsilon_m}]. \qquad \text{(eq. 2.2.4)}$$

The Frohlich condition for describing the resonance of dipole surface polaritons of the silicon at DUV is deduced from C_{sca}, and gives

$$Re[\varepsilon(\omega)] = -2\varepsilon_m. \qquad \text{(eq. 2.2.5)}$$

, based on explaining the resonance condition of minimizing $|\varepsilon + 2\varepsilon_m|$ with a slowly-varying $Im[\varepsilon]$ around the resonance.

doi:10.6342/NTU202501130

The material absorption is represented by the absorbed energy, A_{abs}, which is proportional to the imaginary part of the dielectric function, $Im[\varepsilon(\omega)]$, and is described by

$$A_{abs} \propto Im[\varepsilon(\omega)]|E_0|^2 \quad \text{(eq. 2.2.6)}$$

Turning back to discuss the negative permittivity of silicon in the DUV region, where strong interband transitions resulted in the increasing absorption that leads to the negative $Re[\varepsilon(\omega)]$, going with an increase in $Im[\varepsilon(\omega)]$, featured by higher absorption.

Kramers-Kronig relations properly link the real part and the imaginary part of the dielectric functions:

$$Re[\varepsilon(\omega)] = 1 + \frac{2}{\pi} P \int_0^\infty \frac{\omega' \cdot \mathrm{Im}[\varepsilon(\omega')]}{\omega'^2 - \omega^2} d\omega'$$

$$Im[\varepsilon(\omega)] = -\frac{2\omega}{\pi} P \int_0^\infty \frac{Re[\varepsilon(\omega')] - 1}{\omega'^2 - \omega^2} d\omega'$$

, where P is the Cauchy principal value integral. From these relations, an interband transition causing increment in $Im[\varepsilon(\omega)]$ results in a decrease of $Re[\varepsilon(\omega)]$. Therefore, once the interband transition strength is high enough, $Re[\varepsilon(\omega)]$ experiences a sudden drop and falls to be negative value, which meets the case for silicon in the DUV regime.

Moreover, polaritons in layered two-dimensional materials are mainly classified as plasmon polaritons (PPs), phonon polaritons (PhPs), and exciton polaritons (EPs). Propagating polaritons indicate electromagnetic modes confined in an interface composed of materials of a positive and a negative permittivity with evanescent

doi:10.6342/NTU202501130

electromagnetic waves propagating along the direction perpendicular to the surface. Three types of surfaces related to polaritons in crystalline silicon (c-Si) are briefly discussed below.

Surface plasmon polaritons (SPPs) are the most widely discussed among the three types of polaritons. The system for discussing SPP is applied to the flat interface between a conductor and a dielectric. Here, we characterized the surface excitations in terms of their dispersion and spatial profile with a brief discussion of the field enhancement, starting from the wave equation. ε is the complex dielectric function, which could be discussed in detail under different conditions. $\varepsilon_0 \approx 8.854 \times 10^{-12} F/m$, is named vacuum permittivity. $\mu_0 \approx 1.257 \times 10^{-6} H/m$, is named vacuum permeability. Light speed is defined as $c = \frac{1}{\sqrt{\varepsilon_0 \mu_0}} \approx 2.99752353 \times 10^8$. By identifying $\nabla \times \nabla \times \boldsymbol{E} \equiv \nabla(\nabla \cdot \boldsymbol{E}) - \nabla^2 \boldsymbol{E}$ as well as $\nabla \cdot (\varepsilon \boldsymbol{E}) \equiv \boldsymbol{E} \cdot \nabla \varepsilon + \varepsilon \nabla \cdot \boldsymbol{E}$, rendering

$$\nabla \times \nabla \times \boldsymbol{E} = -\mu_0 \frac{\partial^2 \boldsymbol{D}}{\partial t^2}, \qquad \text{(eq. 2.2.7)}$$

$$\nabla(\nabla \cdot \boldsymbol{E}) - \nabla^2 \boldsymbol{E} = -\mu_0 \varepsilon_0 \varepsilon \frac{\partial^2 \boldsymbol{E}}{\partial t^2}, \qquad \text{(eq. 2.2.8)}$$

$$\nabla\left(\frac{1}{\varepsilon}[\nabla \cdot (\varepsilon \boldsymbol{E}) - \boldsymbol{E} \cdot \nabla \varepsilon]\right) - \nabla^2 \boldsymbol{E} = -\mu_0 \varepsilon_0 \varepsilon \frac{\partial^2 \boldsymbol{E}}{\partial t^2}, \qquad \text{(eq. 2.2.9)}$$

devoid of inhomogeneity in materials with $\nabla \cdot \varepsilon = 0$ leading to $\nabla \cdot \boldsymbol{D} = 0$, where **D** is the dielectric displacement of linear, isotropic and nonmagnetic media, defined as

$$\boldsymbol{D} = \varepsilon_0 \varepsilon \boldsymbol{E} = \varepsilon_0 \boldsymbol{E} + \boldsymbol{P} = (1 + \chi)\boldsymbol{E}. \qquad \text{(eq. 2.2.10)}$$

, where $\boldsymbol{P}$ represents the electric dipole moment per unit volume, caused by the

doi:10.6342/NTU202501130

alignment of microscopic dipoles with the electric field.

Thus, it leads to

$$\nabla\left(-\frac{1}{\varepsilon}\boldsymbol{E}\cdot\nabla\varepsilon\right)-\nabla^2\boldsymbol{E}=-\mu_0\varepsilon_0\varepsilon\frac{\partial^2\boldsymbol{E}}{\partial t^2}, \quad \text{(eq. 2.2.11)}$$

Since ε is neglected, we obtained

$$\nabla^2\boldsymbol{E}-\frac{\varepsilon}{c^2}\frac{\partial^2\boldsymbol{E}}{\partial t^2}=0. \quad \text{(eq. 2.2.12)}$$

Considering a time-harmonic electromagnetic field with $\boldsymbol{E}(\boldsymbol{r},t)=\boldsymbol{E}(\boldsymbol{r})e^{-i\omega t}$ yields *Helmholtz equation*,

$$\nabla^2\boldsymbol{E}+k_0^2\varepsilon\boldsymbol{E}=0. \quad \text{(eq. 2.2.13)}$$

where $k_0=\frac{\omega}{c}$ is the propagating wave vector in vacuum.

Describe the electromagnetic field in Cartesian coordinate with $E(x,y,z)=E(z)e^{-i\beta x}=E(z)e^{-ik_x x}$, in which β is called the *propagation constant* of the traveling waves for an infinite long metal film by assuming

$$\frac{\partial^2\boldsymbol{E_x}(z)}{\partial z^2}+(k_0^2\varepsilon-\beta^2)\boldsymbol{E_x}=0. \quad \text{(eq. 2.2.14)}$$

As for the magnetic field $H(x,y,z)=H(z)e^{i\beta y}=H(z)e^{ik_y y}$, yielding the form of

$$\frac{\partial^2\boldsymbol{H_y}(z)}{\partial z^2}+(k_0^2\varepsilon-\beta^2)\boldsymbol{H_y}=0. \quad \text{(eq. 2.2.15)}$$

The mentioned electromagnetic wave demonstrated in (eq. 2.2.15) is also called the transverse magnetic modes (TM or p) modes, corresponding to the electric field demonstrated in (eq. 2.2.14).

Recalling Faraday-Lentz's law as $\nabla\times\boldsymbol{E}=-\frac{\partial\boldsymbol{B}}{\partial t}$, (eq. 2.2.16)

doi:10.6342/NTU202501130

and Ampere's law as $\nabla \times \boldsymbol{H} = J_{ext} + \frac{\partial \boldsymbol{D}}{\partial t}$. (eq. 2.2.17)

Remembering $\boldsymbol{D} = \varepsilon_0 \varepsilon \boldsymbol{E}$ and $\boldsymbol{B} = \mu_0 \mu \boldsymbol{H}$.

For harmonic time dependence, it goes with $\frac{\partial}{\partial t} = -i\omega$.

Following curl equations demonstrated in (eq. 2.2.16) and (eq. 2.2.17), we derive

$\frac{\partial E_z}{\partial y} - \frac{\partial E_y}{\partial z} = i\omega\mu_0 H_x;$

$\frac{\partial E_x}{\partial z} - \frac{\partial E_z}{\partial x} = i\omega\mu_0 H_y;$

$\frac{\partial E_y}{\partial x} - \frac{\partial E_x}{\partial y} = i\omega\mu_0 H_z.$

And the corresponding equations for magnetic fields

$\frac{\partial H_z}{\partial y} - \frac{\partial H_y}{\partial z} = -i\omega\varepsilon_0 \varepsilon E_x;$

$\frac{\partial H_x}{\partial z} - \frac{\partial H_z}{\partial x} = -i\omega\varepsilon_0 \varepsilon E_y;$

$\frac{\partial H_y}{\partial x} - \frac{\partial H_x}{\partial y} = -i\omega\varepsilon_0 \varepsilon E_z.$

For $z > 0$, it shows

$$H_y(z) = A_2 e^{i\beta x} e^{-k_2 z},$$

$$E_x(z) = iA_2 \frac{1}{\omega\varepsilon_0\varepsilon_2} k_2 e^{i\beta x} e^{-k_2 z}, \quad \text{(eq. 2.2.18)}$$

$$E_z(z) = -A_1 \frac{\beta}{\omega\varepsilon_0\varepsilon_2} e^{i\beta x} e^{-k_2 z}.$$

For $z < 0$, it shows

$$H_y(z) = A_1 e^{i\beta x} e^{k_1 z},$$

$$E_x(z) = -iA_1 \frac{1}{\omega\varepsilon_0\varepsilon_1} k_1 e^{i\beta x} e^{k_1 z}, \quad \text{(eq. 2.2.19)}$$

$$E_z(z) = -A_1 \frac{\beta}{\omega\varepsilon_0\varepsilon_1} e^{i\beta x} e^{k_1 z}.$$

doi:10.6342/NTU202501130

First of all, we discuss only metal-dielectric interface with inherently positive real dielectric constant (or permittivity) ε_2 and that of complex dielectric constant for metallic of $Re[\varepsilon_1] < 0$. Noting that $k_i \equiv k_{z,i}(i = 1, 2)$ follows the wave vector perpendicular to the interface of material with ε_1 and ε_2. In the meantime, defines the evanescent decay length of the fields $\hat{z} = 1/|k_z|$, called reciprocal value acting as the ability for confining the wave in the perpendicular direction.

With the boundary condition $A_1 = A_2$, it leads to

$$\frac{k_2}{k_1} = -\frac{\varepsilon_2}{\varepsilon_1} \qquad \text{(eq.2.2.20)}$$

, which also indicates that the surface wave exists only at interfaces between materials with opposite signs of dielectric permittivity, the same as the demonstrated conductor-insulator surface.

Replacing (eq. 2.4.12), (eq. 2.4.13) and (eq. 2.4.14) into (eq. 2.4.9) leads to

$$k_i^2 = \beta^2 - k_0^2 \varepsilon_i \qquad \text{(eq.2.2.21)}$$

, where $k_0 = 2\pi/\lambda$ means the vacuum wave number.

Combining (eq.2.4.15) and (eq. 2.4.14) derives the dispersion relation of propagating SPPs at the interface

$$k_{sp} = \beta = k_0 \sqrt{\frac{\varepsilon_1 \varepsilon_2}{\varepsilon_1 + \varepsilon_2}}. \qquad \text{(eq. 2.2.22)}$$

It doesn't matter whether the permittivity of metal, $\varepsilon_1(\omega)$, is real or complex number going with a term for dissipation, the surface plasmonic dispersion relation is

doi:10.6342/NTU202501130

accomplished.

Secondly, we briefly discuss the transverse electric mode (TE mode) and its possibility of initiating the surface plasmon polariton on the metal-insulator surface. It turns out that there is no possibility with a pure transverse electric wave.

Specifying the electromagnetic wave in the region of $z > 0$ gives

$$E_y(z) = A_2 e^{i\beta x} e^{-k_2 z},$$
$$H_x(z) = -iA_2 \frac{1}{\omega\mu_0} k_2 e^{i\beta x} e^{-k_2 z}, \qquad \text{(eq. 2.2.23)}$$
$$H_z(z) = A_1 \frac{\beta}{\omega\mu_0} e^{i\beta x} e^{-k_2 z}.$$

For $z < 0$, it goes with

$$E_y(z) = A_1 e^{i\beta x} e^{k_1 z},$$
$$H_x(z) = iA_1 \frac{1}{\omega\mu_0} k_1 e^{i\beta x} e^{k_1 z}, \qquad \text{(eq. 2.2.24)}$$
$$H_z(z) = A_1 \frac{\beta}{\omega\mu_0} e^{i\beta x} e^{k_1 z}.$$

From the continuity of E_y and H_x gives

$$A_1(k_1 + k_2) = 0. \qquad \text{(eq. 2.2.25)}$$

Since it requires k_1 and k_2 as the confinement on the surface, the only existing solution is $A_1 = A_2 = 0$. It indicates that surface polaritons can only be excited by TM polarization rather that TE mode.

However, the material we are concerned about is silicon, which is not a standard metal. Interestingly, silicon has negative relative permittivity, making it an optical

doi:10.6342/NTU202501130

polaritonic material in the DUV region. Therefore, it is better to include surface phonon polariton and surface exciton polariton based on the multiple indirect band gap transitions (demonstrated in section 2.4) and the intrinsic electron-hole pair in the bulk c-Si.

Surface phonon polariton arises from coupling the electromagnetic field to lattice vibrations of polar dielectrics, such as SiC, at infrared frequencies. Silicon is not a polar dielectric, but it still demonstrates insulator behaviors and an induced dipole moment. Therefore, all facts indicate that c-Si contains more than one kind of polaritons[49,50].

In 2025, an ultra-thin layer of a-Si showed the possibility of exciting long-range surface polaritons (LRSPs) in the visible and ultraviolet region at which a-Si is a strongly absorbing dielectric[43]. Secondly, the pioneering work published in 1990 by *Yang et al.*[44] already demonstrated the excitation of LRSPs in thin films at the infrared wavelength at which the material behaves as a strongly absorbing dielectric. Hence, it is promising that other strongly absorbing dielectric materials, such as c-Si at DUV wavelength, might show similar effects. Thirdly, by comparing the refractive index of a-Si to that of c-Si, c-Si has an even sharper positive real and a larger imaginary part of the refractive index from the wavelength 290 nm to 380 nm. With a shorter wavelength below 290 nm, not only a-Si but also c-Si demonstrate a negative permittivity, behaving as a strongly absorbing dielectric. Yet, both materials go with a negative permittivity and obey what KK-relation[45] told us that a peak in the imaginary part of the dielectric function, ε''_1,

doi:10.6342/NTU202501130

leads to a jump in the real part, ε'_1, as demonstrated as Figure 1.3. What's more, when the electrons are excited from the valence band to the conduction band, strong interband transition leads to negative permittivity with large absorption. Moreover, when an electron goes from the valence band to the conduction band[49,50], leaving a hole in the valence band, the negatively charged electron and the positively charged hole form a bound state. This kind of electron-hole pair quasiparticle is called an exciton.

Last but not least, surface exciton polaritons are elementary excitations propagating along the boundary between a dielectric medium and a Wannier-type crystal excited in bulk. In general, elementary excitations are classified into three parts: the lattice vibrations described by phonons, the collective vibrations of free electrons in the conduction band named plasmons, and the excitation of the electron-hole excitations described by excitons. Therefore, the thin bulk c-Si[46] surface immersed in the air is suitable to be described by three kinds of polaritons[47] rather than one of them.

doi:10.6342/NTU202501130

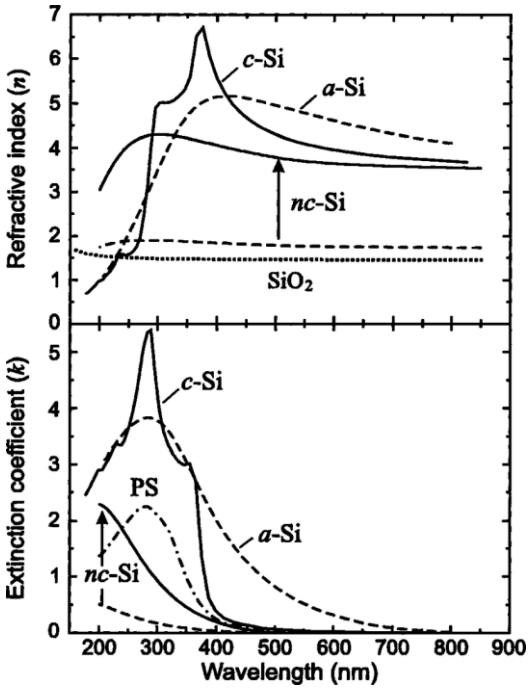

Figure 2.2: A comparison of c-Si and a-Si with their real (n) and imaginary parts (extinction coefficient, k) of the refractive index. The figure was reproduced from [48]. The n and k follow the KK-relation, which endows a peak in the real part lying in a slightly larger wavelength than the peak of the imaginary part of materials.

In brief, the conclusion of section 2.2 was corrected to a more general term for c-Si as "localized surface polariton resonance" to suit the physical properties, with the assumption of a much smaller size of the nanoparticle being much smaller than the excitation wavelength. Even though the assumption doesn't correspond to the simulation condition used in this research, it helps a simpler form to represent the electric dipole resonance in eq. 2.1.48 and 2.1.49, and more ideal form for the mathematical description of representing a nanoparticle as an ideal dipole to articulate eq. 2.2.3 and eq. 2.2.4.

doi:10.6342/NTU202501130

Additionally, the key physics among these two sections includes:

First, according to eq. 2.1.42 and eq. 2.1.43 with the simplification of Riccati-Bessel functions, a_1 corresponds to electric dipole resonance, while $b_1 = 0$ indicates the absence of magnetic dipole resonance in localized surface polariton resonance.

Secondly, a polariton in the DUV region is excited at the interface with a negative sign on the permittivity of two materials, such as c-Si-air interface or c-Si-silica interface in the DUV region.

Third, the fundamental physical properties of crystalline silicon in the DUV region exhibit polaritonic resonance.

2.3 Photothermal nanophotonic nonlinear scattering

Nonlinear optical research involving various materials holds great promise for bridging nanophotonics with modern techniques for nanoscale semiconductor observation and the development of all-optical switches for integrated circuits. A significant breakthrough in this field was the discovery of plasmonic saturated excitation (p-SAX) microscopy, which emerged from the study of saturated excitation in gold nanoparticles. This technique modulates the excitation intensity temporally and demodulates the scattering intensity at harmonic frequencies, enabling label-free imaging of gold nanospheres. p-SAX has demonstrated enhanced spatial resolution, achieving λ/8 of the excitation wavelength, and

doi:10.6342/NTU202501130

has also improved imaging depth.

A historical review of the enhanced photothermal nonlinear scattering by our lab starts with discussing surface plasmon resonance (SPR) in the visible wavelength. The plasmonic field enhancement in metallic nanostructures can lead to a largely enhanced nonlinear refractive index as high as $n_2 \sim 1\ \mu m^2/mW$, which is three orders of magnitude higher than that of the bulk material. This effect is understood through the quasi-static approximation of the classical Mie theory, where the origin of photothermal optical nonlinearity is partially attributed to temperature-dependent permittivity, as described by (eq. 2.3.1),

$$\sigma_{sca}(T) = \frac{8}{3}\pi\kappa^4 r^6 \left|\frac{\varepsilon_p(T) - \varepsilon_m}{\varepsilon_p(T) + 2\varepsilon_m}\right| \quad \text{(eq. 2.3.1)}$$

, where $\sigma_{sca}(T)$ is the scattering cross-section, r is the radius of the nanoparticle, ε_p is the complex relative permittivity for a nanoparticle, and ε_m is the relative permittivity from the surrounding lossless medium, T is the temperature for the nanoparticle, influenced by both electrons and phonon temperatures. Under CW illumination, the temperature difference between electron and phonon is small, and assuming that the thermal conductivity of the background medium is much lower than that of the nanoparticle, so the temperature increment of the nanoparticle is much larger compared to that of the background with a constant permittivity. When the denominator is zero, i.e.

doi:10.6342/NTU202501130

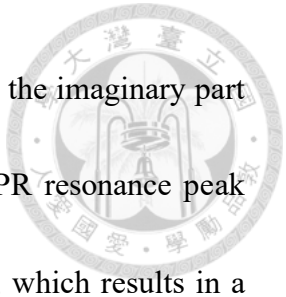

Re($\varepsilon_p + 2\varepsilon_m$)=0, resonance appears with the denominator remaining the imaginary part ε_p. With increasing excitation intensity of the incident light, the SPR resonance peak broadens due to the reduction of σ_{sca} through photothermal effects, which results in a slowdown in the increase of scattering intensity. In Figure 2.3, the real and imaginary parts of the permittivity are shown in (a) under 564 nm laser illumination. In Figure 2.3(a), the blue dots represent the permittivity calculated using the linear temperature model, while the black line corresponds to the analytical solution of the coupled heat and Maxwell equations. Figure 2.3(b) illustrates the relationship between the excitation and scattering intensity of a gold nanoparticle with a diameter of 80 nm under continuous-wave (CW) laser illumination at 561 nm. The analytical solutions, obtained using the quasi-static approximation, and the Mie theory are represented by the green and black lines, respectively, and are solved using the coupled equations with the absorption cross-section. The red dots in (b) correspond to the experimental results in (b).

It was not until 2020 that research on silicon nanoparticles revealed their giant optical nonlinearity, attributed to Mie resonance-enhanced light-matter interactions. This discovery opened new possibilities for GHz all-optical control at the nanoscale and super-resolution imaging of silicon, achieving more than a two-fold enhancement in spatial resolution in the visible region. Building upon this pioneering work, our present study aims to explore the deep ultraviolet (DUV) region, further expanding the potential

doi:10.6342/NTU202501130

applications of nonlinear optical microscopy.

Unlike metals, the polaritonic resonances of silicon in the DUV region originate from strong interband transitions between the valence and conduction bands, leading to a sharp permittivity peak in the deep ultraviolet (DUV) region. Similar to how Mie resonance explains photothermal nonlinearity in the visible region, the polaritonic resonance of silicon may satisfy eq. 2.3.1, thereby enabling the explanation of photothermal nonlinearity in the DUV region.

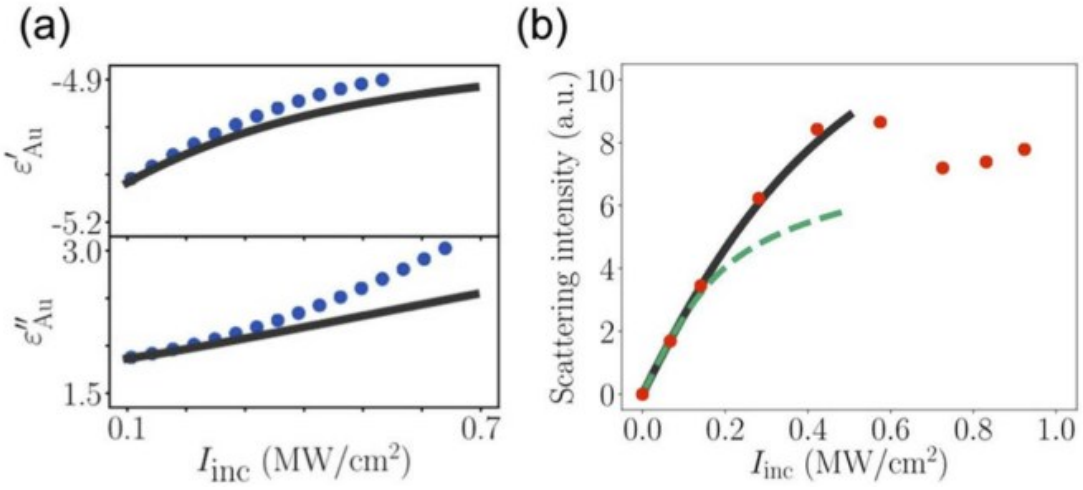

Figure 2.3: Photo-thermo-optical nonlinearity analyzed analytically and numerically. (a) Real and imaginary parts of the permittivity of gold nanoparticles of diameter (D) 100 nm under CW laser excitation at wavelength 564 nm. The blue dots are permittivity calculated by the linear temperature model. Solid black lines indicate the analytical solution combining the coupled heat and Maxwell equations. (b) Excitation intensity at 560 nm CW laser and the corresponding scattering intensity of a single gold nanoparticle of D=80 nm. The green dashed line and black solid line are numerical solutions by solving the

doi:10.6342/NTU202501130

coupled equations with the absorption cross-section calculated by quasi-static approximation and Mie theory, respectively. Red dots come from experimental results. (a) and (b) are reproduced from [30].

In our previous discussions in the visible region, detailed analyses of the photothermal nonlinearity of the effective nonlinear index (n_2) were conducted. For bulk silicon, n_2 approaches $10^{-6}\mu m^2/mW$, which is three orders of magnitude larger than Kerr-type nonlinearity, where n_2 is approximately $10^{-9}\mu m^2/mW$. The heating mechanism in silicon, known as the thermo-optical effect, is explained by two self-induced optical heating processes[22]. First, the photothermal effect arises from material absorption, which depends on the absorption cross-section of incident light and leads to a temperature increase. The absorption cross-section is determined theoretically using Mie resonance and measured experimentally via spatial modulation spectroscopy. This temperature increase, in turn, triggers the thermo-optical effect, where the absorption cross-section changes as a feedback response to temperature variations. These two processes alternate until thermal equilibrium is reached. The relation of the temperature and the refractive index is

$$n = n_0 + \frac{dn}{dT}\Delta T. \qquad \text{(eq. 2.3.2)}$$

In this equation, $\frac{dn}{dT}$ it has the same meaning as the temperature coefficient and ΔT is the temperature increment based on light-heating materials. The equilibrium temperature is

doi:10.6342/NTU202501130

calculated by Fourier's heat equation[51],

$$\rho C_p \frac{\partial T}{\partial t} - \kappa \nabla^2(T) = \alpha I, \quad \text{(eq. 2.3.3)}$$

where C_p is the heat capacity of the nanoparticle, ρ is the density, κ is the thermal conductivity, α is the absorption coefficient, and I is the intensity of the light source. In the equilibrium state, the first term in the heat equation can be eliminated, so we are left with

$$-\kappa \nabla^2(\Delta T) = \alpha I. \quad \text{(eq. 2.3.4)}$$

Integrating over the region of radius r, we therefore derived,

$$\Delta T = \frac{\alpha I r^2}{\kappa}, \quad \text{(eq. 2.3.5)}$$

Replacing this with the refractive index, we have

$$n = n_0 + \frac{dn}{dT}\frac{\alpha r^2}{\kappa} I. \quad \text{(eq. 2.3.6)}$$

Hence, we derive the nonlinear refractive index for the photo-thermo-optical effect in the following representation,

$$n_2 = \frac{dn}{dT}\frac{\alpha r^2}{\kappa}. \quad \text{(eq. 2.3.7)}$$

In summary, the nonlinear refractive index (n_2) is influenced by Mie-resonance-enhanced giant photothermal nonlinearity, which depends on $\frac{dn}{dT}$. Therefore, we analyzed the gradient of the refractive index in the visible wavelength range, as shown in Figure 2.4 (c) and (d).

Furthermore, since our goal was to tune the wavelength to the deep ultraviolet

doi:10.6342/NTU202501130

(DUV) region to explore the distribution of nonlinearity and its role in enhancing spatial resolution, we did not limit our discussion to the refractive index at 561 nm. Instead, we also examined the refractive index at 266 nm, as demonstrated in Figure 2.4 (a) and (b). In Figure 2.4 (c), the refractive index (n) in the visible region varies by 3%, ranging from 3.98 to 4.1, while the extinction coefficient (k) varies by 2.2%, ranging from 0.023 to 0.0737. In the deep ultraviolet (DUV) region, as shown in Figure 2.4 (a), n exhibits a 15% variation, ranging from 2.2 to 2.53. Similarly, k decreases by 3.85%, from 4.368 to 4.2, as the temperature increases from 300K to 700K. Here, n denotes the extent of light bending, while k characterizes the material's absorption properties.

Moreover, the permittivity data shown in Figure 2.4 (b) and (d) provide valuable insight into the optical properties of silicon from permittivity. If the real part of the permittivity is greater than 0 with positive permeability, the material is classified as a dielectric material[52]. Conversely, if the real part is less than 0, the material cannot support propagating light waves, and reflection or plasmonic effects dominate. Thus, the discussions in panels (b) and (d) are relevant for understanding these properties.

In Figure 2.4 (b), for the discussion of the material in the DUV region, the real part of the permittivity ranges from -14.2 to -11.3 as the temperature increases from 300K to 700K, showing a 20.4% variation. The imaginary part varies from 19.3 to 21.3, with a 10.36% variation. In the visible region, the real part of the permittivity ranges from 15.84

doi:10.6342/NTU202501130

to 16.744, exhibiting a 6.9% variation, while the imaginary part increases from 0.07 to 0.16878 with a 141% increment. To the first order of approximation, the variation in the real part in the DUV region is four times greater than that in the visible range, suggesting that the photothermal nonlinearity at 266 nm might be more significant than that at 561 nm.

However, determining the modulation depth solely from variations in the refractive index or permittivity is challenging, as the resonance induced in the nanoparticle depends on both its size and shape. Therefore, numerical simulations are essential for analyzing light-matter interactions, making them a crucial component of the study in Chapter 4.

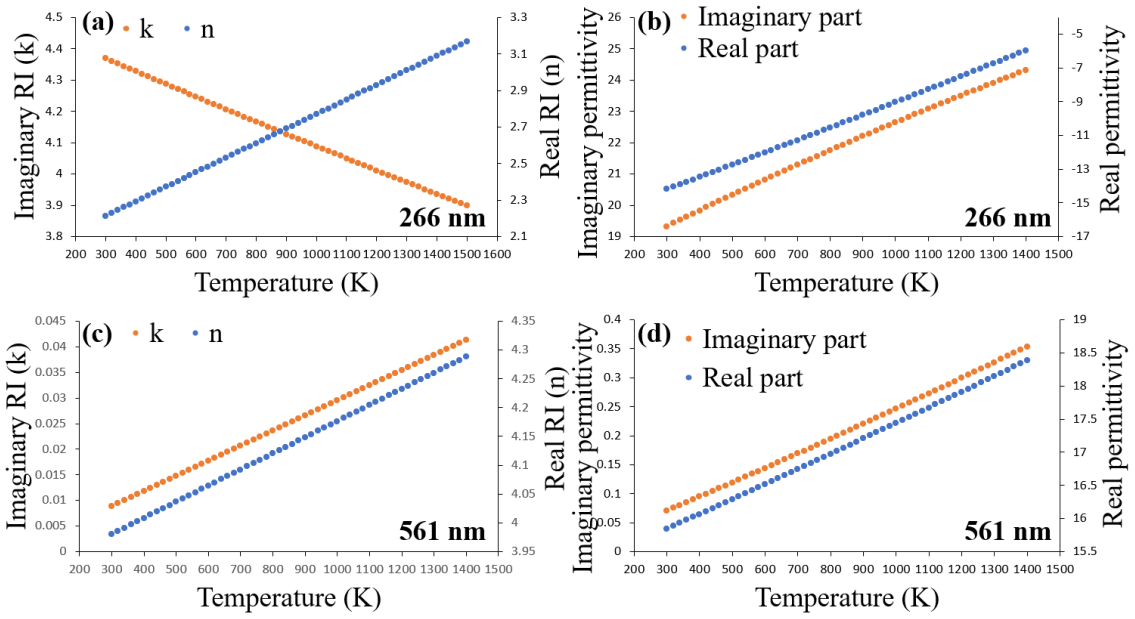

Figure 2.4: Refractive index and permittivity at 266 nm and 561 nm wavelengths as a function of temperatures ranging from 300K to 1400K. (a) The real and the imaginary parts of the refractive index (*n*

doi:10.6342/NTU202501130

and *k*) are plotted at 266 nm. (b) The real and imaginary permittivity are shown at 266 nm. (c) The real and imaginary refractive index at 561 nm. (d) The real and imaginary permittivity at 561 nm. The refractive index values are reproduced from [7].

Table 1 contains the information on the real part or the imaginary part of the refractive index as a function of temperatures, $n(T)$ and $k(T)$, and the permittivity, $\varepsilon_R(T)$ and $\varepsilon_I(T)$, and the absorption cross-sections as a function of temperatures, $C_{abs}(T)$ between 300K to 1400K.

First of all, for the SiNB with a temperature transition from 300K to 700K at 561 nm wavelength, n varies from 3.98 to 4.092, and k varies from 0.000884 to 0.0206. For the DUV region at 266 nm wavelength, n varies from 2.212 to 2.5305, and k varies from 4.368 to 4.206. Transitions from the visible to the DUV region, the imaginary part, k, becomes larger than n, indicating a negative permittivity in the real part. This causes the silicon nanostructure to become a polaritonic material in the DUV region. The representation of the real part or the imaginary part of the permittivity is also listed nearby n and k value.

A debate arises over whether the strong absorption of silicon in the DUV region leads to proportionally strong absorbed energy, based on its dependence on the imaginary part of the permittivity and the squared magnitude of the exciting electric field along the direction of the absorption dipole moment, as described in a paper published in 2025[61]. It

doi:10.6342/NTU202501130

is expected that a 35 nm-radius SiND in the DUV region—despite having half the volume of a 100 nm-width SiNB in the visible region—exhibits 200 times greater absorption, potentially resulting in 100 times more absorbed energy in the DUV region. Therefore, we plot Figure 2.5 to visualize the electric field distributions and Figure 2.6 to clarify how large the I_{ex} we need to heat up a nanoparticle to an average temperature 700K.

As a result, Figures 2.5 (a) and 2.6 (a) show that LSPR confines the electric field to the surface in the DUV region, enabling a r=35 nm SiND to reach 700K with an I_{ex} of 22 $mW/\mu m^2$. In the visible region, heating a w=100 nm SiNB to 700K requires an I_{ex} of 8.5 $mW/\mu m^2$, as shown in Figures 2.5 (b) and 2.6 (b). Figures 2.5 (c) and 2.6 (c) indicate that a w=170 nm SiNB requires 6.8 $mW/\mu m^2$, while Figures 2.5 (d) and 2.6 (d) show that a w=190 nm SiNB requires 5.3 $mW/\mu m^2$ to reach the same temperature.

In conclusion, although a SiND with a radius of 35 nm in the DUV region (266 nm) exhibits higher absorption, its limited electric field intensity results in greater absorbed energy in SiNBs with varying widths in the visible region (561 nm). This leads to smaller absorption cross-sections (C_{abs}) as a function of temperature for the SiND in the DUV region, compared to those of the three types of SiNBs in the visible region, as listed in Table 1.

doi:10.6342/NTU202501130

Wavelength (nm)	n(T)	k(T)	ε_R(T)	ε_I(T)	C_{abs}(T)	
561 nm Silicon Nanoblock	300K→700K	300K→700K	300K→700K	300K→700K	w=100 nm	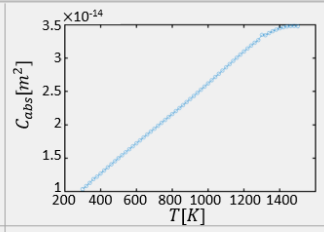
	3.98 ↓ 4.092	0.000884 ↓ 0.0206	15.84 ↓ 16.744	0.0703 ↓ 0.16878	w=170 nm	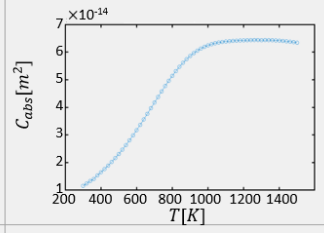
					w=190 nm	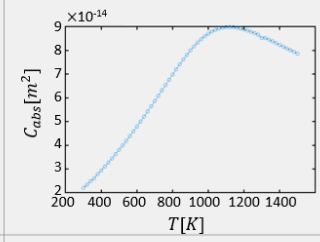
266 nm Silicon Nanodisk	300K→700K	300K→700K	300K→700K	300K→700K	r=35 nm	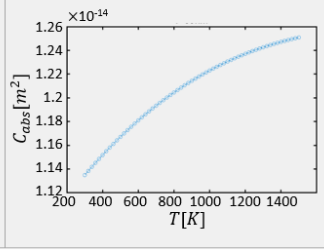
	2.212 ↓ 2.5305	4.368 ↓ 4.206	-14.19 ↓ -11.2865	19.328 ↓ 21.2863		

Table 1: A chart for comparing parameters used in the DUV (266 nm) and the visible region (561 nm) contains the information on the real part or the imaginary part of the refractive index, n(T) and k(T), and the permittivity, $\varepsilon_R(T)$ and $\varepsilon_I(T)$, and the absorption cross-sections (C_{abs}) as a function of temperatures between 300K to 1400K.

doi:10.6342/NTU202501130

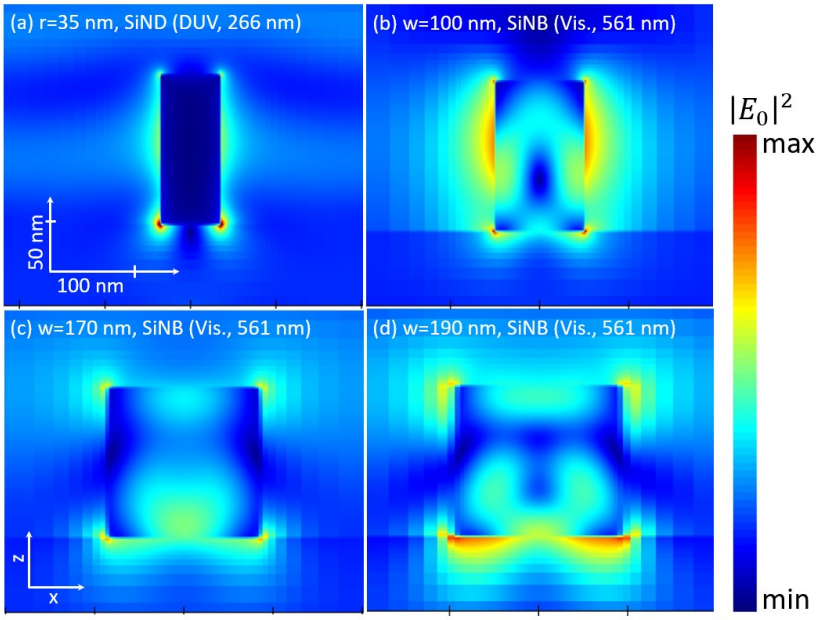

Figure 2.5: Electric field profiles along the xz-plane are shown in the DUV region at 266 nm for (a) a SiND with radius *r*=35 nm, and in the visible region at 561 nm for (b) a SiNB with width *w*=100 nm, (c) *w*=170 nm, and (d) *w*=190 nm. The incident plane wave is x-polarized and propagates along the -z direction.

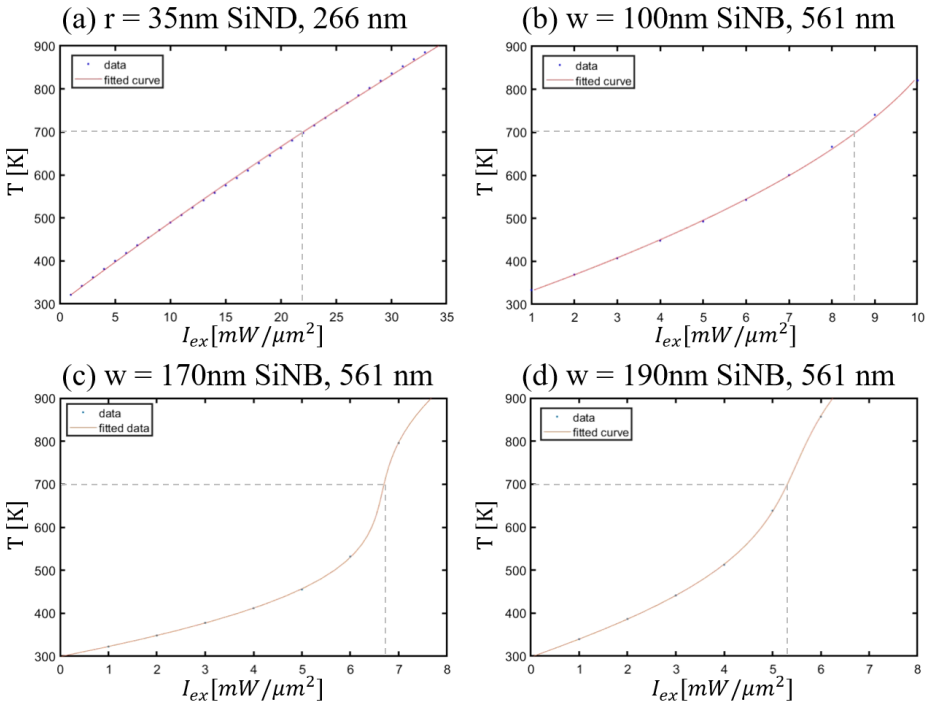

Figure 2.6: The excitation intensities (I_{ex}) required to heat a nanoparticle to an average temperature (T) of

doi:10.6342/NTU202501130

700 K are shown in the figure. For (a), a r=35 nm SiND at the DUV region (266 nm) requires an I_{ex} of 22 $mW/\mu m^2$ to heat it up to 700K. The required I_{ex} to heat a SiNB in the visible region (561 nm) to 700 K is 8.5 $mW/\mu m^2$ for w=100 nm in (b), 6.8 $mW/\mu m^2$ for w=170 nm in (c), and 5.2 $mW/\mu m^2$ for w=190 nm in (d).

2.4 Differential-excitation saturated excitation (dSAX) microscopy

The distinguishable distances between two point spread functions (PSF) define the resolution of optical microscopy. If we could get the image of signals with smaller PSFs, we could resolve a smaller distance between two PSFs, hence increasing the resolution. If the resolution surpasses the optical resolution limit, super-resolution is achieved. In this section, we'll demonstrate two kinds of SAX super-resolution optical microscopy, one is conventional SAX and the other is differential-excitation SAX (dSAX) microscopy for achieving super-resolution imaging[28].

In conventional SAX microscopy[19], the extraction of nonlinear fluorescence signals is achieved by harmonic demodulation techniques to achieve super-resolution with different harmonics. A higher order of harmonics signal contributes to a smaller PSF. The strategy of conventional SAX microscopy is shown in Figure 2.5, saturated scattering (SS) of a fluorescence signal is excited under stronger incident laser illumination. Fourier transform of the SS contributes to a frequency spectrum of several harmonics. If the light

doi:10.6342/NTU202501130

incident is not strong enough to excite a nonlinear response, only linear scattering is shown. The corresponding Fourier transform shows a single frequency identical to that of the incident light.

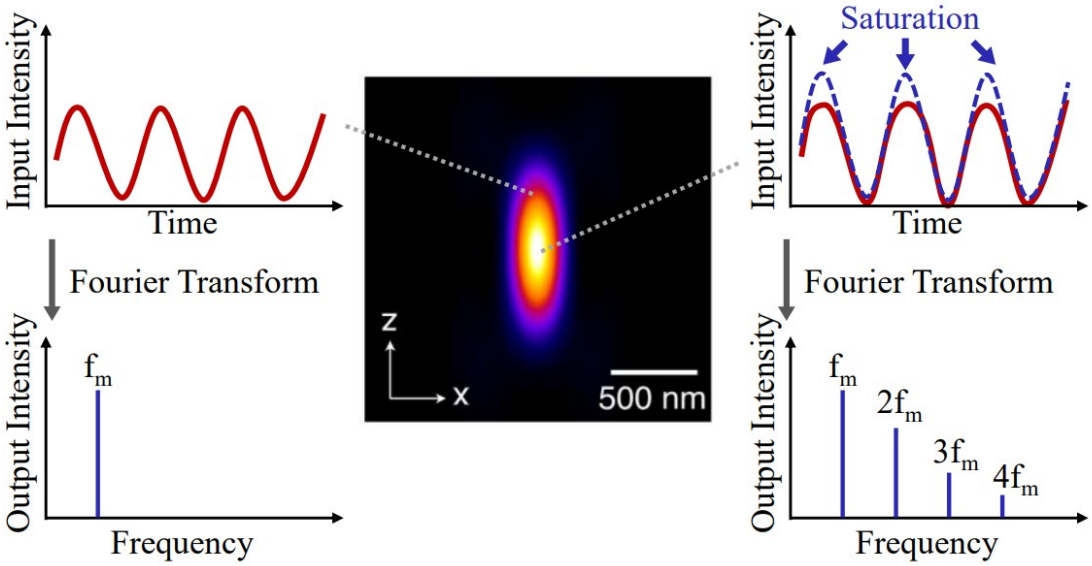

Figure 2.7: The concept of SAX microscopy. The center image represents the PSF of the focal point. Near the center part of the PSF, light intensity is the strongest, causing a nonlinear response for showing saturated scattering (SS). Fourier transform of the SS shows higher-order harmonics in the frequency spectrum. On the edge of the Gaussian beam, light intensity is weaker, so only linear scattering is excited. Fourier spectrum shows an identical frequency to the incident frequency. The figure was reproduced from [29].

Unlike conventional SAX using harmonic demodulation techniques, dSAX proposed by Hampolickova et al, extracted saturated fluorescence signals varying with different excitation intensities and compared different degrees of excitation saturation to

doi:10.6342/NTU202501130

improve the SNR. The scheme of dSAX is shown in Figure 2.6. The Linear signal minus the nonlinear signal leads to the subtraction signal. This subtraction signal shows resolution enhancement compared to the linear signals. The subtraction signal is obtained according to eq. 2.5.1,

$$I_{FL}(I_{ex}) = a_1 I_{ex} + a_2 {I_{ex}}^2 + a_3 {I_{ex}}^3 + \ldots = I_L(I_{ex}) - I_{NL}(I_{ex}) \qquad \text{(eq. 2.5.1)}$$

$I_{FL}(I_{ex})$ is the scattering intensity of fluorescent molecules, and it can be expanded to orders of excitation intensities ($a_1 I_{ex} + a_2 {I_{ex}}^2 + a_3 {I_{ex}}^3 + \ldots$). $I_L(I_{ex})$ is the linear signal and $I_{NL}(I_{ex})$ is the difference between the linear and subtraction fluorescent signal, $I_{FL}(I_{ex})$. $I_L(I_{ex})$ minus $I_{NL}(I_{ex})$ results to the nonlinear intensity with enhanced SNR ratio, as shown in Figure 2.6.

Combining dSAX and conventional SAX means tuning the excitation intensity by conventional SAX microscopy to enhance resolution. By improving the SNR with better beam quality and comparing SAX of different signal qualities, the spatial resolution is improved. In this thesis, even though we don't have the experimental result showing saturation scattering with different harmonics, we used simulational scattering nonlinearity with the concept of dSAX to achieve a narrower PSF.

doi:10.6342/NTU202501130

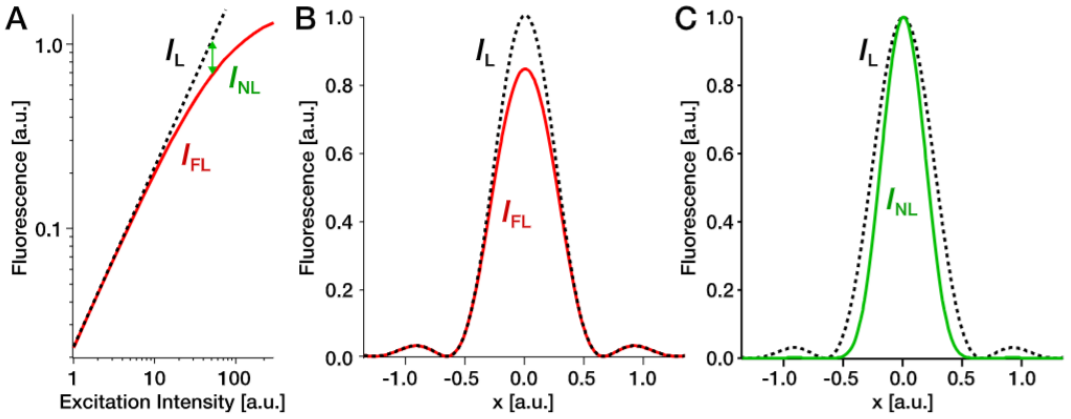

Figure 2.8: Concept of differential-excitation SAX (dSAX) proposed by Hampolickova et al. A narrower PSF is achieved by subtracting the nonlinear fluorescence signal from linear scattering intensity. (a) Relations between saturated fluorescent signal (I_{FL}), linear intensity (I_L), and nonlinear intensity (I_{NL}). (b) Relation between I_L and I_{FL}. (c) I_{NL} from subtracting I_{FL} from I_L shows a narrower PSF compared to I_L. Figures were reproduced from [28].

2.5 Finite-difference time-domain and finite element method

Faraday and Ampere's discoveries are the essence for Maxwell to unify the form of electromagnetic waves (EMW). There is no doubt that Maxwell's unification reached a milestone in classical electrodynamics; the missing term of the displacement current, which requires a physical basis, articulates the physics map of EMW. Maxwell's equations remain the development basis of electro-technology since the nineteenth century[53]. Many EMW interaction problems solved are related to the arbitrary shapes of particles illuminated by scattered fields. Therefore, an efficient way to calculate the

doi:10.6342/NTU202501130

scattered field based on total-field or scattered-field (TFSF) incident light source equipped in most commercial finite-difference time-domain (FDTD) solvers prevail due to its high efficiency.

The basis of FDTD lies in Maxwell's equation. If we consider Maxwell's equations in Cartesian coordinates, they are described in the following form in a single medium, which is linear, isotropic, and homogeneous in vacuum and no electromagnetic source,

$$\frac{\partial H_x}{\partial t} = \frac{1}{\mu}\left[\frac{\partial E_y}{\partial z} - \frac{\partial E_y}{\partial y} - (M_{source_x} + \sigma^* H_x)\right] \quad \text{(eq. 2.6.1)}$$

$$\frac{\partial H_y}{\partial t} = \frac{1}{\mu}\left[\frac{\partial E_z}{\partial x} - \frac{\partial E_x}{\partial z} - (M_{source_y} + \sigma^* H_y)\right] \quad \text{(eq. 2.6.2)}$$

$$\frac{\partial H_z}{\partial t} = \frac{1}{\mu}\left[\frac{\partial E_x}{\partial y} - \frac{\partial E_y}{\partial x} - (M_{source_z} + \sigma^* H_z)\right] \quad \text{(eq. 2.6.3)}$$

$$\frac{\partial E_x}{\partial t} = \frac{1}{\varepsilon}\left[\frac{\partial H_z}{\partial y} - \frac{\partial H_y}{\partial z} - (J_{source_x} + \sigma E_x)\right] \quad \text{(eq. 2.6.4)}$$

$$\frac{\partial E_y}{\partial t} = \frac{1}{\varepsilon}\left[\frac{\partial H_x}{\partial z} - \frac{\partial H_z}{\partial x} - (J_{source_y} + \sigma E_y)\right] \quad \text{(eq. 2.6.5)}$$

$$\frac{\partial E_z}{\partial t} = \frac{1}{\varepsilon}\left[\frac{\partial H_y}{\partial x} - \frac{\partial H_x}{\partial y} - (J_{source_z} + \sigma E_z)\right] \quad \text{(eq. 2.6.6)}$$

, where σ: $electric\ conductivity\ (S/m)$ and σ^*: $equivalent\ magnetic\ loss\ (\Omega/m)$.

The numerical method used in FDTD is the central difference method (中央差分法), used to simplify terms in solving partial differential equations in the following Taylor expansions:

doi:10.6342/NTU202501130

$$f(x \pm \Delta x) = f(x) \pm \frac{f\prime(x)}{1!}(\Delta x) + \frac{f"(x)}{2!}(\Delta x)^2 + O(\Delta x)^3. \quad \text{(eq. 2.6.7)}$$

Afterwards, we rearranged terms to obtain appropriate differential equations:

$$f'(x) = \frac{f(x+\Delta x)-f(x)}{\Delta x} - \frac{\Delta x}{2!}f"(x) + O(\Delta x)^2 \text{ or}$$

$$f'(x) = \frac{f(x)-f(x-\Delta x)}{\Delta x} - \frac{\Delta x}{2!}f"(x) + O(\Delta x)^2. \quad \text{(eq. 2.6.8)}$$

Tidy up the differential equation and neglect higher order terms, we obtained the central differential equations as the following representation,

$$f'(x) \simeq \frac{f(x+\Delta x)-f(x-\Delta x)}{2\Delta x}. \quad \text{(eq. 2.6.9)}$$

In discretizing Maxwell's equations, FDTD applied the Yee algorithm for doing so[54]. Kane Yee first proposed the basic algorithm of FDTD in 1966. Later on, Allen Taflove and M.E. Brodwin obtained the numerical stability for Yee's algorithm, who first solved the sinusoidal steady-state EM scattering problems in two- and three-dimensional. This solution becomes an example in a lot of textbooks regarding classical computer programs. We'll discuss FDTD in detail with a precise mathematical form for clarity after a rough understanding of some basic properties of FDTD and its comparison to another commonly used finite element method (FEM).

In discretizing Maxwell's equations based on the Yee algorithm, space and time are meshed. We can rename every point in space and time respectively as (i, j, k) and $n\Delta t$, among which Δt is the time interval and n is the integer multiple of the time interval. Therefore, we can represent a function of space and time as,

doi:10.6342/NTU202501130

$$f(i,j,k,n\Delta t) = f^{n}_{i,j,k} \qquad \text{(eq. 2.6.10)}$$

with the concept of the central difference method, we discretized and tidied up the following equations:

$$E_x\big|^{n+1/2}_{i,j+1/2} = \left(\frac{1-\frac{\sigma_{i,j+1/2}\Delta t}{2\varepsilon_{i,j+1/2}}}{1+\frac{\sigma_{i,j+1/2}\Delta t}{2\varepsilon_{i,j+1/2}}}\right)E_x\big|^{n-1/2}_{i,j+1/2} + \frac{\frac{\Delta t}{\varepsilon_{i,j+1/2}}}{1+\frac{\sigma_{i,j+1/2}\Delta t}{2\varepsilon_{i,j+1/2}}}\left[\frac{H_z\big|^{n}_{i,j+1}-H_z\big|^{n}_{i,j}}{\Delta y} - J_{source_x}\big|^{n}_{i,j+1/2}\right],$$

(eq. 2.6.11)

$$E_y\big|^{n+1/2}_{i-1/2,j+1} = \left(\frac{1-\frac{\sigma_{i-1/2,j+1}\Delta t}{2\varepsilon_{i,j+1/2}}}{1+\frac{\sigma_{i-1/2,j+1}\Delta t}{2\varepsilon_{i-1/2,j+1}}}\right)E_y\big|^{n-1/2}_{i-1/2,j+1} + \frac{\frac{\Delta t}{\varepsilon_{i-1/2,j+1}}}{1+\frac{\sigma_{i-1/2,j+1}\Delta t}{2\varepsilon_{i-1/2,j+1}}}\left[-\frac{H_z\big|^{n}_{i,j+1}-H_z\big|^{n}_{i-1,j+1}}{\Delta x} - J_{source_x}\big|^{n}_{i-1/2,j}\right], \qquad \text{(eq. 2.6.12)}$$

$$H_z\big|^{n+1}_{i,j+1} = \left(\frac{1-\frac{\sigma^{*}_{i,j+1}\Delta t}{2\mu_{i,j+1}}}{1+\frac{\sigma^{*}_{i,j+1}\Delta t}{2\mu_{i,j+1}}}\right)H_z\big|^{n}_{i,j+1} + \frac{\frac{\Delta t}{\mu_{i,j+1}}}{1+\frac{\sigma^{*}_{i,j+1}\Delta t}{2\mu_{i,j+1}}}\left[\frac{E_x\big|^{n+1/2}_{i,j+3/2}-E_x\big|^{n+1/2}_{i,j+1/2}}{\Delta y} - \frac{E_y\big|^{n+1/2}_{i+1/2,j+1}-E_y\big|^{n+1/2}_{i-1/2,j+1}}{\Delta y} - M_{source_x}\right]. \qquad \text{(eq. 2.6.13)}$$

The interval of time and space differs by 0.5Δ, as shown in Figure 2.7. From these discretized equations, we can generate every next step electric field from its former electric and magnetic field according to Yee grid mesh as shown in Figure 2.8.

Courant–Friedrichs–Lewy (CFL) stability criterion describes that information traveling distance during every timestep length must be lower than the distance between meshes. Time and space must satisfy the rule for keeping stable during every calculation in iterations.

$c\Delta t \leq \frac{1}{\sqrt{(\frac{1}{\Delta x})^2+(\frac{1}{\Delta y})^2+(\frac{1}{\Delta z})^2}}$, among which c is the light speed in a vacuum, Δx, Δy, Δz

doi:10.6342/NTU202501130

represents the spatial resolution along the x-axis, y-axis, and z-axis, respectively. In a one-dimensional mesh settings, we have $\Delta t \leq \frac{\Delta x}{\sqrt{2}c}$. It has to be satisfied to approach stability in the simulation.

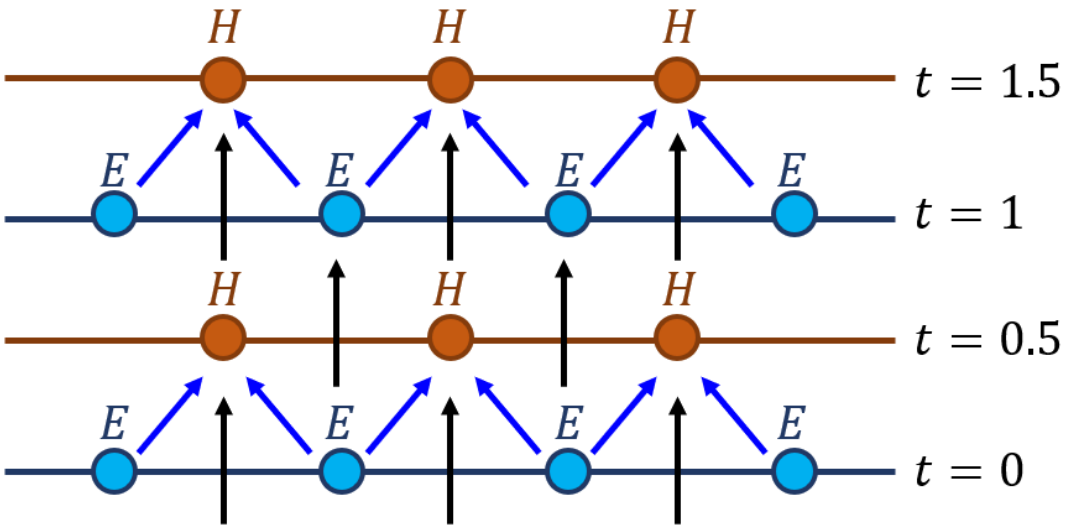

Figure 2.9: Flowchart of FDTD calculation in space and time. The basic idea of the Yee algorithm in 1 dimension. Brown color represents magnetic fields, blue color represents electric fields, and black arrows indicate the direction of incident light.

FDTD is mainly used to solve differential equations, such as Radio Frequency (RF) and microwave applications. Additionally, FDTD comparable to the finite element method (FEM) is fast because it does not need to solve matrix equations or simultaneous equations. Mesh constructions in FDTD are distributed according to Cartesian coordinates in space. Comparable to that of FEM, where mesh settings are stored in the matrix and its storage contains what components are built for, FDTD offers fast

doi:10.6342/NTU202501130

calculation and less storage. Additionally, FEM is more suitable to be considered with a low frequency of 50Hz comparable to FDTD. Nevertheless, precise mesh settings with FEM enable the simulation of various structures in detail.

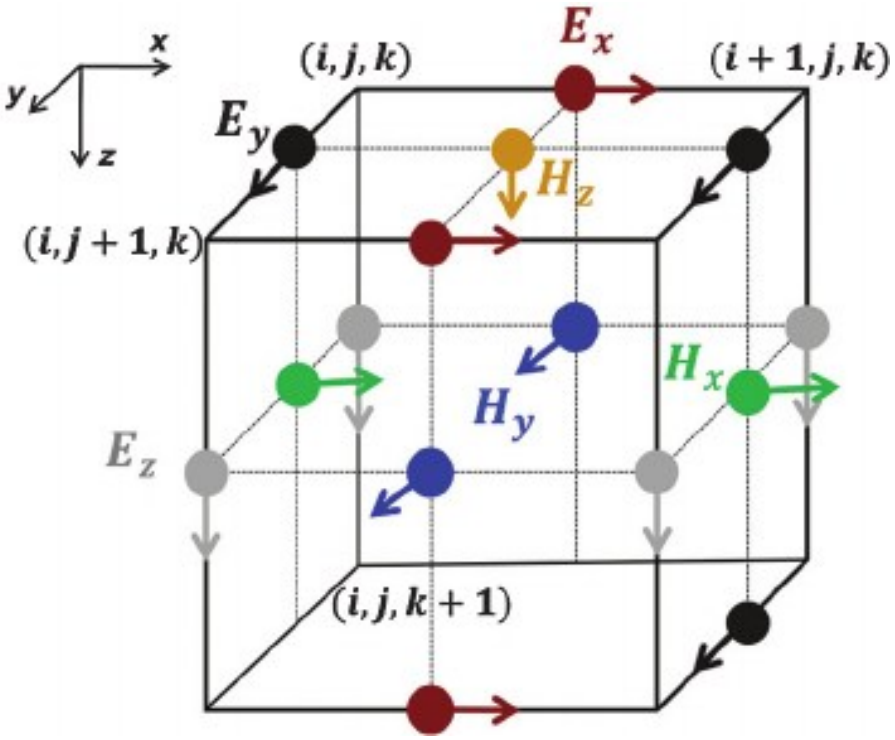

Figure 2.10: The electromagnetic field distribution in a Yee grid mesh[55]. Inside FDTD, the discretization of space and time is named with every mesh point (i,j,k,nΔt). Δt is a time interval, and n is an integer multiple of Δt. The figure was reproduced from [53].

TFSF technique is an efficient technique widely used in FDTD modeling to compute scattered fields with equivalence principle[54,55], by which the incident wave is separated into the total field and scattered field, as shown in Figure 2.9. Basic TFSF light source propagating in space can be formulated by electric field E and magnetic field H

doi:10.6342/NTU202501130

propagating in an isotropic non-dispersive medium of permittivity ε, permeability μ, electric conductivity σ, and magnetic loss σ^* ,

$$\varepsilon(x)\partial_t E(x,t) + \sigma(x)E(x,t) = \nabla \times H(x,t) - J_{inc}(x_{\partial\Omega}, t), \quad \text{(eq. 2.6.14a)}$$

$$\mu(x)\partial_t H(x,t) + \sigma^*(x)H(x,t) = -\nabla \times E(x,t) - M_{inc}(x_{\partial\Omega}, t), \quad \text{(eq. 2.6.14b)}$$

where the differential operator $\partial_t(\cdot)$ is a partial derivative concerning time t, and $x = [x, y, z] \in R^3$. $\partial\Omega$ indicates the magnetic light sources exist at the interface of the total-field region Ω_T and the scattered-field region Ω_S. The above functions are comprised of electric current density $J_{inc}(x_{\partial\Omega}, t)$ and magnetic current density $M_{inc}(x_{\partial\Omega}, t)$ as forcing functions to form a set of inhomogeneous partial differential equations. The incident wave here is generated by the electric and magnetic current sources, J_{source} and M_{source}, with which its interaction with the target forms a total EM field, E_T and H_T. Relations between incident, scattered, and total field are represented as $E_T = E_{inc} + E_S$ and $H_T = H_{inc} + H_S$. A more precise description is shown as $E(x,t) = E_S(x,t) + E_{inc}(x,t)$ and $H(x,t) = H_S(x,t) + H_{inc}(x,t)$ for $x \in \Omega_T$, belonging to the total-field region. The exterior fields, containing only scattered fields are $E(x,t) = E_S(x,t)$ and $H(x,t) = H_S(x,t)$ for $x \in \Omega_S$. In short, the discontinuity of the EM field, $J_{inc}(x_{\partial\Omega}, t)$ and $M_{inc}(x_{\partial\Omega}, t)$ lies on $x \in \partial\Omega$, where the subscripts S and inc denote the scattered and incident waves, respectively.

doi:10.6342/NTU202501130

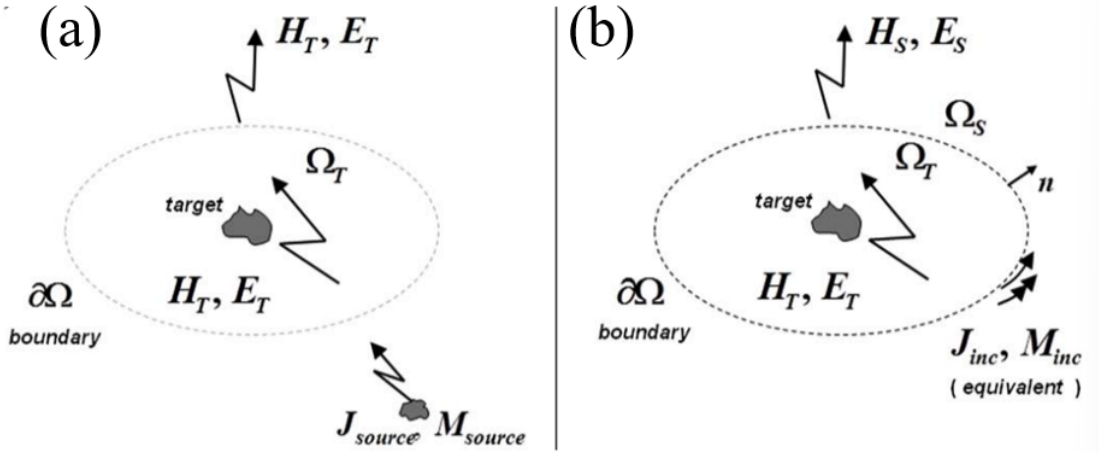

Figure 2.11: FDTD with field equivalence principle to separate incident field and scattered field. (a) is the original problem consisting of total fields filling all of the space. (b) demonstrates the equivalence principle applying to the problem, which divides the space into total-field and scattered-field regions. The figure was reproduced from [55].

doi:10.6342/NTU202501130

Chapter 3. Materials and Methods

In this chapter, we'll introduce sample fabrication in experiments and the settings of simulation files.

3.1 Simulation strategy

The goal of the simulation is to demonstrate photothermal nonlinear scattering in silicon nanostructures heated by laser-induced polaritonic resonance. First, we explain how the optimal radius of the structure is determined using an optimization function. Once the radius is established, we simulate temperature-dependent absorption cross-sections to derive the relationship between excitation intensity and temperature. To model photothermal nonlinearity, we employ three approaches: two setups in Lumerical and one in COMSOL.

In this study, we use the finite-difference time-domain method (FDTD) in Ansys-Lumerical (Lumerical, Inc., FDTD Solutions) combining finite element method (FEM) simulations in COMSOL Multiphysics (COMSOL, Inc.) to study the optical properties from a single silicon nanodisk. Lumerical FDTD simulation is used to calculate the scattering cross-section or absorption cross-section in a thermo-optical process based on the temperature-dependent silicon refractive index. The absorption cross-section is input

doi:10.6342/NTU202501130

to COMSOL for calculating heat flux based on the Fourier heat equation. This simulation method is identical to those demonstrated in the previous work[7].

3.1.1 Particle Swarm Optimization (PSO) method for size determination

First, we want to determine the radius of the silicon nanodisk used for simulating photothermal nonlinear scattering. Since the nonlinear scattering reported in our previous research relies on a temperature-dependent refractive index that causes spectrum shift under different temperatures, we used PSO for calculating the modulation depth, which is defined by the ratio of the scattering cross-section spectrum difference between 300K and 700K with the initial spectrum at 300K, i.e. $\frac{C_{sca,300K}-C_{sca,700K}}{C_{sca,300K}}$ at 266 nm wavelength. The concept of modulation depth here is the same concept shown as nonlinear deviation ratio (NDR)[7] or the modulation depth reported[56].

PSO is inspired by the immigration of animals in groups to profit from others' experiences, as the strategy shown in Figure 3.1. For example, if we have a random function containing several local minima, random points are scattered on the plane and search for minimum points in random directions after several iterations. The functions are shown below,

$$X^i(t+1) = X^i(t) + V^i(t+1), \qquad \text{(eq. 3.1.1.1)}$$

with $X^i(t) = (x^i(t), y^i(t))$ and velocity $V^i(t) = (v_x^i(t), v_y^i(t))$. The velocity is updated according to the rule, $V^i(t+1) = wV^i(t) + c_1 r_1(pbest^i - X^i(t)) +$

doi:10.6342/NTU202501130

$c_2 r_2(gbest - X^i(t))$, where r_1 and r_2 are random numbers between 0 and 1. w, c_1, c_2 are constant parameters.

$w(t)$ is called the inertia weight constant, set between 0 and 1 to represent the tendency for a particle to remain at the same velocity. w is set as a function to avoid velocity explosion[58], which can be set in a variety of ways. The initial value $V(0)$ is suggested to be infinitesimal or 0[57]. $pbest^i$ represents the best position of a single particle ever explored, and $gbest$ represents the best position ever found so far by the swarming group[59].

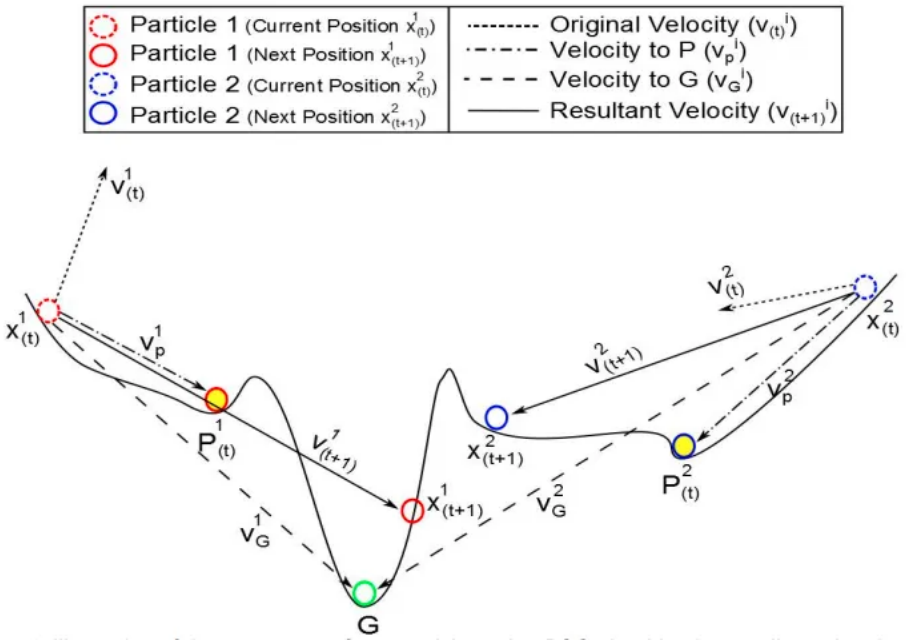

Figure 3.1: Particle swarm optimization (PSO) strategy, cited from[59]. The initial point starts from $x^1_{(t)}$ and the next step is determined by $V^1_p, P^1(t)$ and V^1_G, corresponding respectively to $V^i(t), pbest^i$, and $gbest$ in this thesis. The figure was reproduced from [58].

doi:10.6342/NTU202501130

Figures 3.2, 3.3, and 3.4 illustrate the radius optimization process, which is performed by calculating the largest modulation depth using particle swarm optimization (PSO). The optimization settings, shown in Figure 3.2, are used as input for PSO. The radius is varied between 20 nm and 55 nm, with each generation containing 10 particles and a maximum of 20 generations[60].

The optimized result, displayed in the right panel of Figure 3.3, indicates an optimal radius of 3.6e-08 m (*i.e.* 36 nm). The entire PSO process is visualized in Figure 3.4. The numerical aperture (NA) considered in this model is approximately 0.6.

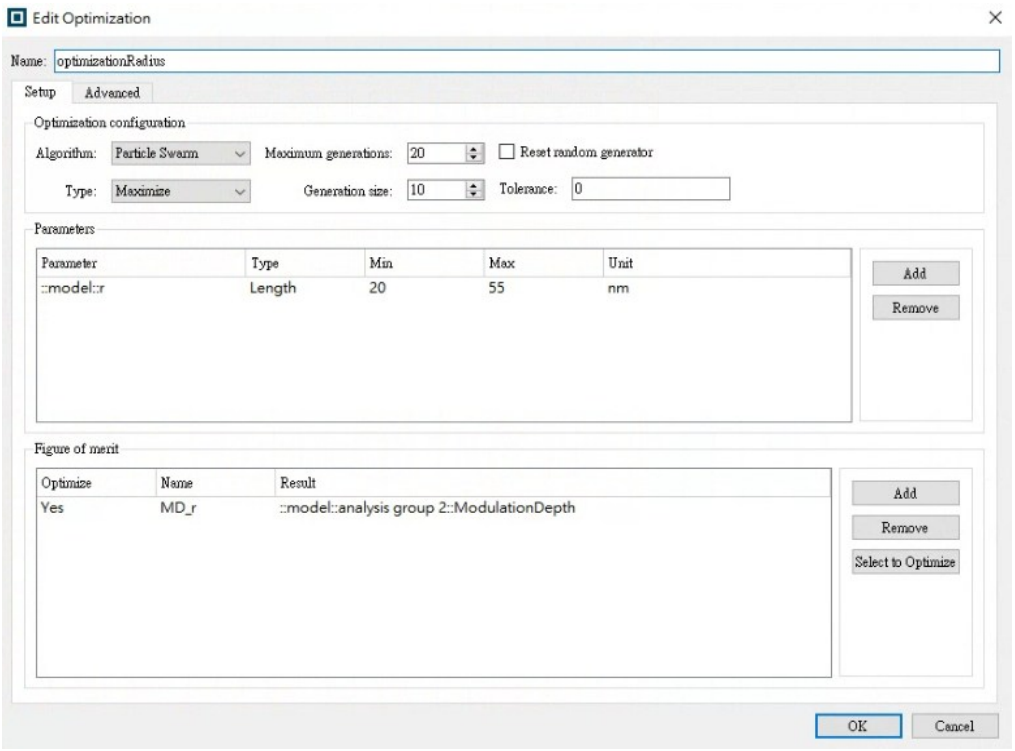

Figure 3.2: Settings in a particle swarm optimization (PSO). The maximum generations is set as number 20. In each generation, 10 random points will be counted, corresponding to the setting in Generation size. Ranges for finding optimized points are from a radius of 20 to 55 nm.

doi:10.6342/NTU202501130

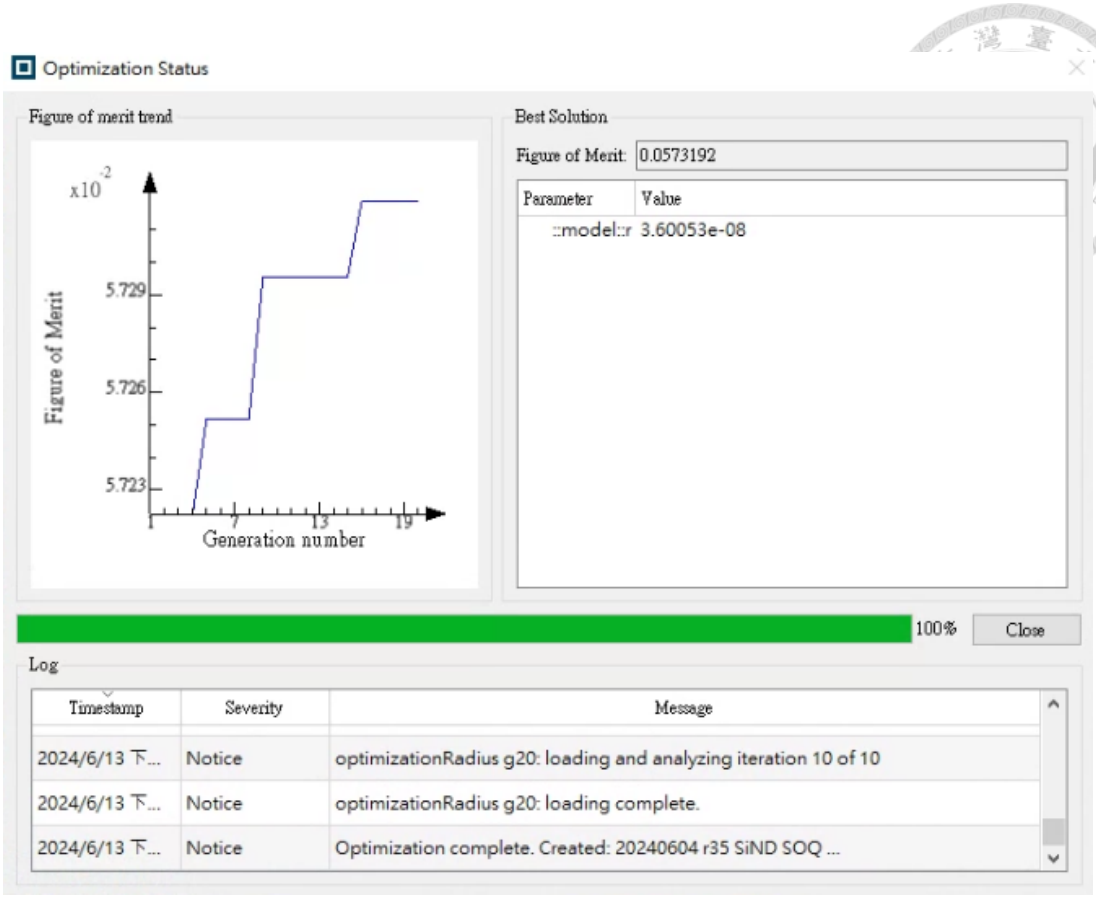

Figure 3.3: Trends of PSO. We can see that PSO keeps finding local minimums. While the blue line becomes flat (the y-axis remains the same value), it means that a local minimum is found. The best solution from PSO indicates an optimized radius of 3.6 e-08 m (*i.e.* 36 nm).

doi:10.6342/NTU202501130

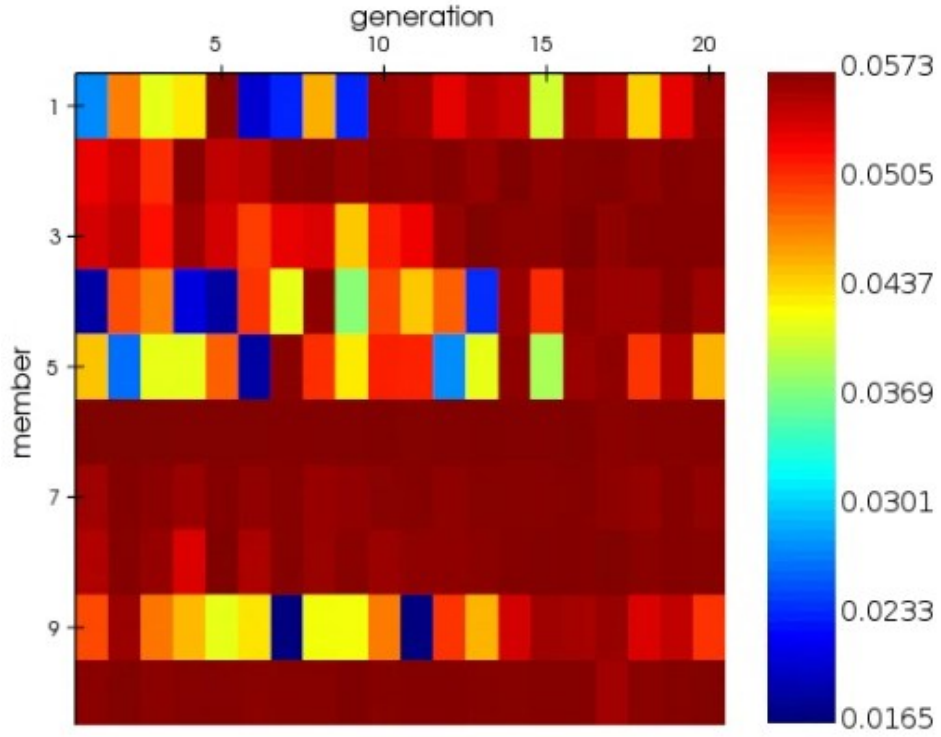

Figure 3.4: Generation of PSO in the form of color maps. The x-axis is the generation time. The y-axis means that there are 10 members, or 10 points selected, in a generation. The color bar indicates the modulation depth, defined as $\frac{C_{sca,300K}-C_{sca,700K}}{C_{sca,300K}}$. The resulting modulation depth is 0.0573, *i.e.* 5.7%.

3.1.2 Simulation Setup in Lumerical and COMSOL

In this section, three models are presented, each featuring a silicon nanodisk on a quartz substrate. Two of these models are simulation setups in Lumerical: one for PSO, as shown in Figure 3.5, and the other for calculating temperature-dependent absorption cross-sections from 300K to 1400K, as shown in Figure 3.6. The third simulation, shown in

doi:10.6342/NTU202501130

Figure 3.7, is a COMSOL setup used to map temperatures to their corresponding excitation intensities.

The simulation setups in Figure 3.5 and Figure 3.6 share the same settings for the total-field scattered-field (TFSF) light source. The only difference is that in Figure 3.5, two TFSF light sources are used to simultaneously extract scattering intensities at 300K and 700K for calculating the largest modulation depth. The settings for each nanodisk are identical to those of a single particle, as shown in Figure 3.6. In Figure 3.5, two silicon nanodisks at 300K and 700K are positioned at (x,y,z)=(-1000,0,0) and (1000,0,0), respectively.

The detailed Lumerical settings are shown in Figure 3.6. The FDTD simulation domain is defined as (x,y,z)=3200 nm×800 nm×1200 nm, centered at (0,0,0). Perfectly matched layer (PML) boundary conditions are applied in all directions. A plane wave light source is implemented using a total-field scattered-field (TFSF) source, spanning 480 nm×480 nm×500 nm and centered at (-1000 nm, 0, 0). The scattering cross-section monitor is positioned within a 600 nm×600 nm×600 nm region, also centered at (-1000 nm, 0, 0), while the absorption cross-section is measured within a 350 nm×350 nm×400 nm region at the same location. The TFSF light source and monitor settings follow the officially released tutorial[61]. To derive the modulation depth using PSO, I expanded the

doi:10.6342/NTU202501130

FDTD simulation domain to twice its original size to accommodate two TFSF light sources. This setup enables the extraction of scattering cross-sections at 300K and 700K, which are used to calculate the modulation depth.

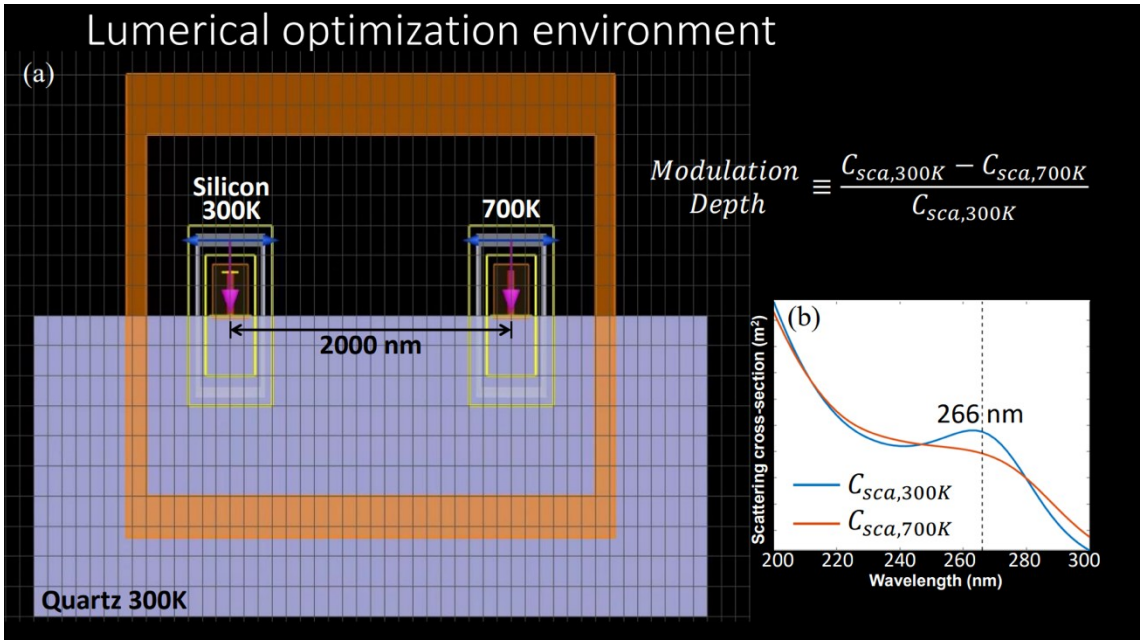

Figure 3.5: The Lumerical environment for calculating modulation depth based on PSO is shown. Two particles are separated from 2000 nm to minimize the polariton coupling. PSO for calculating the largest modulation depth is used to determine the radius of the silicon nanodisk for generating the largest nonlinear scattering. (a) shows the xz-view in Lumerical simulation containing two TFSF light source settings for silicon nanodisks of 300K and 700K refractive index. (b) show two spectra, one is the scattering cross-section calculated with 300K silicon refractive index, and the other is calculated from 700K refractive index. The modulation depth is defined by two spectra at 266 nm wavelength with the equation $\frac{C_{sca,300K}-C_{sca,700K}}{C_{sca,300K}}$.

doi:10.6342/NTU202501130

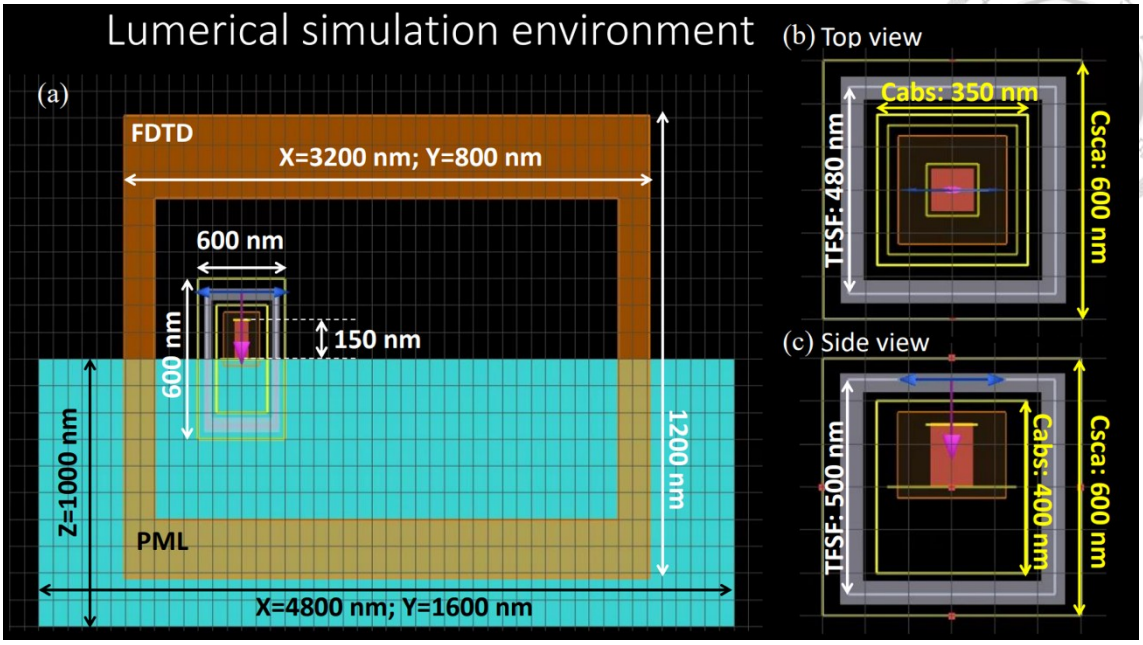

Figure 3.6: Simulation environment for a single silicon nanodisk. (a) is the x-z side view of the simulation settings in Lumerical. (b) is the x-y top view. (c) is the side view of the monitor settings. Monitor settings in TSFS light source contain monitor for scattering cross-section, absorption cross-section, and TFSF light source. Numerical aperture (NA) settings correspond to those shown in the reference paper[7].

COMSOL simulation is used to transfer temperature-dependent absorption cross-sections obtained from the Lumerical model shown in Figure 3.6 to the excitation intensity-dependency, shown in Figure 3.7. COMSOL is equipped with heat transfer in the solids module for calculating the temperature of the silicon nanodisk based on the absorption cross-sections obtained from Lumerical. Absorption cross-sections as a function of temperature calculated by Lumerical are input into COMSOL for deriving the corresponding temperature with different laser excitation intensities. The calculation

doi:10.6342/NTU202501130

domain is set as a cube of an identical edge length of 10000 nm. A single silicon nanodisk of determined radius is located at the center of the calculation domain. The ambient temperature is set as 300 K.

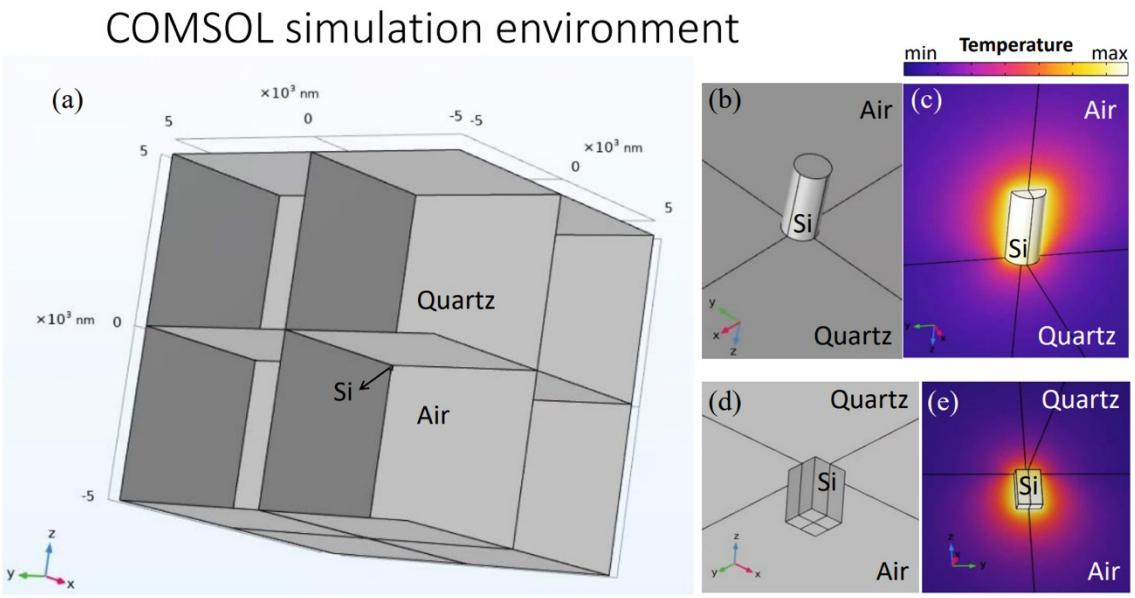

Figure 3.7: COMSOL simulation environment for heating a single silicon nanoparticle. (a) is the environmental setting for heating a nanoparticle. The outer boundary edge length is equivalent to 10 μm. A nanoblock is put on the quartz substrate in the center of the cube structure. The background environment is air. (b) and (d) contain a nanodisk and a nanocube structure, respectively. (c) and (e) are heat maps of a single silicon nanodisk and a nanoblock, respectively. Temperature maps are plotted after the heat simulation is performed. The background environment is set as 300K, the purple color. The positive direction along the z-axis points to the quartz substrate.

doi:10.6342/NTU202501130

3.1.3 Matching simulation results and analytical solutions

To perform the DUV photo-thermo-optical nonlinearity, a few steps should be confirmed. From recent literature, Mie enhanced photothermal nonlinearity of a single silicon nanodisk on quartz was excited at 561 nm[7], and polaritonic resonance of a single silicon nanodisk on sapphire was excited at the DUV wavelength[24]. We checked the Mie analytical solution with Lumerical FDTD simulation, as shown in Figure 3.8, in which I showed my FDTD result compared to Dr. Yusuke Nagasaki's thesis content for confirmation[31].

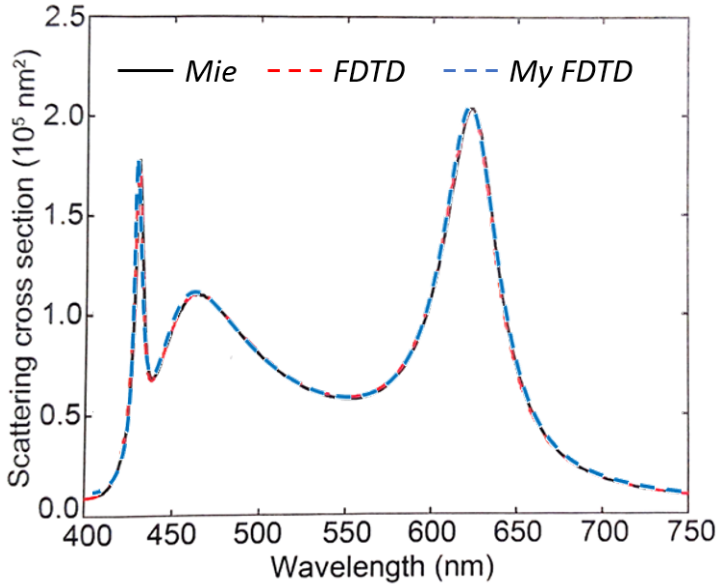

Figure 3.8: Mie analytical solution fits well with Dr. Yusuke Nagasaki's results from the graduate school of Osaka University, Prof. Junichi Takahara's lab[31]. The analytical solution is derived for a n=4, k=0, radius of the 75 nm nanosphere. The black line, Mie analytical solution, and the red dashed line are calculated by

doi:10.6342/NTU202501130

Dr. Nagasaki. The blue dash line is calculated by Lumerical FDTD performed in this thesis.

We also showed the Mie analytical solution for a silicon nanosphere of a radius of 40 nm in Figure 3.9 to confirm a suitable model for checking with smaller particles. The FDTD simulation result fits well in the DUV and visible regions separately.

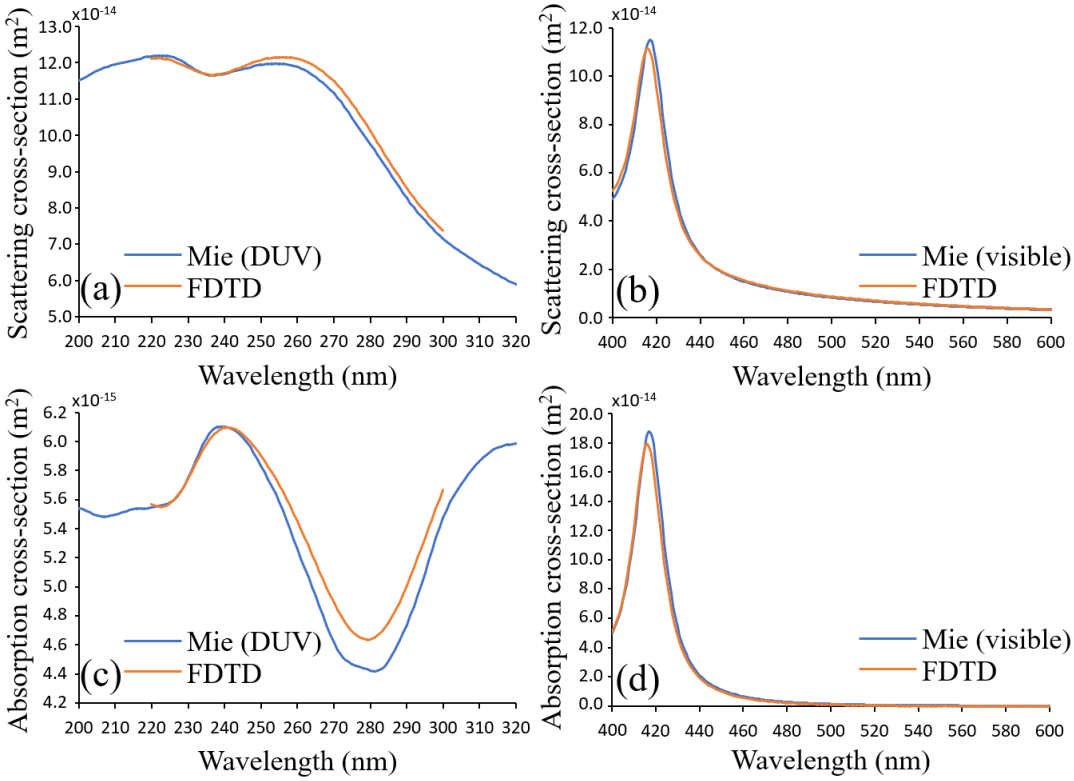

Figure 3.9: Scattering cross-section and absorption cross-section fit well between the Mie analytical solution and FDTD simulation in the visible at 561 nm and the DUV region at 266 nm wavelength. (a) and (b) are Mie scattering cross-sections that fit well with the FDTD simulation in the visible wavelength and the DUV range, respectively. (c) and (d) are Mie absorption cross-sections fitting well with FDTD in the visible wavelength and the DUV range, respectively. FDTD simulation deviates from the Mie analytical solution at 266 nm by about 2.66%. The reason for the deviation comes from the fitting of the refractive

doi:10.6342/NTU202501130

index input to the FDTD simulation. The refractive index data was obtained from [7].

So far, we have already demonstrated the deviations from the analytical solutions. Also, the simulation of photothermal nonlinearity according to the paper published[7] was reproduced in Figure 3.10, left columns, (a) (c) (e), which are consistent with (b) (d) (f).

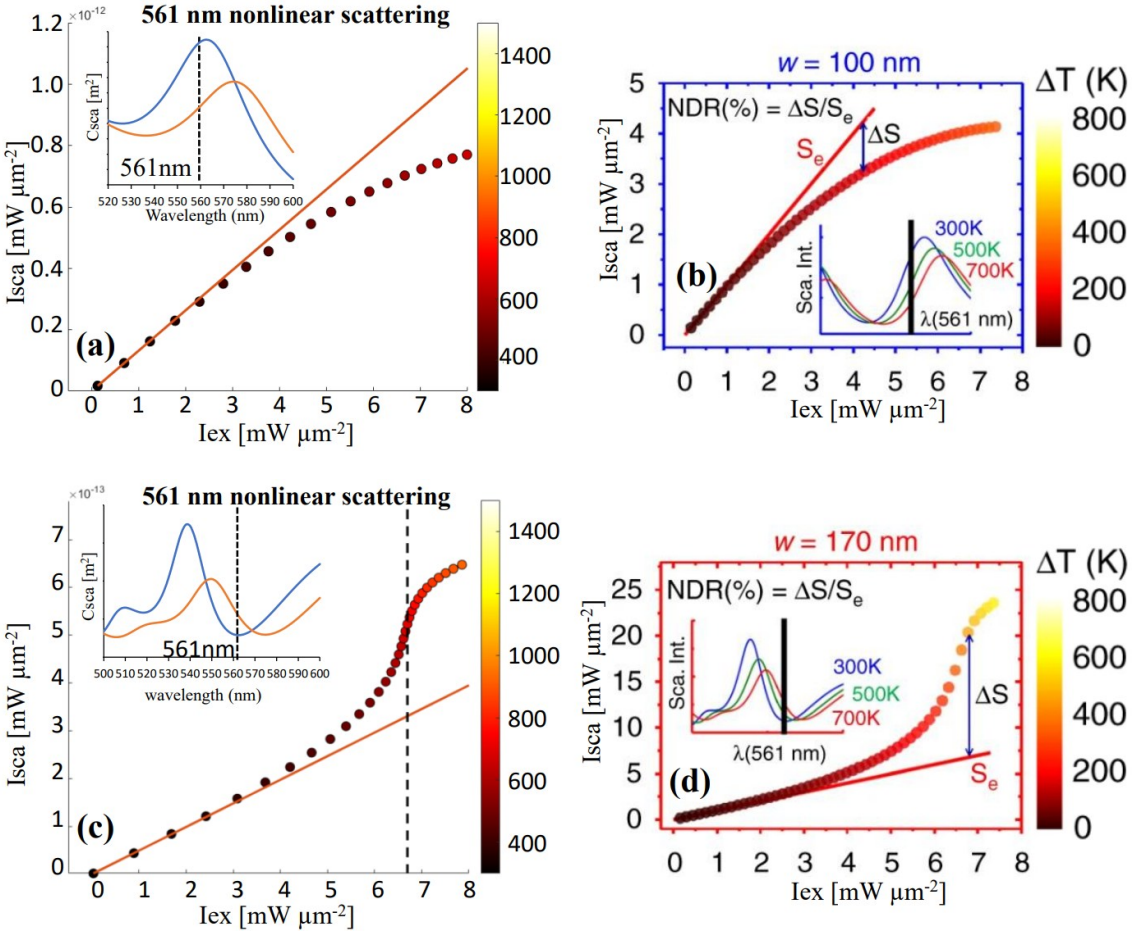

doi:10.6342/NTU202501130

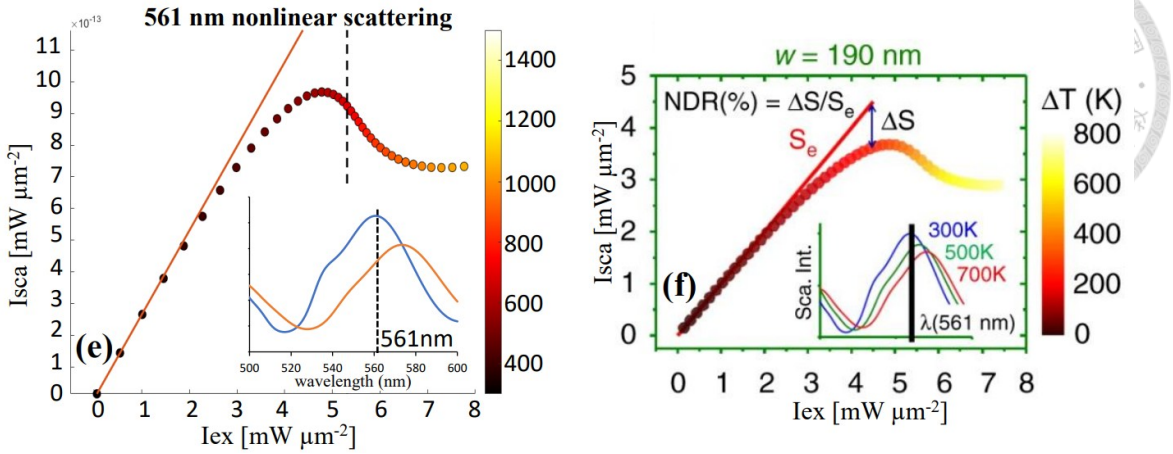

Figure 3.10: Simulation of photothermal nonlinear scattering for single silicon nanodisks with widths of 100, 170, and 190 nm. A nanostructure with different sizes is excited at a 561 nm wavelength to induce various types of Mie resonances, demonstrating different forms of nonlinearity, including (a) and (b) for saturated scattering (SS), (c) and (d) for super-linearity, and (e) and (f) for reverse SS. The three figures in the right column, (b), (d), and (f), were reproduced from [7].

Since we aimed at simulating the polaritonic resonance of a silicon nanostructure in the DUV region, silicon lying on a quartz substrate was reported to show polariton resonance[24,79]. Figure 3.11 (c) shows the polaritonic resonance induced in a silicon nanodisk according to [26]. We reproduced the simulation of the scattering cross-section, Figure 3.11 (a), and the extinction cross-section, Figure 3.11 (b), and found that our reproduced scattering cross-section is closer to the extinction cross-sections shown in Figure 3.11 (c)[24]. The possible reason comes from the inconsistency of the imaginary part of the refractive index used. From Figure 3.11 (b) and (c), polaritonic resonance peaks show a similar redshift with increasing radius. We also reproduced the electric field

doi:10.6342/NTU202501130

intensity in Figure 3.12 (b)-(e), which shows a clear hotspot, *i.e.,* localized electric field enhancement. On the border of the silicon contacting with quartz, an electric field penetrating the substrate magnifies dilated hotspots.

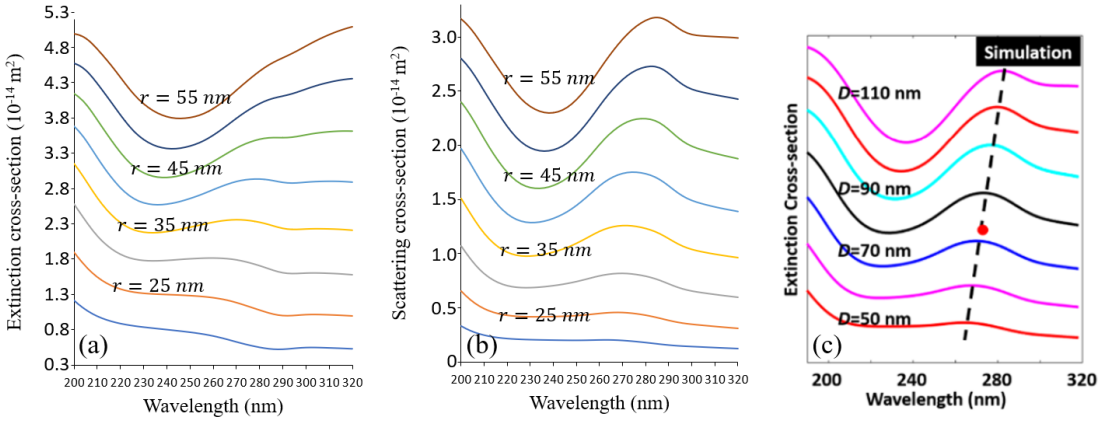

Figure 3.11: Simulation of a silicon nanodisk lying on sapphire for showing extinction cross-section in (a) and scattering cross-section in (b), indicated in the left and middle graphs. The right graph (c) were the extinction cross-sections reproduced from [24]. Compared to our simulation, the reference paper showed an extinction cross-section result similar to the scattering cross-section in the simulation demonstrated here. The reason behind this lies in the differences in the imaginary part of the refractive index of the sapphire used.

doi:10.6342/NTU202501130

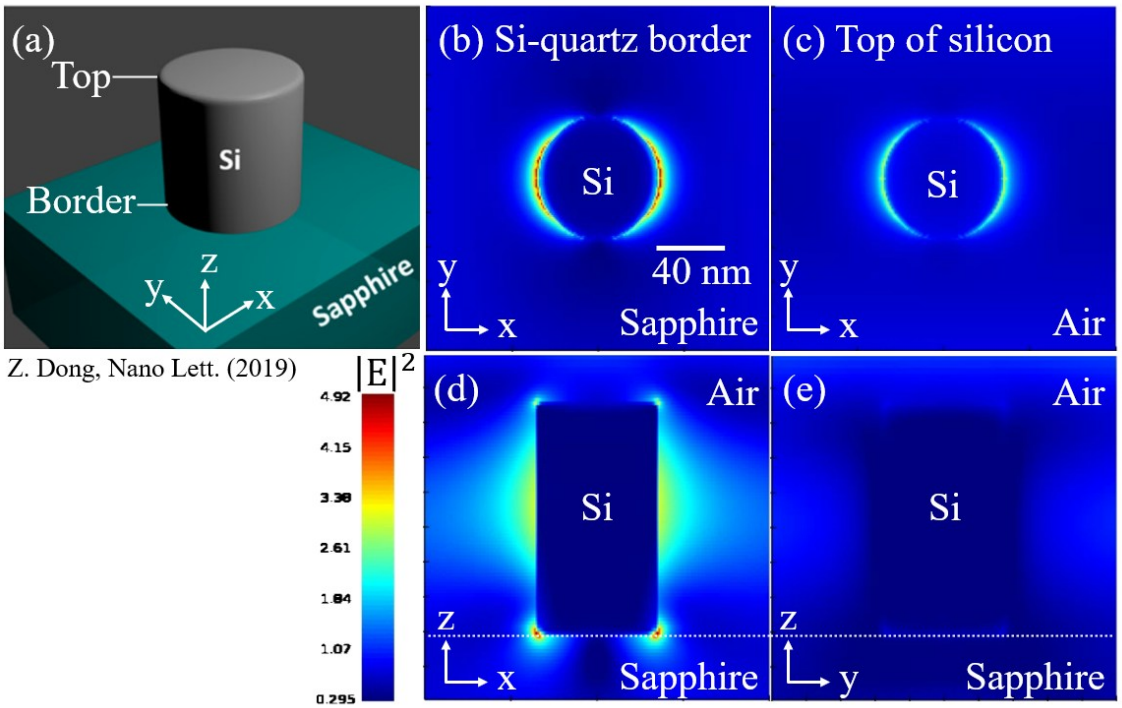

Figure 3.12: Electric fields of a silicon nanodisk lying on the sapphire substrate. (a) shows the electric field profile with corresponding positions, containing xy-view of (b) Si-quartz border, (c) the top of silicon, xz-view in (d), and yz-view in (e). The electric field is polarized along the x-direction, and hotspots are shown in the xz-view in (d). The electric field in (e) is weak. (a) was reproduced from reference [24].

3.2 Experimental preparation

We'll demonstrate steps for measuring photothermal nonlinear scattering excited under a 266 nm laser. Nevertheless, while we checked the reversibility and repeatability of the same sample, it showed a tendency closer to linearity with fluctuations.

In the preparation step, we first introduced the fabrication process of shuffled silicon nanoarrays as shown in sections 3.2.1 and 3.2.2. Afterward, two optical light paths,

doi:10.6342/NTU202501130

one for spectra measurement under white light illumination are shown in section 3.2.3, and the other light path is used to measure photothermal nonlinear scattering under 266 nm laser excitation, shown in section 3.2.4.

3.2.1 Layout of shuffled silicon nanoarrays

PSO indicates the nanodisk has a best radius of 36 nm. We designed the layout of silicon shuffled arrays according to a paper published in 2019[24]. A unit array in the layout is a randomly distributed unit of area 11 μm^2. A whole array is the periodic shuffled array of area 100×100 μm^2 as shown in Figure 3.13. We designed 45 numbers of areas100×100 μm^2 with four different doses in electron beam lithography (EBL), with doses 475, 500, 525, and 550 $\mu C/cm^2$, and repeated 5 patterns for each dose, as shown in Figure 3.14. Figure 3.14 (a) is the top view of the 11 cm^2 silicon on a quartz wafer. The pattern is located in the center, indicated by the pink color in (a). Figure 3.14 (b) shows the arrangement of 45 arrays patterned by EBL. An arrow as a mark is written on the wafer.

doi:10.6342/NTU202501130

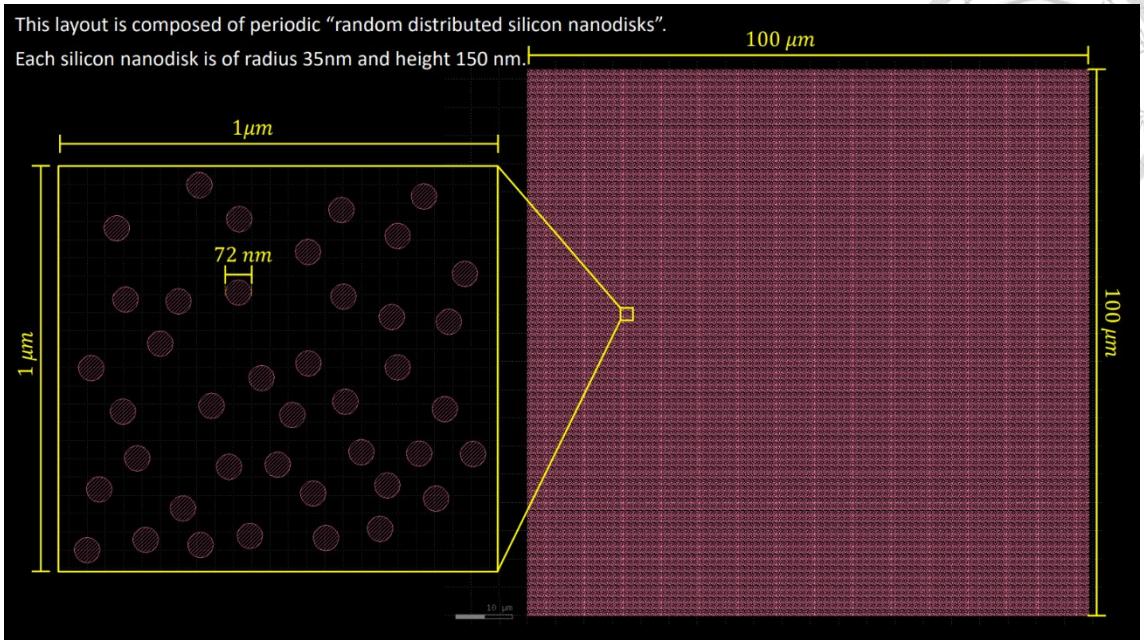

Figure 3.13: The layout of shuffled nanodisk arrays of a radius of 36 nm according to the PSO result. A unit cell is a silicon nanodisk of radius 36 nm. A unit array cell is 1×1 μm^{2,} randomly distributed silicon nanodisks. A whole shuffled silicon nanodisk array is of the area 100×100 μm^2. The distance between the neighboring two arrays is 20 μm.

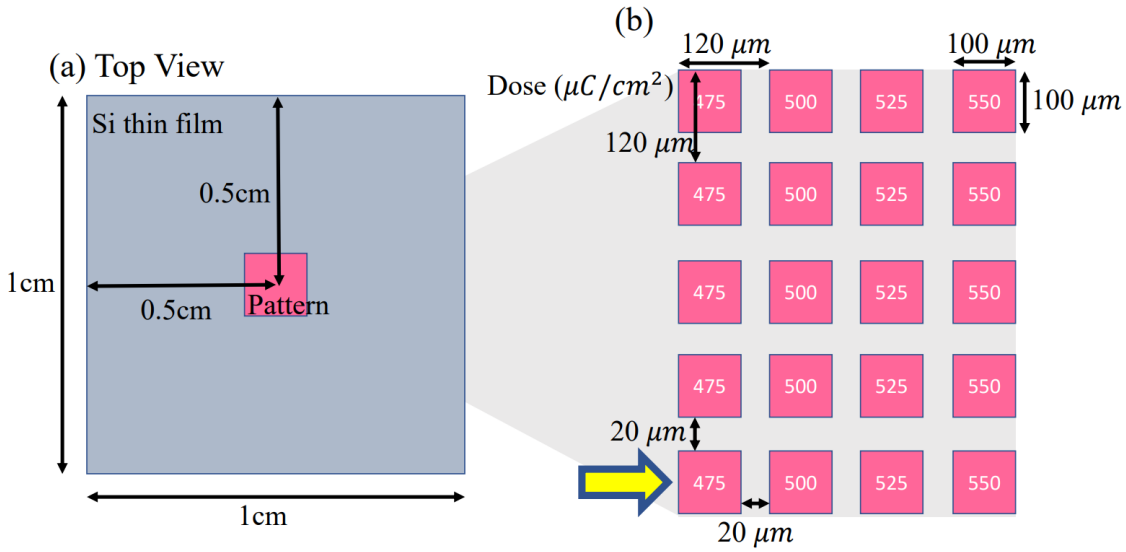

Figure 3.14: The 4×5 numbers of arrays are arranged to be patterned by EBL. (a) Patterns are written in the center of a 1×1 cm^2 silicon nanodisk array on a quartz wafer. (b) Arrays patterned contain four sets of

doi:10.6342/NTU202501130

electron beam doses, 475/ 500/ 525/ 550 μC/cm^2. The distance between the two arrays is 20 μm. An arrow as a mark is labeled on the arrays.

3.2.2 Fabrication process of shuffled silicon nanoarrays

Our sample is composed of shuffled silicon nanodisk arrays, which are cooperated with Prof. Junichi Takahara's lab from Osaka University[62] and Prof. Ming Lun Tseng's lab[63] from National Yang-Ming Chiao-Tung University. The wafer is the 150-nm-thick monocrystalline silicon on a quartz substrate (Shin-Etsu Chemical Co., Ltd.). We used PSO optimization to determine the radius of 36 nm in a unit cell. A shuffled array is composed of monocrystalline silicon nanodisk arrays of radius 36 nm and 150 nm height arranged in a shuffled distribution of an average period of 75 nm.

Si shuffled nanostructures acting as polaritonic resonators operating in the DUV wavelengths were fabricated by the schematics shown in Figure 3.15. The overall process flow is identical to that mentioned in the paper[7]. Nevertheless, the photoresist is changed to polymethyl methacrylate (PMMA) due to a lack of surface attachment leading inhomogeneity. The fabrication process is described in the following Figure 3.15:

doi:10.6342/NTU202501130

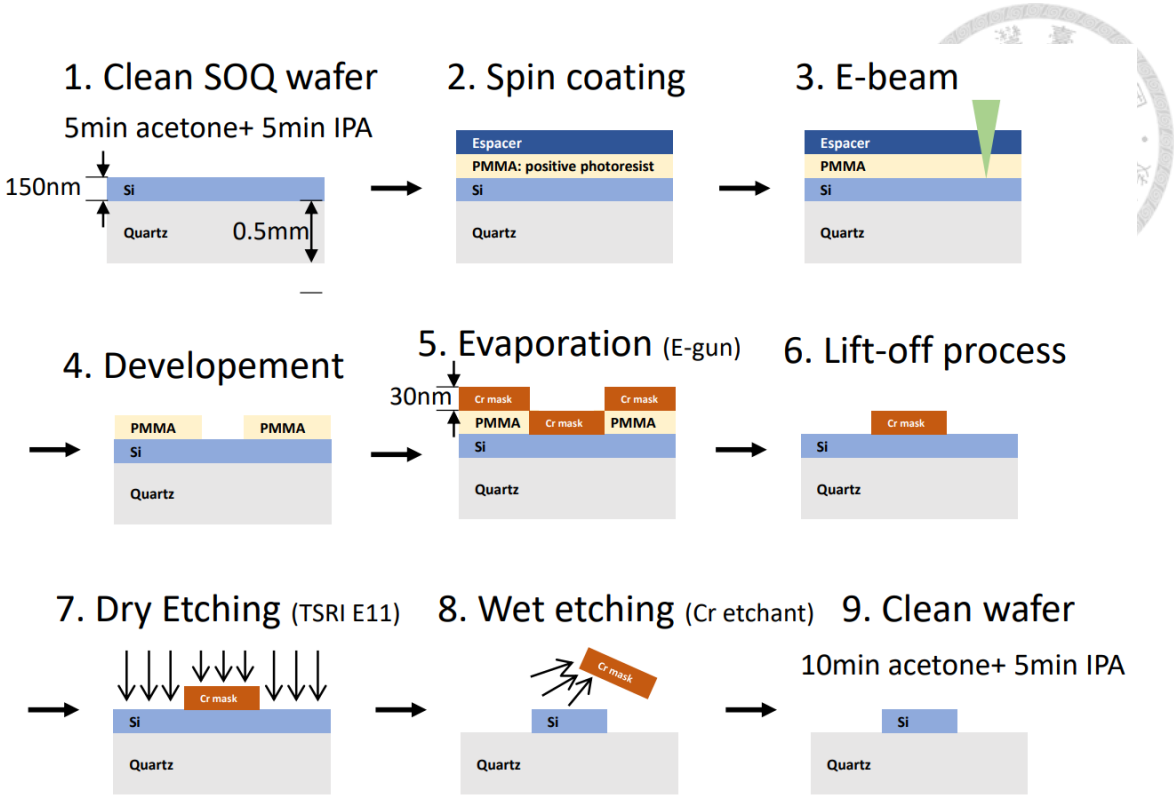

Figure 3.15: Fabrication of shuffled silicon nanodisk arrays. The fabrication processes originate from the paper referenced[7]. The nine steps, start from wafer cleaning, spin coating, electron beam lithography, development, evaporation, lift-off process, dry etching with mask, wet etching to remove mask, and end with wafer cleaning.

Step 1: Sample preparation

Silicon on quartz substrate (SOQ) wafer (supported by Prof. Takahara's lab, manufactured by Shin-Etsu Chemical Co.) was ultrasonicated and cleaned with acetone for 5 minutes and isopropyl alcohol (IPA) for 5 minutes. We are grateful to cooperate with this wafer with Osaka University, Prof. Junichi Takahara's lab. The fabrication processes below are cooperating with National Yang-Ming Chiao-Tung University, associated with Prof. Ming Lun Tseng's lab.

doi:10.6342/NTU202501130

Step 2: Surface coating PMMA and Espacer

SOQ was coated with polymethyl methacrylate (PMMA) as a positive photoresist on the surface. In this step, the SOQ wafer was dried at 180 °C hot plate for 5 minutes, spin-coated with PMMA at 2200 rpm for 10 seconds, and hard-baked at 180 °C for 2 minutes to solidify the photoresist. PMMA was better attached to the surface than ZEP520A (a chemical resist, Zeon Corp.) in our testing, thus showing a better homogeneity on the surface. Furthermore, since SOQ is not a good conductor, it was coated with Espacer to enhance the conductivity for being exposed to the electron beam lithography in the next step. Therefore, we attached an Espacer with 1000 rpm for 10 seconds and 3500 rpm for 50 seconds and soft-baked the wafer at 90 °C for 90 seconds.

Steps 3 and 4: Electron beam lithography

SOQ was coated with positive photoresist PMMA. Electron beam (EB) lithography (Raith VOYAGER) went with an acceleration voltage of 50 keV, dose time of 500~550 μC/cm^2, and field size of 500 μm. After the lithography, the wafer was soaked in MIBK/IPA developer and then IPA. This step starts with removing the Espacer in water for 60 seconds, then moving into MIBK for 70 seconds, and IPA for 60 seconds.

Steps 5 and 6: Patterned-metallic mask deposition

A 30 nm-thick Cr layer was deposited on the hard mask using an evaporator (ULVAC EBX-10C) with an evaporation rate of 0.4 Å/s for the initial 5 nm, followed by

doi:10.6342/NTU202501130

0.1–0.2 Å/s when the deposition thickness exceeded 5 nm. Cr mask preparation was finished after the lift-off process, in which the photoresist was removed, with immersion in acetone overnight, around 12 hours. The redundant Cr mask was removed in acetone by ultrasonic lift-off for 10 to 30 minutes.

Steps 7, 8, and 9: Pattern formation

The silicon layer was etched by plasma gases in a reactive ion etching chamber (LAM2300-BEOL 8” Etcher). The etching rate between Cr and Si is about 2.08. It is a dry etching that makes good use of ion bombardment, featuring anisotropic etching to form an almost perpendicular silicon nanopillar. After finishing the etching, the sample was immersed in Cr etchant overnight to remove the mask. It was taken out and ultrasonically cleaned with acetone for 10 minutes and IPA for 5 minutes.

3.2.3 Setup for spectrum measurement

We use an ultra-broadband light source[69] (ISTEQ, XWS-30, wavelength range: 190nm–2500 nm) in the light path to measure the spectra of shuffled silicon arrays down to the DUV wavelength. A schematic of the setup is shown in Figure 3.16. The white light was collimated by three Al-coated off-axis parabolic mirrors[70] and entered a polarizer (Thorlabs RPM10)[71] associated with an elongated light path for separating s-p waves. Therefore, to match the simulation results, polarized light is incident on the sample through a low-NA objective (NA 0.4, Mitutoyo plan UV infinity corrected objective). The

doi:10.6342/NTU202501130

backward scattering signal is split into two light spots of different wavelength regions, featuring blue and orange color spots. The blue light is collected to the camera, passing through a 50/50 beam splitter (BS1, Thorlabs BSW20). To capture the DUV spectrum with an undiminished signal, the second beam splitter (BS2, Thorlabs BSW10R) is removed from the light path to prevent attenuation of light intensity entering the spectrometer (OtO Photonics, EagleEye EE2063, wavelength resolution: 0.2 nm). The white light path is shown in Figure 3.16.

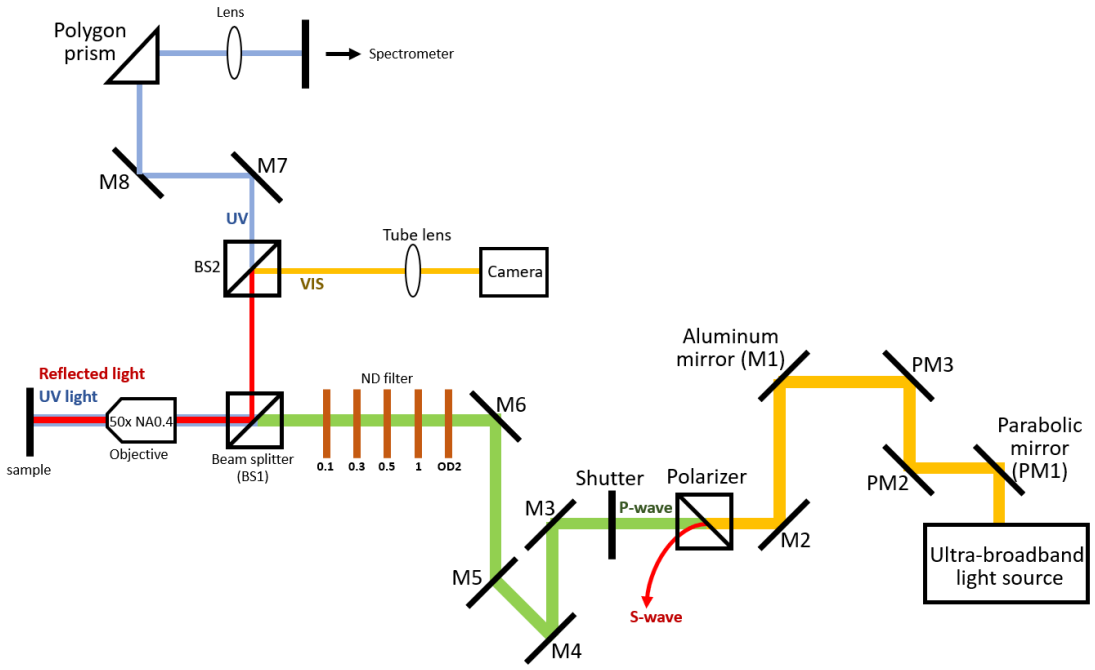

Figure 3.16: The white light path for measuring spectra. Ultrabroadband light source[69] passes through three parabolic mirrors[70], two UV-enhanced aluminum mirrors, and is incident on a Rochon prism as a polarizer[71] to separate s-p waves from a polarized incident light. Polarized light passing through flip neural-density (ND) filters and an objective lens of numerical aperture (NA=0.4, Mitutoyo, 50x) is incident on the sample. The reflected light going through a beam splitter (BS1, Thorlabs BSW20) is separated by a beam splitter

doi:10.6342/NTU202501130

(BS2, Thorlabs BSW10R) and collected by a camera and the spectrometer.

3.2.4 The 266 nm setup for measuring photothermal nonlinear scattering

Noting that the transmission of a shuffled array of identical cells is equivalent to the forward-scattering of a single silicon nanodisk. Since we used an array, as shown in Figure 3.13, laser-illuminated in the experiment, we'll rephrase the forward scattering in simulation to transmission in an experiment. The 266 nm laser light path is shown in Figure 3.17. The 266 nm laser light has a spot size of 0.5 μm in diameter and is beam expanded to be incident on the sample through an objective lens (NA 0.36, Mitutoyo plan UV infinity corrected objective). We can measure the reflection and transmission of light via a removable beam splitter (BS) put in the cage system. The reflection light path is used to measure the power of the laser light incident on the sample. Removing the BS, we can measure the transmission light passing through the sample and collect the scattering signal via a photodetector. To extract signals captured by a photodetector (PDA10A2), we connect the photodetector to an Arduino board (UNO R3) and record the signal with Python code. (This code is supported by Prof. I-Lin's lab at National Central University. I modified the code by adding a recording function.)

doi:10.6342/NTU202501130

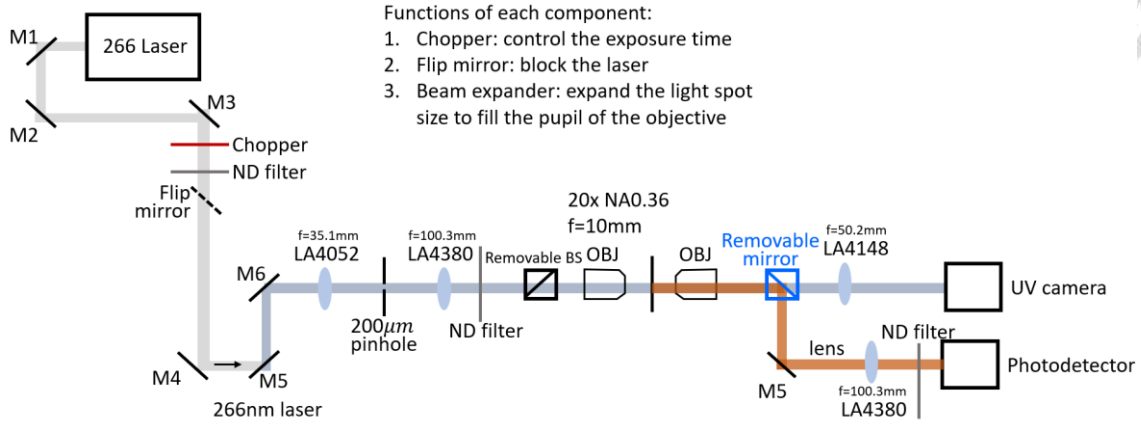

Figure 3.17: The 266 nm laser light path for measuring the nonlinear scattering. The laser light is beam-expanded using two uncoated plano-convex lenses, passes through an ND filter and a low-NA objective lens, and illuminates the sample. The transmission signal passes through an identical objective lens and a plano-convex lens to focus incident light on the photodetector to measure the nonlinear scattering signals.

It contains 6 mirrors in the 266nm illumination light path, causing a debilitated reflectance from 83.63 mW to 62.8 mW in front of the incident objective lens. The measured reflectance from each mirror in front of the incident objective is 0.9375 (M1), 0.9566 (M2), 0.92 (M3), 0.9777 (M4), 0.9765 (M5), 0.9536 (M6), 0.97536 (M7, in the collected light path). After the light incident on the objective (OBJ1), the power is lowered to 34.5 mW. To detect the transmitted scattering signal, we put a photodetector behind the light-collected objective (OBJ2) and a plano-convex lens in front of the photodetector.

doi:10.6342/NTU202501130

Sample images:

[Step 1] Shrinking the light spot to a diameter of 25 μm.

[Step 2] Finding the sample from the arrowhead. The edges of each sample block are clear, so it is easy to locate the sample, pattern 4.

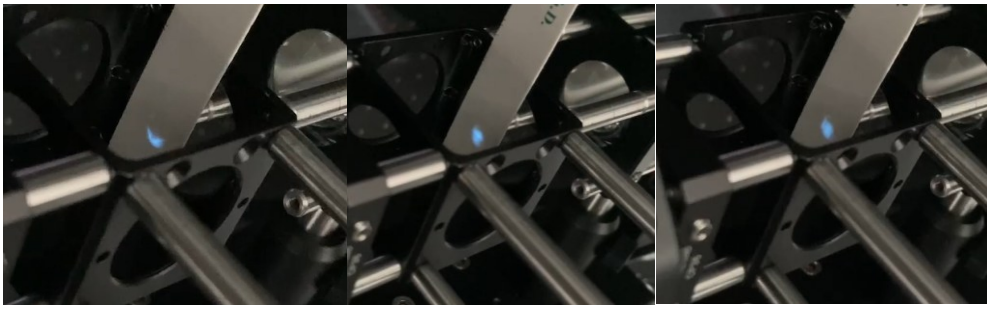

On the last day of our experiments, the camera malfunctioned. Therefore, we used photoluminescence from the paper to localize the sample. Luckily, the experiments were completed smoothly.

doi:10.6342/NTU202501130

Chapter 4 Simulation results

In this chapter, the simulation results show cross-section spectra of a silicon nanodisk on a quartz structure in Figure 4.1, and the electric field profiles are shown in Figure 4.2. The Second results are the modulation depth with different radii near 36 nm. In the photothermal nonlinear scattering result, we choose a radius of 35 nm, and a 0.1% modulation depth difference is predicted from that of 36 nm. The demonstrated photothermal nonlinear scattering includes total, forward, and backward scattering. The nonlinear scattering curve is consistent with the modulation depth estimated between the scattering spectra of 300K and 700K. Last but not least, the nonlinear curve is plotted as a saturated PSF. The resolution enhancement is obtained by subtracting nonlinear signals from the linear signal. We obtained a 1.38-fold smaller PSF and the resolution enhancement based on the SAX using the differential excitation method.

4.1 Polaritonic resonance of a single silicon nanodisk on a quartz substrate in the DUV region

We used Lumerical to demonstrate the polaronic resonance of a single silicon nanodisk on the quartz substrate. The reason we don't use the sapphire substrate is due to the material consistency established in our previous work in [7]. The simulation results are demonstrated in Figure 4.1. We can observe a clear peak redshift in the scattering cross-

doi:10.6342/NTU202501130

section shown in Figure 4.1(b) with increasing radius, reminiscent of the result shown in Figure 3.11 (b). It is reasonable to show peak redshift in almost the same wavelength because sapphire has n around 1.83 while quartz has n around 1.5 around 266 nm wavelength. From the electric field shown in Figure 4.2, we observe the same featured field profiles demonstrated in Figure 3.12. Figure 4.2 (a) shows that the simulated structure is a silicon nanodisk lying on the quartz substrate. Figure 4.2 (b) and (c) are electric field profiles in xy-view on the silicon-quartz border and the top of the silicon disk. Figure 4.2 (d) and (e) are the xz-view and yz-view, respectively. Hotspots occur in the corner along the electric-field polarizing direction, shown in (d).

In previous studies of a metallic nanostructure, both linear and nonlinear scattering are greatly enhanced by surface plasmon resonance (SPR). Wavelength-dependent and intensity-dependent studies reveal that the physical origin is due to nonlinear absorption, meaning that the absorption coefficient becomes smaller with increasing excitation intensity.

doi:10.6342/NTU202501130

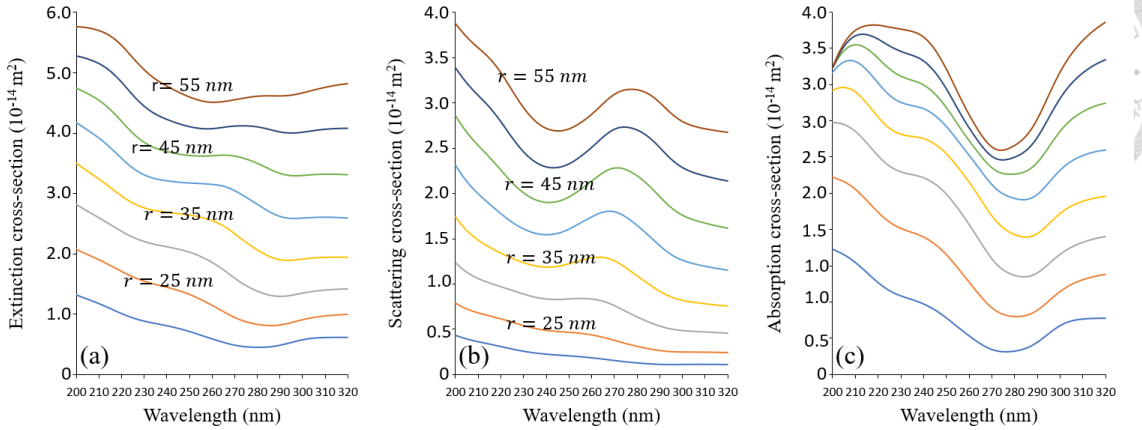

Figure 4.1: Simulation of a single silicon nanodisk lying on a quartz substrate with the results shown in (a) extinction cross-section, (b) scattering cross-section, and (c) absorption cross-section.

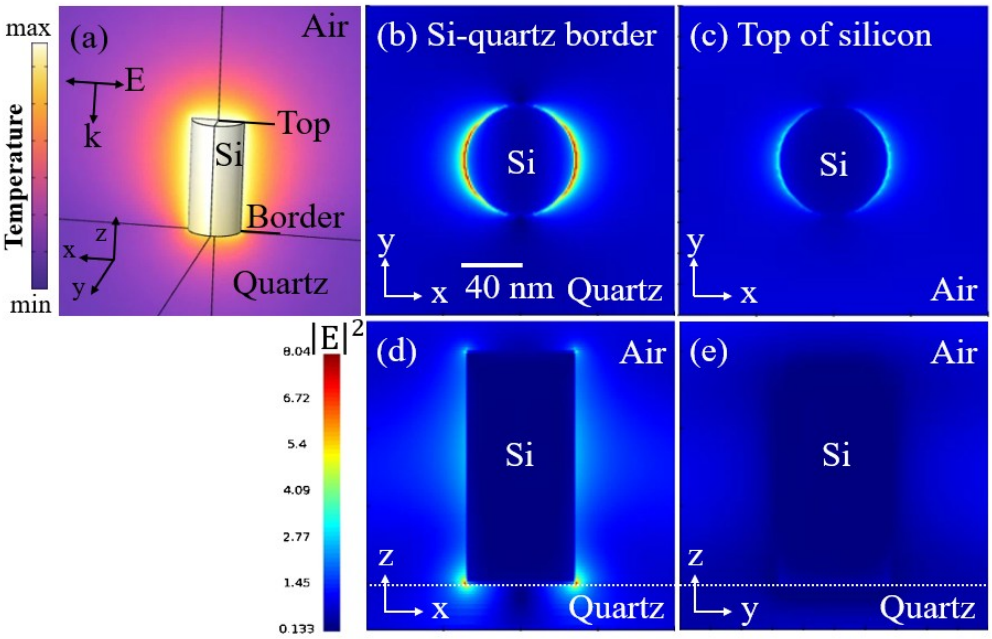

Figure 4.2: Electric field distributions of a silicon nanodisk on a quartz substrate. (a) The color represents temperature, indicating the heating of the nanostructure. (b) In the x-y view, at the quartz-silicon interface, the electric field enhancement is stronger than at the top of the silicon nanodisk. (c) In the x-y view, at the Si-air boundary (the top of the nanodisk), the electric field enhancement is weaker than in the region shown

doi:10.6342/NTU202501130

in (b). (d) shows the x-z view, illustrating that the hot spot corresponds to the electric field polarized along the x-direction. (e) presents the y-z view, demonstrating the disappearance of the hot spot perpendicular to the electric field polarization.

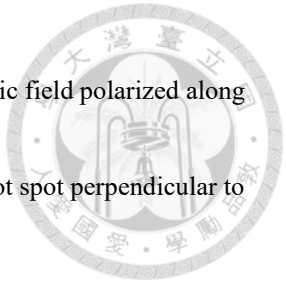

4.2 Optimization of the radius of a single silicon nanodisk in Lumerical

Two particle models are constructed based on the simulation setup described in the Methods section and illustrated in Figure 4.3. Through PSO optimization in Lumerical, an optimal radius of 36 nm was obtained. The modulation depths for different radii are shown in Figure 4.3. Since the model used for PSO optimization (as shown in Figure 3.5) includes minimal polaritonic coupling, this effect can be considered negligible. The orange curve in Figure 4.3, which shows a slight indication of polariton coupling, closely matches the result calculated using a single silicon nanodisk (navy blue curve). The modulation depth of different radii from 35 nm to 40 nm shows a modulation depth of 5.7% without using a function sweep, which is consistent with the PSO showing maxima of radius of 36 nm.

A brief comparison of the 5.7% modulation depth can be made with Figure 2.4 (b). The permittivity in the DUV region shows a real part variation of 20.4% and an imaginary part variation of 10.36%. It is counterintuitive that it only shows 5.7% modulation depth with the permittivity varying between 10.36% to 20.4%. To resolve this

doi:10.6342/NTU202501130

ambiguity, we first clarify the inherent optical properties of bulk silicon by examining its normal-incidence reflectivity, as described in eq. 4.2.1. In the simulation process, while we expand the radius of a silicon nanodisk for calculating the scattering cross-sections, it shows red-shifting and stop to increase in its intensity, resembling that of a silicon mirror. The reflectivity is shown below

$$R_0 = \left|\frac{n_1+n_2}{n_1-n_2}\right|^2 = \frac{n_1^2-2n_1+1}{n_1^2+2n_1+1} = \frac{\varepsilon_0-\Delta\varepsilon-2\sqrt{\varepsilon_0+\Delta\varepsilon}+1}{\varepsilon_0+\Delta\varepsilon+2\sqrt{\varepsilon_0+\Delta\varepsilon}+1} = 1-\frac{4\sqrt{\varepsilon_0+\Delta\varepsilon}}{\varepsilon_0+\Delta\varepsilon+2\sqrt{\varepsilon_0+\Delta\varepsilon}+1} \quad \text{(eq. 4.2.1)}$$

, with $n = \sqrt{\varepsilon_r\mu_r} = \sqrt{\varepsilon_r} = \sqrt{\varepsilon_0 + \Delta\varepsilon}$ and ε_0 is used for 300K and $\Delta\varepsilon$ is existing for the temperature of 700K. $R_{300K} \sim 0.396$ (reflection at 300K, with $\varepsilon_0 = 19.3$) and $R_{700K} \sim 0.4145$ (with $\varepsilon_0 + \Delta\varepsilon = 21.3$). The corresponding modulation depth is defined as $\frac{(R_{700K}-R_{300K})}{R_{300K}} \cong 0.0467 = 4.67\%$. After expressing the results in terms of reflectivity, the comparison between the optimized nanostructure and bulk silicon appeared reasonable. Secondly, if we discuss a Mie sphere in air with its modulation depth according to eq. 2.4.1, a 5.7% modulation depth is obtained. This value is equivalent to the optimized silicon nanodisk lying on the quartz substrate. It seems that a discussion on the shape and the environment are important. The existing of substrate for a nanostructure is related to the coupling of magnetic resonance, which means the magnetic dipole (MD) driven by the incident electric field couples to displacement current loops. Therefore, the result to somehow proves that the nanostructure lying on the quartz substrate is lack of magnetic resonance. According to the paper published in 2016[64], changing shapes from a

doi:10.6342/NTU202501130

cylinder to a sphere with its shape remaining unchanged results in the enhancement of MD resonance. Here, we didn't see enhanced modulation depth, meaning that localized surface polaritonic resonance is not able to generate a stronger MD resonance.

Since two particles exist simultaneously and contain a polariton coupling effect, we calculated the modulation depth in two ways without using PSO optimization. One way uses the model mentioned in Figure 3.6, in which we calculate the modulation depth of 300K and 700K separately without polariton coupling, as shown in the navy blue line in Figure 4.3. We also calculate the modulation depth without using the PSO function, indicated by the orange line. We selected spectra calculated at 300K and 700K because 700K is the highest temperature of the refractive index measured[7]. Calculation without polariton coupling results in a 1% larger modulation depth compared to the bulk silicon. To sum up, modulation depth calculated with or without PSO shows a maximum of a single silicon nanodisk of radius of 36 nm,

doi:10.6342/NTU202501130

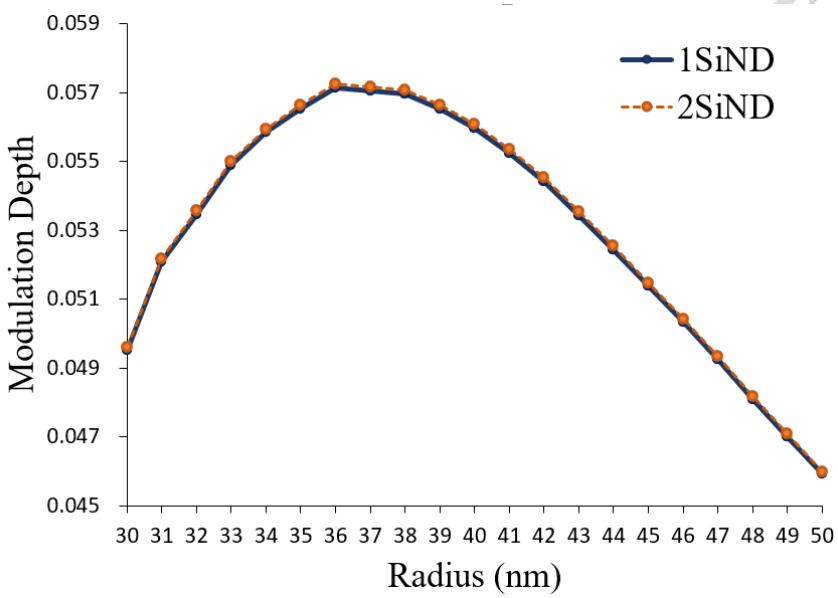

Figure 4.3: The modulation depth was calculated separately for a single nanodisk at 300K and 700K, and two-particle models were used to obtain the modulation depth simultaneously at both temperatures. Two models show almost identical results, meaning that polariton coupling is negligible and PSO results are reliable. The refractive index data was taken from [7].

4.3 Photo-thermo-optical nonlinearity of a silicon nanodisk on quartz excited at 266 nm

We calculated photo-thermo-optical nonlinearity, and it shows saturated scattering. In the following simulation, a single nanosphere with a radius of 35 nm is excited under 266 nm wavelength and shows SS. The temperature-dependent refractive index used is shown in Figure 4.4. The refractive index of silicon as a function of temperature at 266 nm is fitted according to the paper[7,65], and the experimental data labeled by orange spots in Figure 4.4 were measured by our previous member Y. L. Tang[66]. The fitting of n is increasing and k

doi:10.6342/NTU202501130

is decreasing from 30K to 793K[65].

To estimate the refractive index in the DUV range, we apply fitting methods based on data from the visible range to support our simulations. A more detailed discussion on the predicted differences compared to Ref. [67] is provided in Chapter 6.

$$n(T)n_0 + a_n * (T - 300[K])\ ;\ a_n = dn/dT \quad \text{(eq. 4.3.5)}$$

$$k(T) = k_0 * e^{(T/T_k)} \quad \text{(eq. 4.3.6)}$$

where $n_0 = 2.21222, a_n = 0.0007957, k_0 = 4.49445, T_k = -10550.7724$.

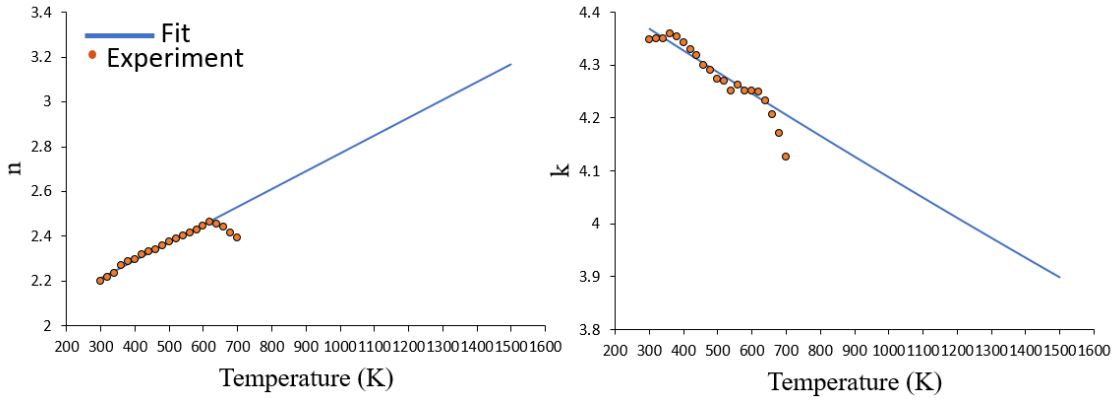

Figure 4.4: Temperature-dependent refractive index of 150 nm thickness silicon nanofilm on quartz at 266 nm wavelength. The refractive index of silicon and quartz, and material properties for thermal simulation, are referred to in the paper[7].

doi:10.6342/NTU202501130

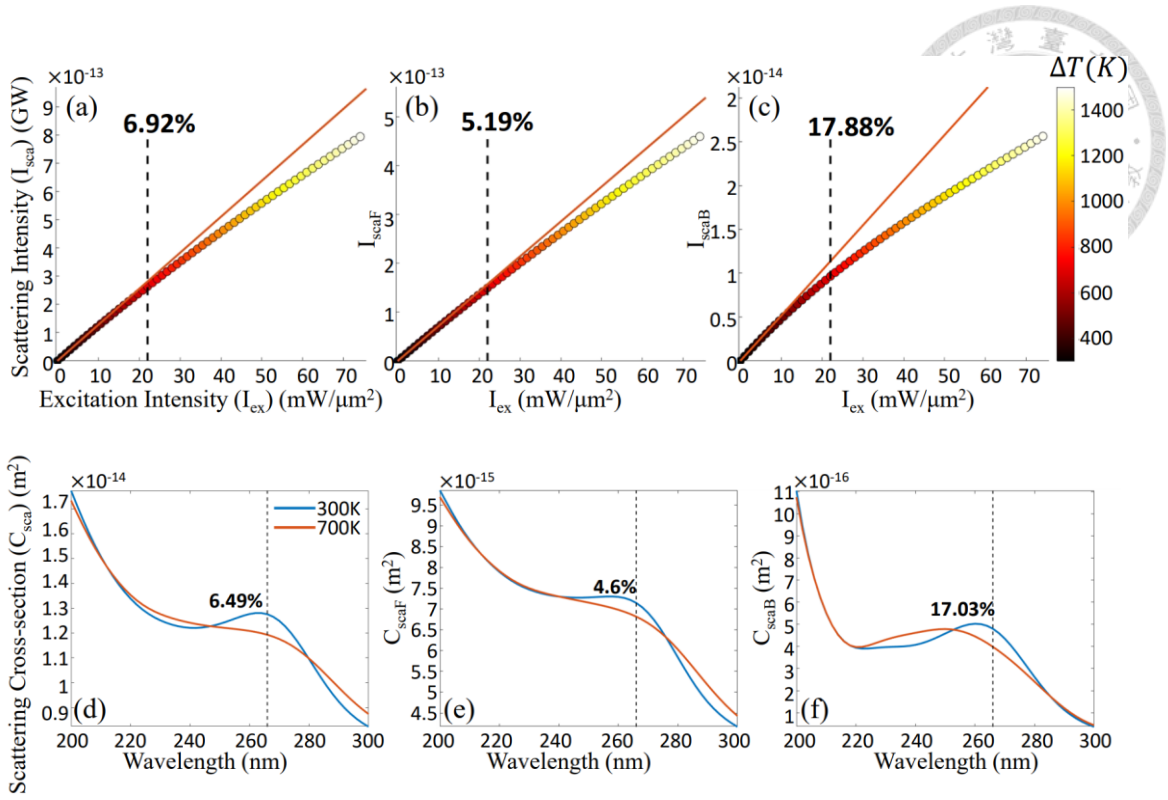

Figure 4.5: Simulation results of photo-thermo-optical nonlinearity from a single silicon nanodisk of radius 35 nm. Three graphs in the upper row, (a)-(c), indicate a nonlinear scattering existing with increasing temperatures. From left to right, they are (a) total scattering intensity with a modulation depth of up to 6.92%, (b) forward scattering intensity with a modulation depth of up to 5.19%, and (c) backward scattering intensity with a modulation depth of up to 17.88%. Temperature differences from 300K to 700K are plotted in black dashed lines. The corresponding 300K (blue line) and 700K (orange line) spectra are shown in the bottom three graphs, (d)-(f). From left to right, it corresponds to (d) the scattering cross-section, (e) the forward-scattering cross-section, and (f) the backward-scattering cross-section. Photothermal nonlinearities are consistent with the modulation depth of temperature-dependent spectra from 300K to 700K.

The simulation contains scattering intensity, forward scattering intensity, and backward scattering intensity for showing photothermal nonlinearity with a modulation

doi:10.6342/NTU202501130

depth predicted to be identical to two temperature-dependent spectra at 300K and 700K in the inset figures of Figure 4.5 (d)-(f). Modulation depth is defined as the density difference between 300K and 700K results. The scattering intensity differing from 300K to 700K shows a 6.92% modulation depth, which is quite consistent with the modulation depth of 6.49% shown in two-temperature spectra. The forward scattering intensity differs by 5.19% from 300K to 700K, and the corresponding modulation depth in scattering cross-section spectra shows a 4.6% modulation depth. The backward scattering intensity shows a 17.88% difference, which is quite consistent with the modulation depth of 17.03% from the two spectra. From the spectra of 300K and 700K, it is clear that the photo-thermo-optical nonlinearity comes from the spectrum being smoothed when the particle is heated.

From temperature-dependent spectra of 300K/ 500K/ 700K shown in Figure 4.6, peaks in spectra decrease and broaden, which proves the photothermal nonlinearity of a silicon nanoparticle excited at 266 nm wavelength is like that of a single gold nanoparticle[68] rather than a clear peak shift with increasing temperatures.

doi:10.6342/NTU202501130

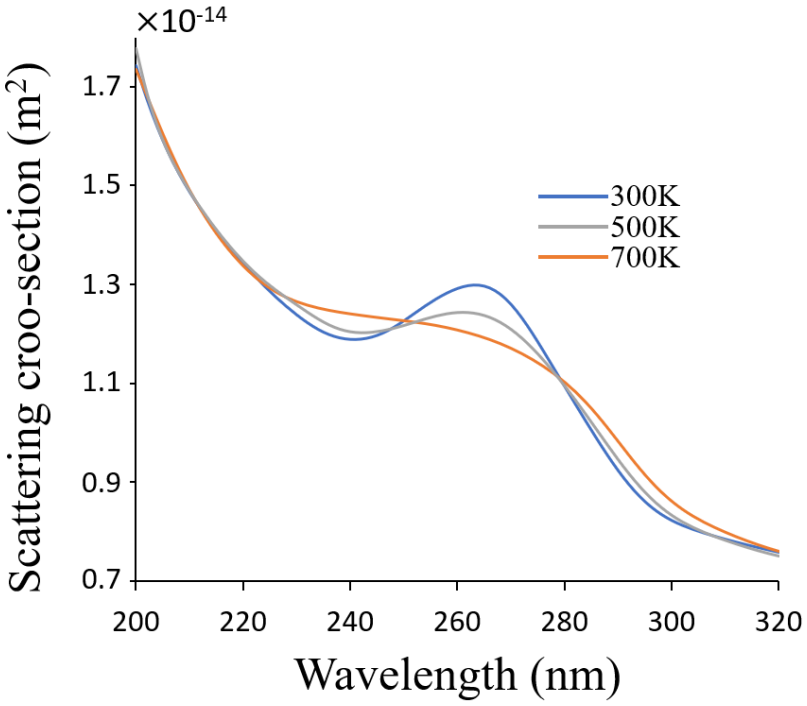

Figure 4.6: Spectra of the radius of 35 nm silicon nanodisk at 300K/ 500K/ 700K. The spectra show flattened and broadened peaks with increasing temperatures. This is proof that a silicon nanodisk excited at 266 nm wavelength is similar to the nonlinear scattering from a nanodisk excited at 561 nm[7].

4.4. dSAX microscopy for resolution enhancement

The dSAX microscopy[69] according to the strategy demonstrated in Figure 2.6, is performed with the signal shown in Figure 4.7. Relations of the photothermal nonlinear scattering (I_{sca}), the linear scattering (I_L), and the nonlinear scattering I_{NL} obtained by subtracting I_{sca} to I_L, i.e. $I_{NL}= I_{sca} - I_L$, are shown in Figure 4.7.

In Figure 4.8, I_L corresponds to a Gaussian function, labeled by the black line, I_{sca} is the saturated scattering intensity, labeled by the green line, and I_{NL} is labeled by the

doi:10.6342/NTU202501130

blue line. The dSAX method is demonstrated by the FWHM of I_L and I_{NL}, as shown in Figure 4.9. The normalized brown line is the FWHM of I_{NL}, and that of the black line is the normalized I_L. The linear signal minus the nonlinear signal, which is the subtraction signal labeled by the blue line. FWHM of the linear signal is 231 nm, and that of the blue line is 167 nm—resolution enhancement with a silicon nanodisk heated up to 700K, showing a 1.38 times resolution enhancement by the dSAX method, as demonstrated in Figure 4.9.

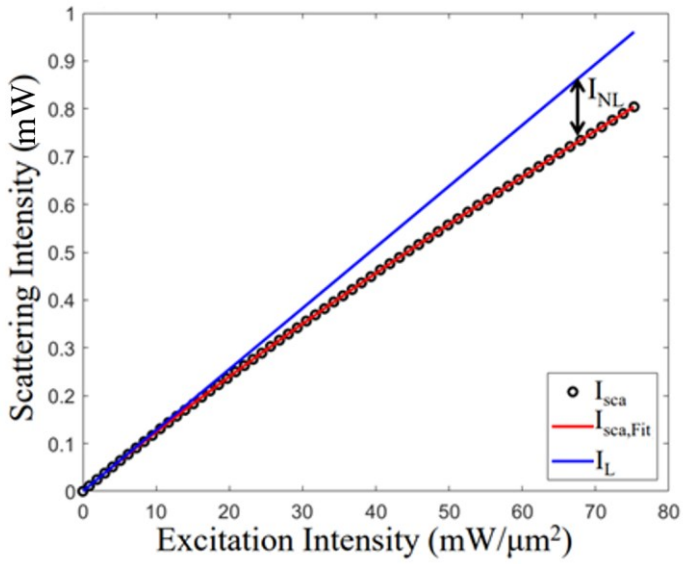

Figure 4.7: Relations between the scattering intensity (I_{Sca}), linear intensity (I_L), and nonlinear intensity (I_{NL}). $I_L=a_1 I_{ex}$ is the linear scattering intensity as shown in eq. 2.5.1. I_{Sca} is the scattering intensity shown in Figure 4.5 (a). I_{NL} comes from I_L minus I_{Sca}.

doi:10.6342/NTU202501130

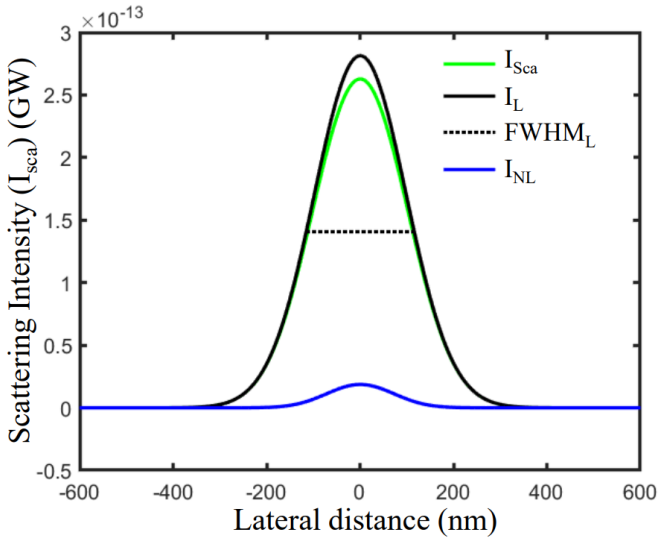

Figure 4.8: SAX microscopy with differential excitation. The black line is a linear signal, I_L (Gaussian function) and the green line is the saturated scattering signal, I_{Sca} (saturated PSF) under 700K, estimated by Figure 4.5.(a). The nonlinear signal, I_{NL} is obtained by (I_L - I_{Sca}).

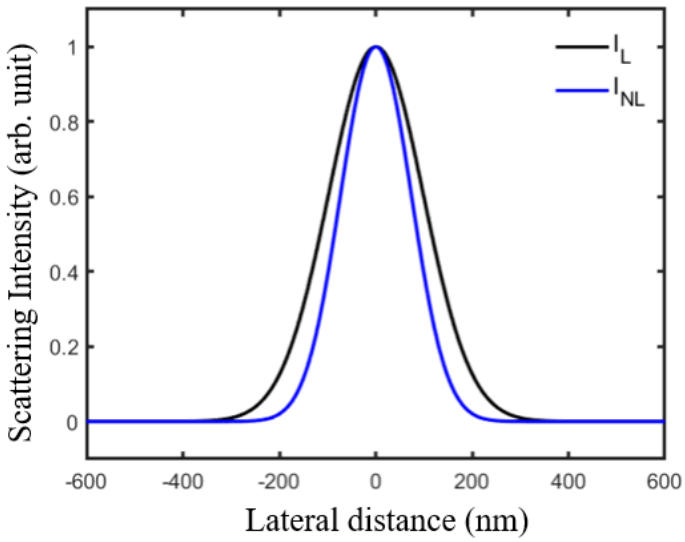

Figure 4.9: Subtraction signal from linear minus nonlinear signal. The FWHM of I_L is 231 nm, and that of I_{NL} is 167 nm, with which we can achieve a 1.38 times better spatial resolution.

doi:10.6342/NTU202501130

Chapter 5. Experimental results

In this chapter, two experimental results are shown. One is the spectra measurement to plot the polariton resonance peak. The other is the experimental results of the photothermal nonlinearity. Nevertheless, due to limited experimental infrastructure, even though we successfully measured the reversibility of scattering nonlinearity, it is difficult to distinguish the trend of nonlinearity at low excitation power due to the noise level, and reversibility has not been achieved in this system. The preliminary experimental results shown in Figure 5.6 are worth recording because the nonlinear scattering patterns align with the reflectance spectrum, which shows a resonance peak in the DUV wavelength range.

Measurement accuracy in experiments is not worthy to be referenced below the incident power of 5 mW, with an illumination spot size of the diameter 25 μm. Nonlinearity between 5 mW to 25.925 mW has fluctuated so that it is difficult to judge the correctness of the experimental data.

5.1 Spectrum measurement in the DUV region

Samples under observation illustrated in Figure 5.1 are measured with the optical light path demonstrated in Figure 3.16. There are 4 x 5 arrays with 4 sets of different doses (475/ 500/ 525/ 550 μC/cm^2) and repeated 5 patterns in each dose, referring to Figure

doi:10.6342/NTU202501130

3.14. We used silicon and aluminum mirrors as the reference spectrum, shown respectively in Figure 5.2 and Figure 5.4. Spectra measured by the aluminum mirror is more fluctuated than those measured by the silicon mirror. An aluminum mirror has higher reflectance, which contributes to spectra of higher sensitivity, compared to bulk silicon. A discussion based on spectra measured by silicon and aluminum mirrors with different 4 sets of doses is shown in Figure 5.3 and Figure 5.5.

Figure 5.3 (a) and Figure 5.5 (a) with a dose of 475 μC/cm^2 show a broad resonance peak in the center of 340 nm, which means the fabrication is failed. In Figure 5.3 (b), (c), (d) and Figure 5.5 (b), (c), (d), we observed that there are resonance peaks in DUV in accordance with successful fabrication parameters. In Figure 5.3 (b) and Figure 5.3 (d), two spectra show resonance peaks in the DUV region. In Figure 5.3 (c), three spectra show resonance peaks in DUV, so dose 525 μC/cm^2 shows the most suitable parameter.

doi:10.6342/NTU202501130

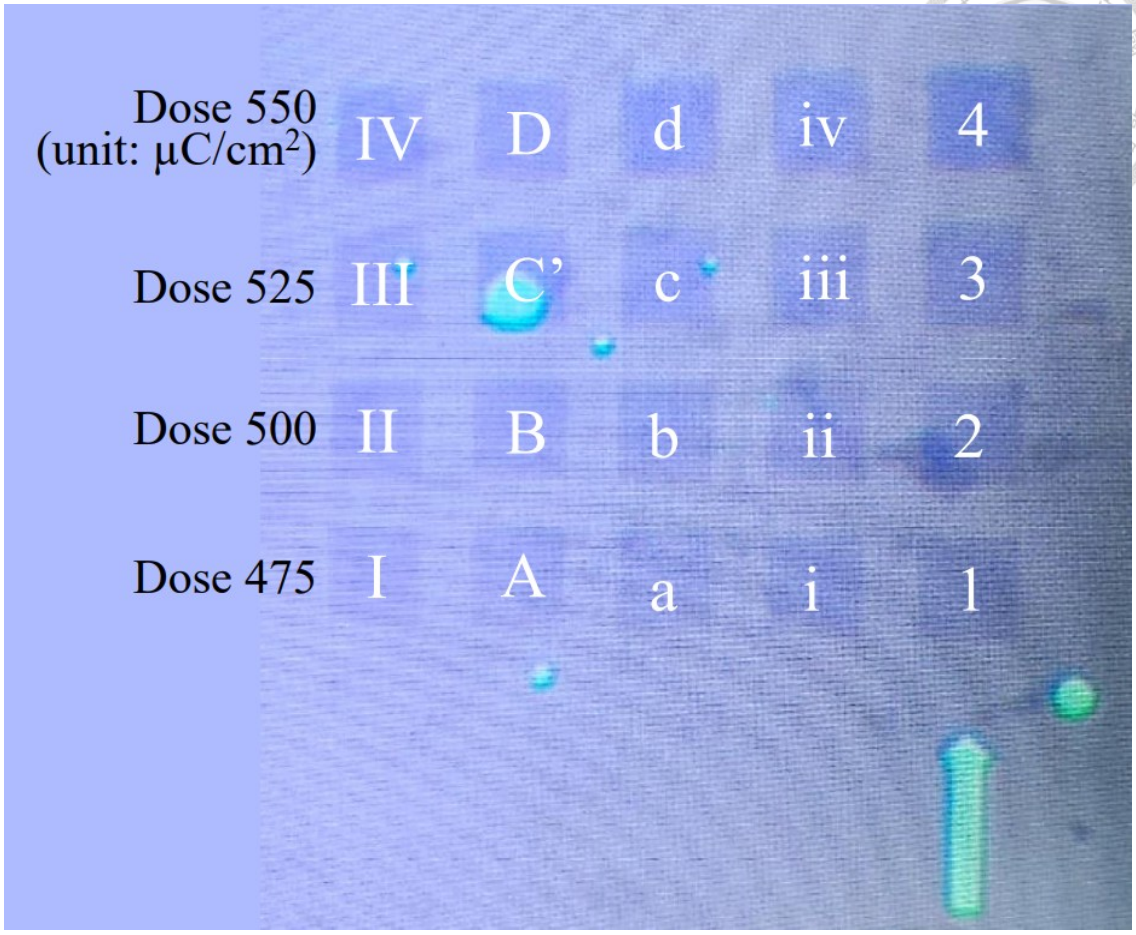

Figure 5.1: Sample arrays with different dose times are labeled according to their column numbers. Arrays 1, i, a, A, I used EBL dose 475 μC/cm^2 for patterning. Arrays 2, ii, b, B, II are patterned by dose 500 μC/cm^2. Arrays 3, iii, c, C', III are patterned by dose 525 μC/cm^2. Arrays 4, iv, d, D, and IV are patterned by dose 550 μC/cm^2. With larger doses, pattern shapes will be enlarged.

doi:10.6342/NTU202501130

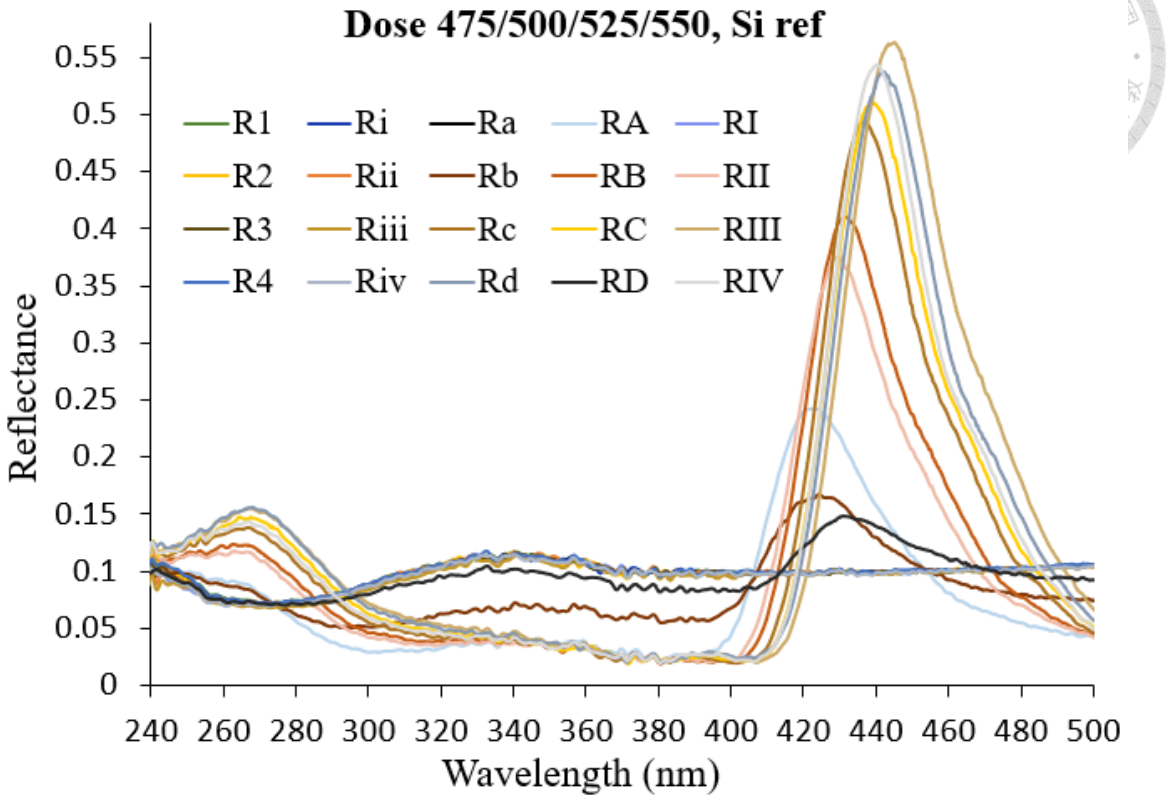

Figure 5.2: Spectra of shuffled nanodisk arrays measured with silicon (Si) mirror as reference background. The reference spectrum is a bulk single crystalline silicon wafer. Integration time is set as 1200 ms in the measurement. Representation of "Ri" means the reflectance from the Array i and so do other arrays. From the spectra, we see two peaks, one lies in the DUV region near 270 nm, and the other lies in the visible region near 450 nm. Therefore, from the optical microscopy, patterns look purple. There are 20 measured spectra with four different doses. R1, Ri, Ra, RA, RI are of dose 475 $\mu C/cm^2$. R2, Rii, Rb, RB, RII are of dose 500 $\mu C/cm^2$. R3, Riii, Rc, RC, RIII are of dose 525 $\mu C/cm^2$. R4, Riv, Rd, RD, and RIV are of dose 550 $\mu C/cm^2$.

doi:10.6342/NTU202501130

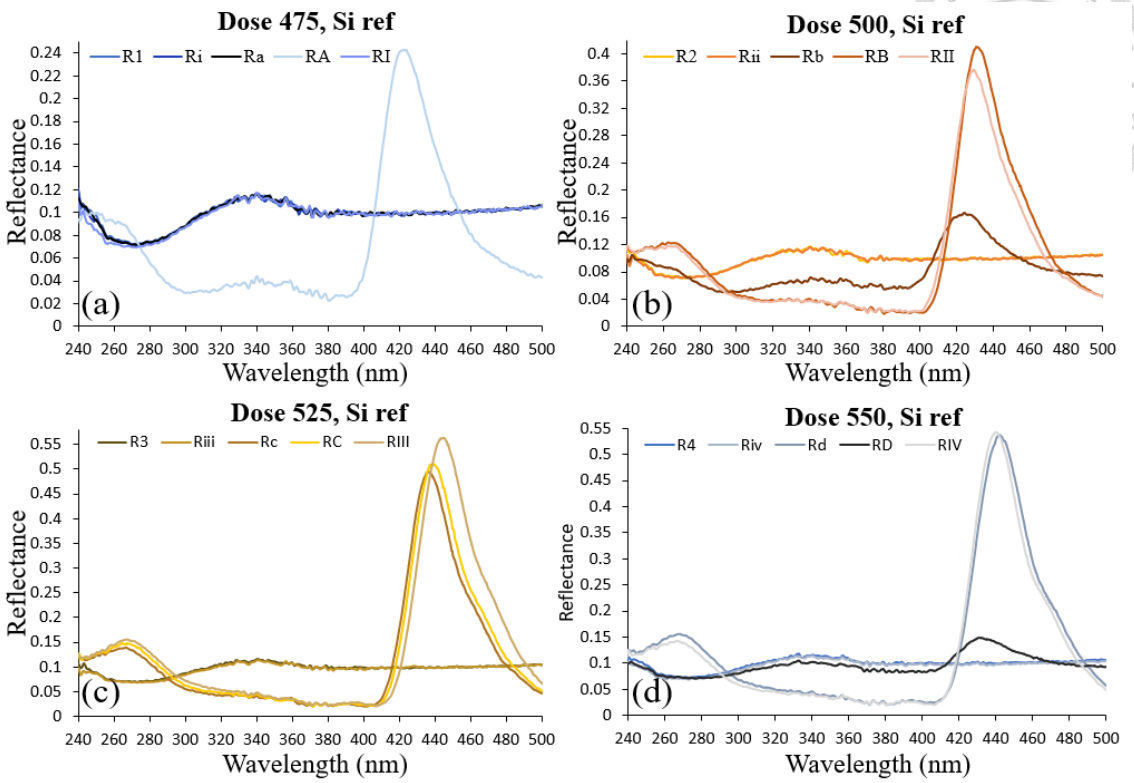

Figure 5.3: Separated spectra with different doses with Si mirror. There are five spectra of each dose. For dose 475 μC/cm^2, a peak is shown near 340 nm in four spectra. RA shows two peaks, one lying at 340 nm and the other lying at 430 nm. For a dose of 500 μC/cm^2, resonance peaks are distributed at 270 nm, 340 nm, and 430 nm. For dose 525 μC/cm^2, peaks of R3, RC, and Riii lie at 270 nm and 440 nm, and they are quite consistent with the simulation results. For dose 550 μC/cm^2, peaks of Riv and RIV lie at 270 nm and 445 nm, which are also consistent with the simulation results. Overall, the spectra of dose 525 seem to be the best fit with the simulation result.

doi:10.6342/NTU202501130

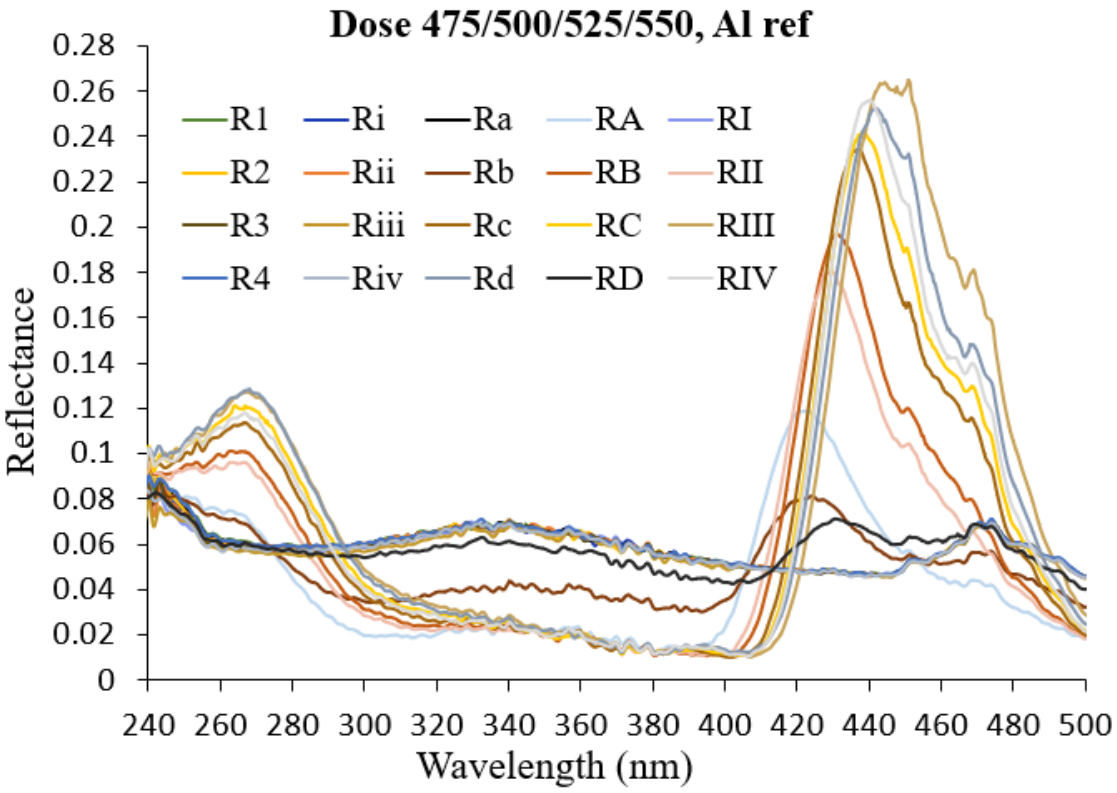

Figure 5.4: Spectra of shuffled nanodisk arrays measured with an aluminum (Al) mirror. The reference spectrum is a bulk single-crystalline silicon wafer. Integration time is set as 1200 ms in the measurement. Representation of "Ri" means the reflectance from the Array i, and so do other arrays. From the spectra, we see two peaks, one lying in the DUV region near 270 nm, and the other lying in the visible region near 450 nm. Therefore, from the optical microscopy, patterns look purple. There are 20 measured spectra with four different doses. R1, Ri, Ra, RA, RI are of dose 475 μC/cm^2. R2, Rii, Rb, RB, RII are of dose 500 μC/cm^2. R3, Riii, Rc, RC, RIII are of dose 525 μC/cm^2. R4, Riv, Rd, RD, and RIV are of dose 550 μC/cm^2.

doi:10.6342/NTU202501130

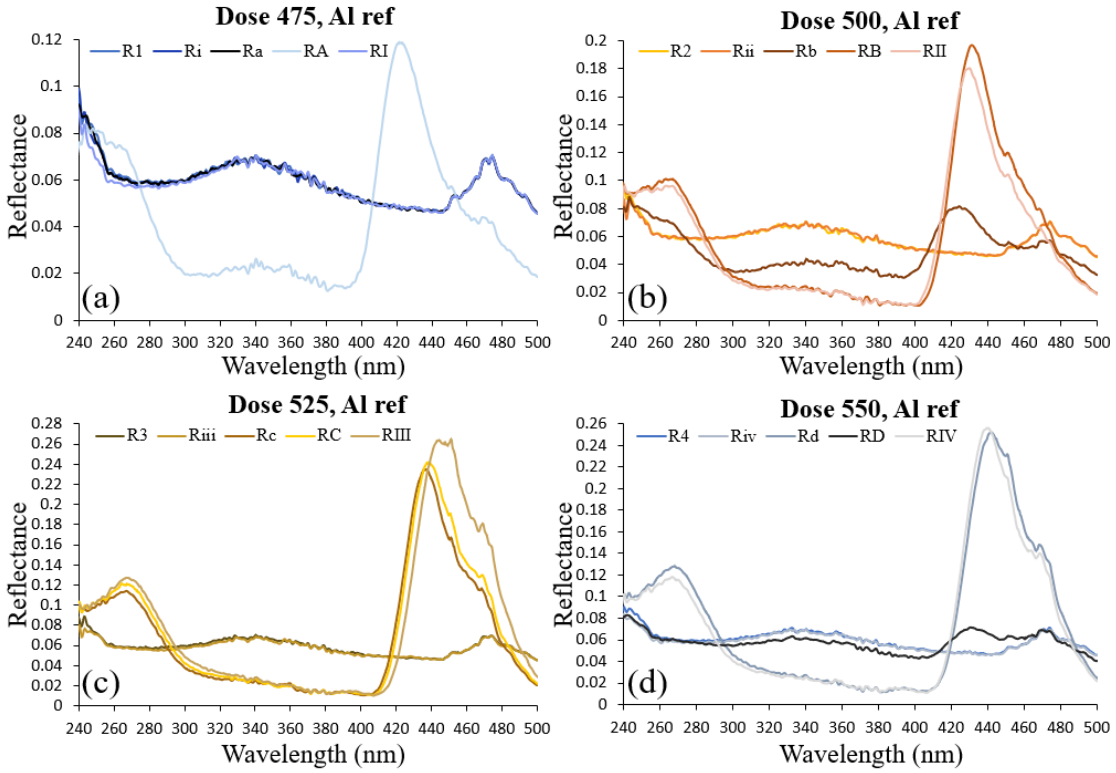

Figure 5.5: Separated spectra with different doses with Al mirror. There are five spectra of a single dose. For dose 475 μC/cm^2, a broadened peak is shown near 340 nm in four spectra. RA shows two peaks, one lies on 340 nm, and the other lies on 430 nm. For dose 500 μC/cm^2, resonance peaks are distributed at 270 nm, 340 nm, and 430 nm. For dose 525 μC/cm^2, peaks of R3, RC, and Riii lie at 270 nm and 440 nm, which are quite consistent with the simulation results. For dose 550 μC/cm^2, peaks of Riv and RIV lie at 270 nm and 445 nm, which are consistent with the simulation results. Compared to spectra measured with Si mirror, spectra with Al mirror are more fluctuating. It might come from a stronger reflection from Al than the Si mirror.

In sum, the above-mentioned spectra show resonance peaks on Array A, b, B, II, c, C', III, IV, and d. Spectrum measurement is performed before May 2024. After May,

doi:10.6342/NTU202501130

the system was slightly adjusted to perform experiments faster.

Since the setup was slightly modified, I remeasured the spectrum of the same sample using a 2 μm pinhole in diameter. It turned out that R4 (from Array 4) showed a clear resonance peak at 270 nm. Array 4 is used to measure the repeatability of nonlinear scattering in Section 5.2.

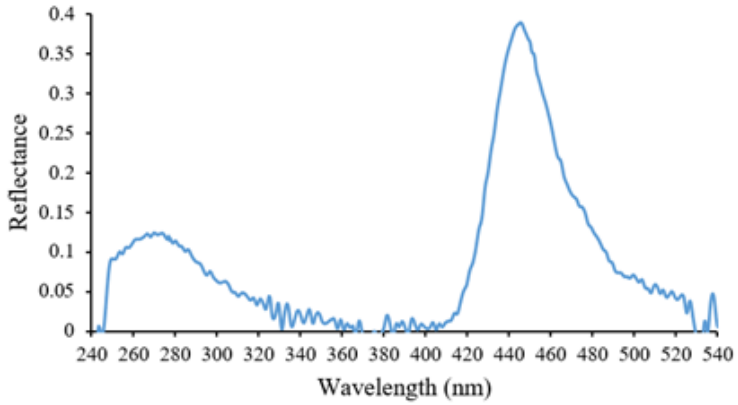

Figure 5.6: The Spectrum of Array 4 shows a resonance peak at 270 nm. Array 4 shall be a good candidate for measuring nonlinearity.

5.2 Photothermal nonlinearity experimental measurement

Figure 5.7 shows the preliminary results of the nonlinear scattering of shuffled silicon nanodisk arrays measured in April. There is no shutter for adjusting exposure times, so the reversibility needs to be checked to avoid damaging the sample. The signal captured is the transmission signal of the shuffled array (equivalent to the forward scattering of a single nanodisk). The y-axis is the voltage measured by the photodetector. The x-axis is

doi:10.6342/NTU202501130

the excitation intensity of measuring a laser light spot of a diameter of 25 μm. The power meter for measuring the laser excitation power is placed behind the OBJ1 in accordance with Figure 3.17. We observed the nonlinear scattering shown on the sample arrays corresponding to the spectra showing resonance peaks in Figure 5.3 and Figure 5.5.

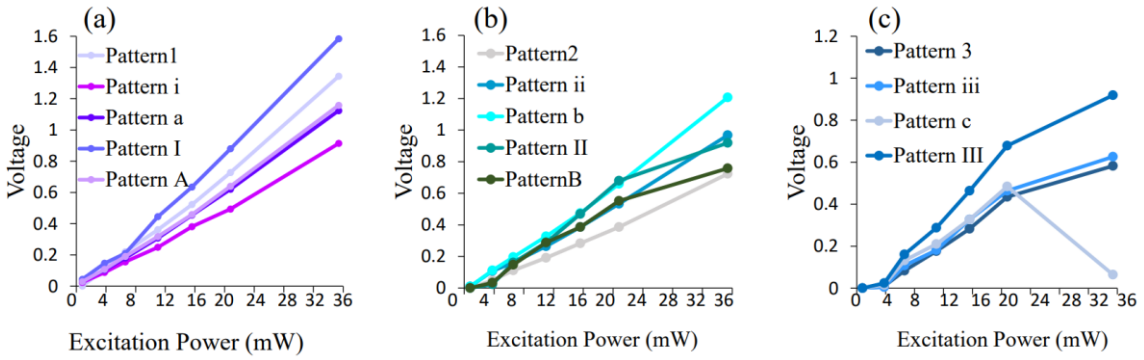

Figure 5.7: Preliminary results of photothermal nonlinearity of shuffled silicon arrays. (a) Patterns 1, i, a, I, A, with EBL dose 475 μC/cm^2, under observation, showed linear scattering. (b) Patterns 2, ii, b, with dose 500 μC/cm^2, showed linear scattering, and patterns II and B showed nonlinear scattering, which accorded with patterns showing resonance peaks in DUV. (c) Patterns 3, iii, c, III with dose 525 μC/cm^2, showed nonlinear scattering. Pattern c showing much obvious nonlinearity is possibly due to the remaining Cr mask. Arrays 4, iv, d, IV, D are not observed in Figure 5.6. modified system for observing Array 4 is discussed below.

We modified the system with an optical chopper to control the exposure time with 600 Hz for measuring reversibility of Array 4 with the light path shown in Figure 3.17. Several sets of data are demonstrated for Array 4, including the transmission signal of silicon arrays, quartz and air signal for normalization. The transmission signal of the

doi:10.6342/NTU202501130

background quartz means that the incident light passes through quartz substrate and reaches the photodetector. That of silicon array means that light passing through silicon arrays, reaching quartz substrate and being collected by the photodetector. Subtracting two signals derives the transmission signal of silicon nanodisks. Raw data in Figure 5.8 to Figure 5.11 are demonstrated below for clarity. Experiments were performed with a laser spot size of the diameter of 25 μm.

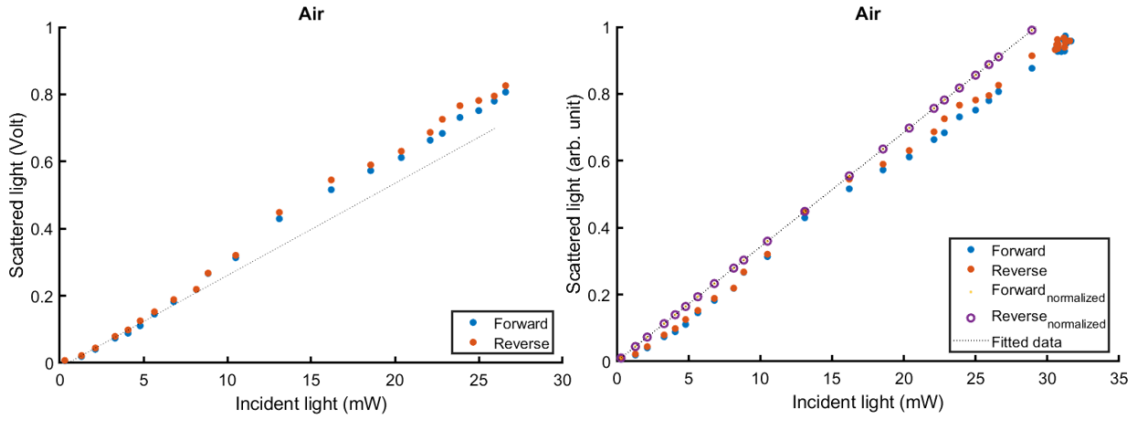

Figure 5.8: Transmission signal of air (left) and its normalization signal (right). Air signal should not show nonlinearity, so we normalize the air signal to linearity. Blue dots represent a signal with increasing incident light power. Orange dots represent a reverse measurement with decreasing laser light power. Yellow spots and purple spots represent the normalized data of forward and reverse data, respectively.

doi:10.6342/NTU202501130

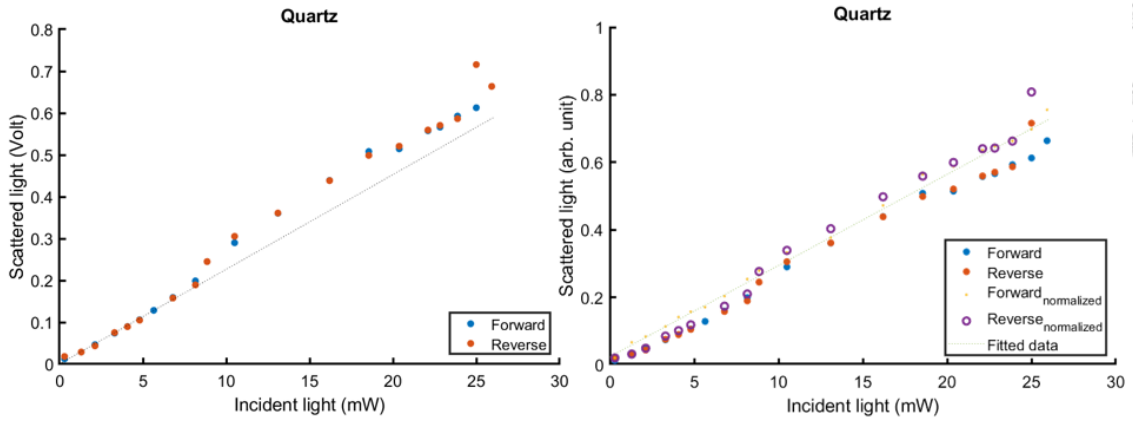

Figure 5.9: Reversibility and repeatability of photothermal nonlinearity of the transmitted signal of the quartz substrate. Light passing through the quartz substrate and being collected by the photodetector. The left is the experimental raw data and the right is the fitted data. Increasing signal in a forward direction overlaps well with the reverse direction with decreasing light intensity. Fitted signal of quartz demonstrates a linear tendency then nonlinearity. However, quartz shall not show nonlinearity. It indicates a system instability after the incident light of 9 mW with a spot size of 25 μm.

A good reversibility of the normalized quartz signal is demonstrated in the right figure below the incident power of 9 mW. The left figure demonstrated in Figure 5.9 shows experimental raw data and the right figure is the normalized signal. We further normalized the silicon signal based on the normalization factor derived from the air. The following four figures demonstrated in Figure 5.10 are transmitted signals of silicon nanodisks on quartz, two left figures are experimental raw data of light passing through Array 4 and quartz. The two right figures are the normalized silicon data. Overall, forward

doi:10.6342/NTU202501130

and reverse data overlap well. It showed a good reversibility in experiments below 9 mW with laser light spot in diameter of 25 μm.

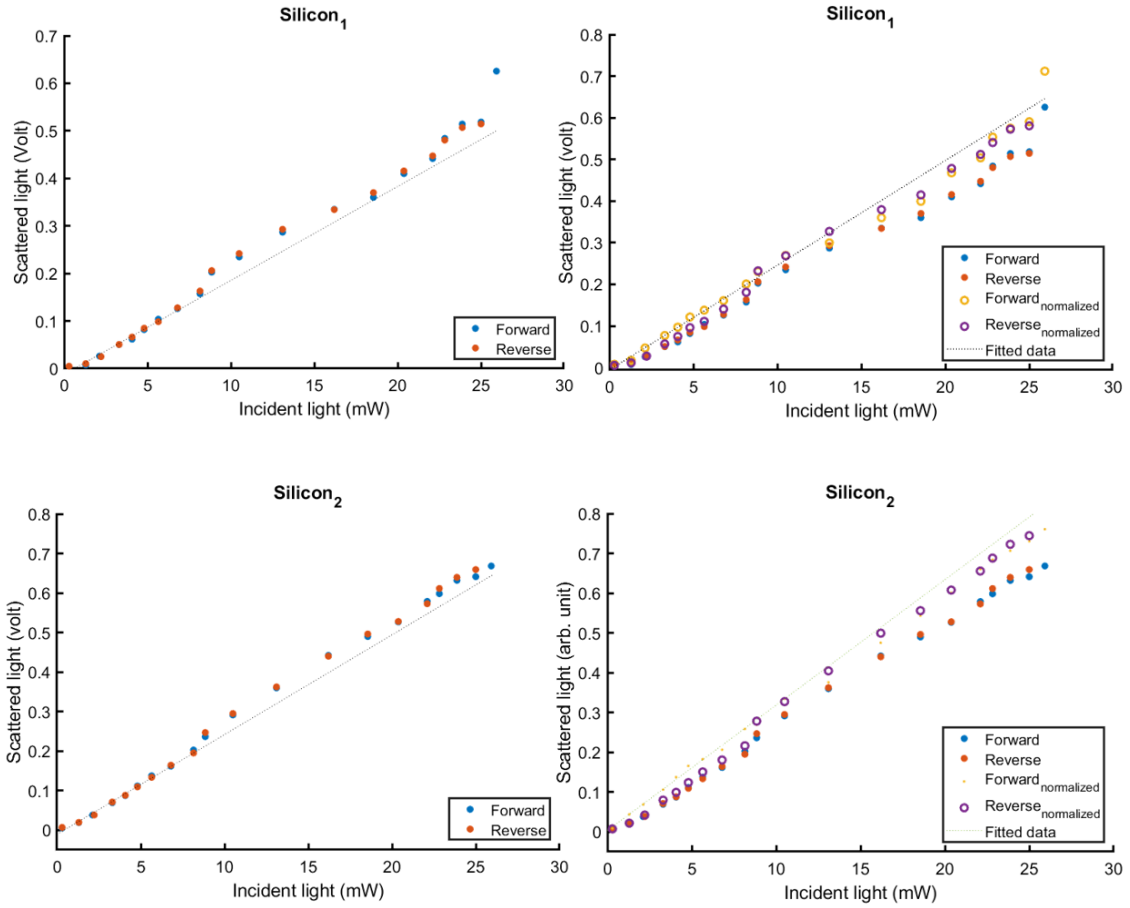

Figure 5.10: Reversibility and repeatability of silicon's nonlinearity: Light passes through silicon nanodisks and the quartz substrate, collected by a photodetector. The left figures are the experimental raw data. The dashed line is a linear fitting of the former several data points; the right figures demonstrate normalized data in yellow with the forward direction, in purple with the reverse direction. Two sets of experimental data were performed sequentially on the same day in the order of $Silicon_1$ and then $Silicon_2$. $Silicon_1$ measurement deviates from linearity starting from 13.1 mW. $Silicon_2$ measurement deviates from linearity starting from 16.2 mW. Overall speaking, linearity shows a good reversibility, and a larger incident power

doi:10.6342/NTU202501130

leads to a deviation from linearity. Furthermore, we tried to shrink the spot size to 2~5 μm by enhancing the laser incident power.

With a smaller incident light spot demonstrated in Figure 5.11, linearity lasts to 8.15 mW with a smaller spot size.

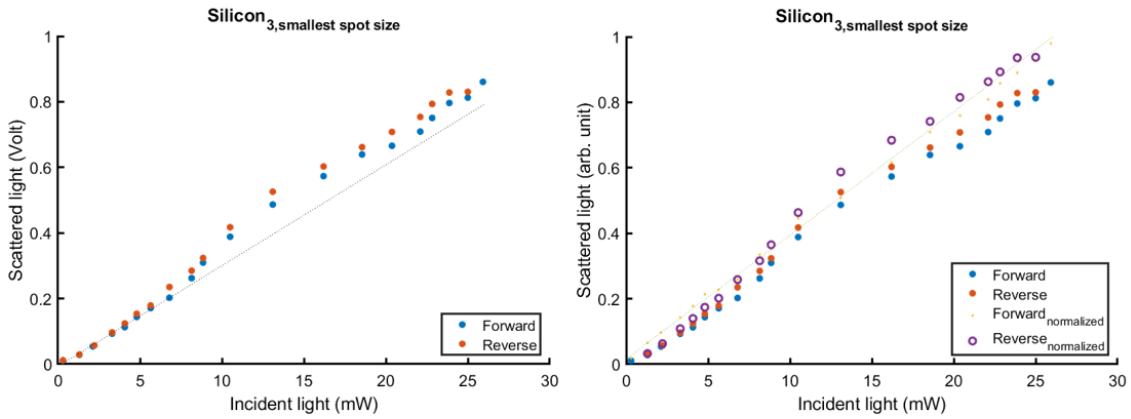

Figure 5.11: Reversible measurement of silicon signal with a spot size of 2~5 μm. This signal is deemed as the intensity of the incident light.

To sum up, the experimental system with a photodetector contributes to a linear tendency below 13.1 mW, 16.2 mW with a spot size of 25 μm, and 8.15 mW with a spot size of 2~5 μm. However, experiments are already modified to be able to demonstrate reversibility with linearity, proving an optimized system stability. Hopefully, we can distinguish nonlinear tendency with a photodetector of higher sensitivity, such as an avalanche photodetector that can extract signal down to nano-watt.

doi:10.6342/NTU202501130

Chapter 6. Conclusion and future work

6.1 Conclusion

We numerically studied polaritonic resonance-induced photo-thermal-optical nonlinearity, a single crystalline silicon nanodisk lying on a quartz substrate combining FDTD and FEM methods. The photothermal nonlinearity was demonstrated for the first time numerically, based on silicon polaritonic resonance down to a wavelength of 266 nm. We optimized the radius of a single silicon nanodisk with the particle swarm optimization (PSO) method. We further simulate the photothermal nonlinear scattering of a single silicon nanodisk of radius 35 nm and demonstrate the resolution enhancement based on the dSAX method to obtain a 1.38 times smaller PSF to achieve the spatial resolution enhancement in simulation. To further improve the simulation accuracy, we note that the real part of n used in the simulation is 16.5%–22.5% lower than the experimentally measured value. According to eq. 2.4.1, a decrease in n leads to a lower modulation depth of 4.28%, which is 2.21% less than the simulation result. This reduced modulation depth suggests that, for a nanodisk structure, the actual outcome may be even less favorable than predicted.

In the simulation demonstrated in Figure 4.5, the refractive index used is the blue fitted line shown in Figure 6.1. Comparing the experimental data in Figure 4.5 to the

doi:10.6342/NTU202501130

temperature-dependent refractive index reported in Ref. [67] reveals a good agreement. Even though the refractive index measured in Ref. [7] covers a broader temperature range up to 700 K, the limited data reported in Ref [67] show that temperatures ranging from 300 K to 500 K exhibit a 16.5%–22.5% lower difference in *n*. On the other hand, *k* differs from 0.98% to 1.05% with a larger slope from 300K to 400K and 450K to 500K.

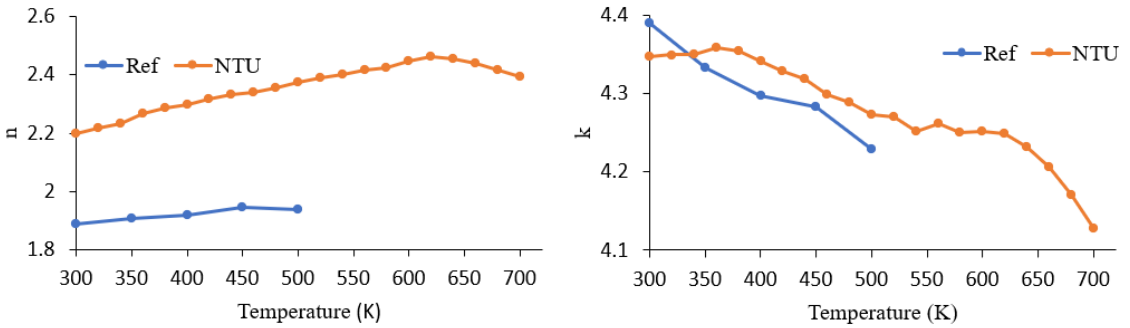

Figure 6.1: Comparing the experimentally measured *n* and *k* at 266 nm based on the experimental data from the referenced paper published in [67] with the theoretical analysis.

Experimentally, we fabricated shuffled silicon nanodisk arrays for observing nonlinear scattering. Due to the background noise level, a linear trend with fluctuations was observed. However, it is promising to complete the experiment in the near future with an avalanche photodetector and the construction of a stage scan for silicon nonlinearity with high stability and sensitivity.

6.2 Future work

We would like to further optimize the polariton resonance-induced photo-thermo-optical nonlinearity using different shapes or materials for an even larger modulation depth. In

doi:10.6342/NTU202501130

addition, a promising application is SAX super-resolution optical microscopy operating in the deep ultraviolet region, with metasurfaces that allow for function switching at different temperatures, serving as an all-optical switch or for bio-sensing research.

doi:10.6342/NTU202501130

Reference

1. Ma, Z. & Seiler, D. G. *Metrology and Diagnostic Techniques for Nanoelectronics*. (CRC Press, 2017).

2. Erni, R., Rossell, M. D., Kisielowski, C. & Dahmen, U. Atomic-resolution imaging with a sub-50-pm electron probe. *Phys. Rev. Lett.* **102,** 096101 (2009).

3. Custance, O., Perez, R. & Morita, S. Atomic force microscopy as a tool for atom manipulation. *Nat Nanotechnol*. **4**, 803–810 (2009).

4. Brodusch, N., Demers, H. & Gauvin, R. *Field Emission Scanning Electron Microscopy: New Perspectives for Materials Characterization.* (Springer, 2017).

5. Nguyen, D. T. et al. Super-resolution fluorescence imaging for semiconductor nanoscale metrology and inspection. *Nano Lett.* **22**, 10080–10087 (2022).

6. Luo, H. et al. Self-sensing scanning superlens for three-dimensional noninvasive visible-light nanoscale imaging on complex surfaces. *Nano Lett.* **23**, 4311–4317 (2023).

7. Duh, Y.-S. et al. Giant photothermal nonlinearity in a single silicon nanostructure. *Nat. Commun*. **11**, 4101 (2020).

8. Daunois, A. & Aspnes, D. E. Electroreflectance and ellipsometry of silicon from 3 to 6 eV. *Phys. Rev. B*, **18**, 1824-1839 (1978).

9. Zheng, G., Horstmeyer, R. & Yang, C. Wide-field, high-resolution Fourier

doi:10.6342/NTU202501130

ptychographic microscopy. *Nature Photon* **7**, 739–745 (2013).

10. Mayerich, D. & Sun, R. Superresolution image processing. In *Microscope Image Processing* (Academic Press, 2023).

11. Yu, B. et al. FinFET scaling to 10 nm gate length. In *Digest of Technical Papers. International Electron Devices Meeting* (IEEE, 2003).

12. Jagtap, S. M. & Gond, V. J. Study the performance parameters of novel scale FINFET device in nm region. In *2017 International Conference on Electronics, Communication and Aerospace Technology (ICECA)* (IEEE, 2017).

13. Beyond the diffraction limit [Editorial] *Nat. Photonics* **3**, 361 (2009).

14. Vicidomini, G., Bianchini, P. & Diaspro, A. STED super-resolved microscopy. *Nat. Methods* **15**, 173–182 (2018).

15. Rust, M. J., Bates, M. & Zhuang, X. Sub-diffraction-limit imaging by stochastic optical reconstruction microscopy (STORM). *Nat. Methods* **3**, 793–795 (2006).

16. Shroff, H., White, H. & Betzig, E. Photoactivated localization microscopy (PALM) of adhesion complexes. *Curr. Protoc. Cell Biol.* **58**, Ch. 4.21.1-4.21.28 (2013).

17. Fujita, K., Kobayashi, M., Kawano, S., Yamanaka, M. & Kawata, S. High-resolution confocal microscopy by saturated excitation of fluorescence. *Phys. Rev. Lett.* **99**, 238105 (2007).

18. Ravikumar, V. K. et al. Super-resolution laser probing of integrated circuits using

doi:10.6342/NTU202501130

algorithmic methods. *Nat. Commun.* **13,** 5155 (2022).

19. Chu, S.-W. et al. Measurement of a saturated emission of optical radiation from gold nanoparticles: application to an ultrahigh resolution microscope. *Phys. Rev. Lett.* **112**, 017402 (2014).

20. Tang, Y.-L. et al. Mie-enhanced photothermal/thermo-optical nonlinearity and applications on all-optical switch and super-resolution imaging. *Opt. Mater. Express* **11**, 3608–3626 (2021).

21. Nishida, K., Deka, G., Smith, N. I., Chu, S.-W. & Fujita, K. Nonlinear scattering of near-infrared light for imaging plasmonic nanoparticles in deep tissue. *ACS Photonics* **7**, 2139–2146 (2020).

22. Tsoulos, T. V. & Tagliabue, G. Self-induced thermo-optical effects in silicon and germanium dielectric nanoresonators. *Nanophotonics* **9**, 3849–3861 (2020).

23. Tonkaev, P. & Kivshar, Y. High-Q Dielectric Mie-Resonant Nanostructures (Brief Review). *JETP Letters* **112**, 615–622 (2020).

24. Dong, Z. et al. Ultraviolet Interband Plasmonics with Si Nanostructures. *Nano Lett*. **19**, 8040–8048 (2019).

25. Philipp, H. R. & Ehrenreich, H. Optical Properties of Semiconductors. *Phys. Rev.* **129**, 1550 (1963).

26. Lee, B.-R. et al. Deep-UV silicon polaritonic metasurfaces for enhancing

doi:10.6342/NTU202501130

biomolecule autofluorescence and two-dimensional material double-resonance Raman scattering. *Adv. Funct. Mater.* **35**, 2402439 (2025).

27. Young, A. T. Rayleigh scattering. *Appl. Opt.* **20**, 533–535 (1981).

28. Nawa, Y. *et al.* Saturated excitation microscopy using differential excitation for efficient detection of nonlinear fluorescence signals. *APL Photonics* **3**, 080805 (2018).

29. Yamanaka, M. *et al.* Saturated excitation of fluorescent proteins for subdiffraction-limited imaging of living cells in three dimensions. *Interface focus* **3**, 20130007 (2013).

30. Sivan, Y. & Chu, S.-W. Nonlinear plasmonics at high temperatures. *Nanophotonics,* **6**, 317–328 (2017).

31. Nagasaki, Y. Structural color generation with silicon-based Mie resonators. *PhD thesis*, Osaka Univ. (2022).

32. Hergert, W. & Wriedt, T. *The Mie Theory: Basics and Applications*. (Springer, 2012).

33. Grandy, W. T. *Scattering of Waves from Large Spheres.* (Cambridge Univ. Press, 2000).

34. Burlak, G. N. *The Classical and Quantum Dynamics of the Multispherical Nanostructures*. (Nova Science Publishers, 2004).

35. Davis, E. J. & Schweiger, G. *The Airborne Microparticle.* (Springer, 2002).

36. Kerker, M. *The Scattering of Light and Other Electromagnetic Radiation*. (Elsevier, 2016).

doi:10.6342/NTU202501130

37. Maier, S. A. *Plasmonics: Fundamentals and Applications*. (Springer, 2007).

38. Bohren, C. F. & Huffman, D. R. *Absorption and Scattering of Light by Small Particles*. (Wiley, 1998).

39. Mayer, K. M. & Hafner, J. H. Localized surface plasmon resonance sensors. *Chem. Rev.* **111**, 3828–3857 (2011).

40. Kittel, C. *Introduction to Solid State Physics*. (Wiley, 1956).

41. Low, T. et al. Polaritons in layered two-dimensional materials. *Nat. Mater.* **16**, 182–194 (2017).

42. Jackson, J. D. *Classical Electrodynamics.* (Wiley, 1999).

43. Giannini, V., Zhang, Y., Forcales, M. & Gómez Rivas, J. Long-range surface polaritons in ultra-thin films of silicon. *Opt. Express.* **16**, 19674–19685 (2008).

44. Yang, F., Sambles, J. R. & Bradberry, G. W. Long-range coupled surface exciton polaritons. *Phys. Rev. Lett.* **64**, 559–562 (1990).

45. Toudert, J. & Serna, R. Interband transitions in semi-metals, semiconductors, and topological insulators: a new driving force for plasmonics and nanophotonics. *Opt. Mater. Express* **7**, 2299-2325 (2017).

46. Hu, C. *Modern Semiconductor Devices for Integrated Circuits*. (Prentice Hall, 2010).

47. Lagois, J. & Fischer, B. Introduction to surface exciton polaritons. *Festkörperprobleme* **18**, 197–216 (1978).

48. Amans, D. et al. Ellipsometric study of silicon nanocrystal optical constants. *J. Appl. Phys*. **93**, 4173–4179 (2003).

doi:10.6342/NTU202501130

49. Zallen, R. & Paul, W. Effect of pressure on interband reflectivity spectra of germanium and related semiconductors. *Phys. Rev.* **155**, 703–711 (1967).

50. Cardona, M., Shaklee, K. L. & Pollak, F. H. Electroreflectance at a Semiconductor-Electrolyte Interface. *Phys. Rev.* **154**, 696 (1967).

51. Oane, M., Mahmood, M. A. & Popescu, A. C. A state-of-the-art review on integral transform technique in laser–material interaction: Fourier and non-Fourier heat equations. *Materials* **14**, 3906 (2021).

52. Liu, Y. & Zhang, X. Metamaterials: a new frontier of science and technology. *Chem. Soc. Rev.* **40**, 2494–2507 (2011).

53. Jaysaval, P., Shantsev, D. & de la Kethulle de Ryhove, S. Fast multimodel finite-difference controlled-source electromagnetic simulations based on a Schur complement approach. *Geophysics* **79**, E315–E327 (2014).

54. Archambeault, B., Brench, C. & Ramahi, O. M. The finite-difference time-domain method. *In EMI/EMC Computational Modeling Handbook 35–70* (Springer, 2001).

55. Taflove, A., Oskooi, A. & Johnson, S. G. *Advances in FDTD Computational Electrodynamics: Photonics and Nanotechnology*. (Artech House, 2013).

56. Cheng, H.-Y. *et al.* Large optical modulation of dielectric Huygens' metasurface absorber. *Adv. Opt. Mater.* **11**, 2300102 (2023).

57. Marini, F. & Walczak, B. Particle swarm optimization (PSO). A tutorial.

doi:10.6342/NTU202501130

Chemometrics Intell. Lab. Syst. **149**, 153–165 (2015).

58. Website. Yong, R [最佳化演算法]粒子群演算法 Particle swarm optimization (PSO) (2021).

59. Website. https://machinelearningmastery.com/a-gentle-introduction-to-particle-swarm-optimization/

60. Website. https://optics.ansys.com/hc/en-us/articles/360034922953-Optimization-utility.

61. Website. https://optics.ansys.com/hc/en-us/articles/360034382934-Tips-and-best-practices-when-using-the-FDTD-TFSF-source.

62. Nagasaki, Y., Suzuki, M. & Takahara, J. All-dielectric dual-color pixel with subwavelength resolution. *Nano Lett.* **17**, 7500–7506 (2017).

63. Tseng, M. L. et al. Vacuum ultraviolet nonlinear metalens. *Sci. Adv.* **8**, eabn5644 (2022).

64. van de Groep, J. & Polman, A. Designing dielectric resonators on substrates: combining magnetic and electric resonances. *Opt. Express* **21**, 26285–26302 (2013).

65. Lautenschlager, P., Garriga, M., Vina, L. & Cardona, M. Temperature dependence of the dielectric function and interband critical points in silicon. *Phys. Rev. B* **36**, 4821-4830 (1987).

66. Tang, Y.-L. *et al.* Multipole engineering by displacement resonance: a new degree of

doi:10.6342/NTU202501130

freedom of Mie resonance. *Nat. Commun.* **14**, 7213 (2023).

67. Franta, D., Franta, P., Vohánka, J., Čermák, M. & Ohlídal, I. Determination of thicknesses and temperatures of crystalline silicon wafers from optical measurements in the far infrared region. *J. Appl. Phys*. **123**, 185707 (2018).

68. Wu, H.-Y. *et al.* Ultrasmall all-optical plasmonic switch and its application to superresolution imaging. *Sci. Rep.* **6**, srep24293 (2016).

69. de Jong, S. XWS 30 - Broadband plasma light source. https://www.isteq.nl/xws-30.php.

70. Off-Axis Parabolic Mirrors, UV-Enhanced Aluminum Coating. https://www.thorlabs.com/newgrouppage9.cfm?objectgroup_id=7002.

71. Burlak, G. N. *The Classical and Quantum Dynamics of the Multispherical Nanostructures*. (Imperial College Press, 2004).

doi:10.6342/NTU202501130